Synthesis and Characterization of ZeoliteX supported MnO_2/Cu_2O composite for degradation of methylene blue from aqueous solution

Eset Negash Kebebew

A thesis Submitted to the Department of Materials Science and Engineering,
School of Mechanical, Chemical and Materials Engineering
Presented in Partial Fulfillment of the Requirement for the Degree of Master's in Materials Science and Engineering
Office of Graduate Studies
Adama Science and Technology University

June, 2023Gc
Adama, Ethiopia

Synthesis and Characterization of ZeoliteX supported MnO_2/Cu_2O composite for degradation of methylene blue from aqueous solution

Eset Negash Kebebew

Main Advisor: Gebissa Bekele (Ph.D.)

Co advisor: Osman Ahmed zelekew (Asso. Prof.)

A Thesis Submitted to the Department of Materials Science and Engineering, School of Mechanical, Chemical, and Materials Engineering

Presented in Partial Fulfillment of the Requirement for the Degree of Master's in Materials Science and Engineering

Office of Graduate Studies

Adama Science and Technology University

July 2023

Adama, Ethiopia

Declaration

I hereby declare that this Master's Thesis entitled “Synthesis and Characterization of ZeoliteX supported MnO_2/Cu_2O composite for degradation of methylene blue from aqueous solution” is my work and it has not been submitted for the award of any academic degree, diploma, or certificate in any other university. All sources of materials that are used for this thesis have been duly acknowledged through citation.

_____	_____	_____
Name of student	Signature	Date

Recommendation

I/We, the advisors of this thesis, hereby certify that I have closely advised/supervised the student while developing this proposal and read the draft thesis entitled “Synthesis and Characterization of ZeoliteX supported MnO_2/Cu_2O composite for degradation of methylene blue from aqueous solution” prepared under my guidance by Eset Negash. Therefore, I/we recommend the submission of the revised version of the thesis to the department following the applicable procedures.

_____	_____	_____
Major Advisor	Signature	Date
_____	_____	_____
Co Advisor	Signature	Date

Approval

I/we, the advisors of the thesis entitled “Synthesis and Characterization of ZeoliteX supported MnO_2/Cu_2O composite for degradation of methylene blue from aqueous solution” and developed by Eset Negash hereby certify that the recommendation and suggestions made by the board of examiners are appropriately incorporated into the final version of the thesis.

_____	_____	_____
Major Advisor	Signature	Date

_____	_____	_____
Co-Advisor	Signature	Date

Approval of Board of Reviewers

We, the undersigned, members of the Board of Examiners of the thesis by Eset Negash have read and evaluated the thesis entitled “Synthesis and Characterization of ZeoliteX supported MnO_2/Cu_2O composite for degradation of methylene blue from aqueous solution” and examined the candidate during the open defense. This is, therefore, to certify that the thesis is accepted for partial fulfillment of the requirement of the degree of Master of Science in material science and Engineering.

Chairperson	Signature	Date
Internal Examiner	Signature	Date
External Examiner	Signature	Date

Finally, approval and acceptance of the thesis/dissertation proposal are contingent upon the submission of its final copy to the Office of Postgraduate Studies (OPGS) through the Department Graduate Council (DGC) and School Graduate Committee (SGC).

Department Head	Signature	Date
School Dean	Signature	Date
Office of Postgraduate Studies, Dean	Signature	Date

ACKNOWLEDGMENTS

First of all, I praise the Lord God Almighty for providing me with the power and grace to carry out this work. Foremost, I would like to express my deep and sincere gratitude to my research advisor, Dr. Gebissa Bekele for his encouragement, and timely and constructive insightful comments which have been very helpful in improving and guiding the thesis process. I would like to express my gratitude to my co-adviser Dr. Osman Ahmed for his valuable advice and insightful comments. I would like to thank all staff of material science and engineering and also the technical staff, specially Mr. Demeke Tesfaye and Mr. Henok Mekonen for their support. I would also thank the ASTU Department of Chemical Engineering Staff and office workers, for their technical and moral support. I am grateful to Adama Science and Technology University, specially to the School of Mechanical, Chemical, and Material Science and Engineering, for their precious support. I am extremely grateful to my parents for their love, prayers, caring, and all the sacrifices in educating and preparing me for my future. Last but not least, I would like to thank my classmates, relatives, and friends who in one way or another shared their support.

TABLE OF CONTENTS

LIST OF FIGURES

LIST OF TABLES

ACRONYMS

AOP	Advanced Oxidation Processes
AA	Ascorbic acid
BET	Brunauer-Emmett-Teller
Cu_2O	Copper di Oxide
CB	Conduction Band
DRS	Differential Reflectance Spectroscopy
DTA	Differential Thermo gravimetric Analysis
EIS	Electrochemical Impedance Spectroscopy
FT-IR	Fourier transforms infrared spectroscopy
MB	Methylene blue
MC	MnO_2 with Cu_2O heterojunction
MK	Metakaolin
MnO_2	Manganese di Oxide
NaOH	Sodium Hydroxide
NP	Nanoparticle
PDE	Percent Degradation Efficiency
PL	Photoluminescence-Spectroscopy
SC	Semiconductor
SEM	Scanning Electron Microscopy
TGA	Thermo Gravimetric Analysis
UV–Vis	Ultraviolet-visible spectroscopy
VB	Valence Band
XRD	X-Ray Diffraction
Zeolite X	Faujsite zeolite (low silica-to-alumina ratio)
ZMC	ZeoliteX supported MnO_2 with Cu_2O heterojunction
V_{FB}	Flat band potential

E_g	Bandgap
e^-	electron
h^+	hole
H_2O_2	Hydrogen Peroxide
$\cdot OH$	Hydroxyl Radicals
$\cdot O^{-2}$	Oxygen Radical

ABSTRACT

Water pollution is a result of the massive amounts of waste products, like organic dyes, that have been released into the environment as a result of global industrial expansion. An appealing method for eliminating organic dye pollutants from wastewater is to use semiconductors as a photocatalyst. MnO_2 has shown potential uses in the photocatalytic field in recent years. However, its performance is constrained due to its high agglomeration, limited stability and high photo-induced electron-hole pair recombination rate. In this thesis, MnO_2 coupled with Cu_2O by varying their concentration whereas MnO_2 takes 10%, 30%, 50%, 70%, and 90% ratio of the composite and labeled as 1MC, 3MC, 5MC, 7MC, and 9MC respectively which are intended to reduce the recombination rate. To characterize the as-prepared samples different techniques such as XRD, SEM, FTIR, Uv/Vis-DRS, BET, TGA, PL, and EIS were used. The photocatalytic activities of MnO_2, Cu_2O, ZeoliteX, ZM, MC,1-ZMC, 2-ZMC, 3-ZMC, 4-ZMC, and 5-ZMC catalysts were tested towards the degradation of Methylene Blue (MB), and 49%, 52%, 54%, 61%, 74.7%, 87%, 91%, 99.01%, 97%, and 89.1% were degraded respectively in 80 min reaction time using 0.4g/L amount of catalyst within neutral pH (pH7) at room temperature. Also, the ternary composite without any light was checked and degraded 75% of MB dye. Among the catalysts, 3-ZMC had the highest performance which could be due to the synergetic effect of heterojunction (MC) and the support with sufficient amount of ZeoliteX that results in low recombination, lower electron transfer resistance, low agglomeration, and high surface area. The stability experiment revealed that 3-ZMC demonstrates a relatively good photocatalytic activity after 4 recycles. Therefore, ZeoliteX-supported MnO_2/Cu_2O is a promising catalyst for the degradation of MB under visible light.

Keywords: ZeoliteX, heterojunction, synergetic effect, Methylene Blue

CHAPTER ONE

1. Introduction

1.1 Background of the study

Pure water is the most important thing for life since it is the fundamental component for circulating all the necessary nutrients in the body of humans as well as other living things (Cech, 2018). Thus, keeping the health of the water is the same as increasing the life span of living things (Nathanson & Ambulkar, 2018). Even if industrialization, agriculture, and geological changes have improved the quality of life, they are contributing to water, soil, and air pollution since they release a variety of pollutants, including organic dyes, heavy metals, iron, nitrate, arsenic, fluoride, and halide (Nathanson & Ambulkar, 2018). Organic dyes are colorants that are used in fabric, paper, plastic, medicine, and other objects (Gürses et al., 2016). About 15% of the total world dye production is wasted and released into water or soil. This dye have a significant impact on the health of aquatic ecosystems and the organisms that live in them (Natarajan, Bajaj, & Tayade, 2018). So discharge of dyes must be properly and economically regulated in order to keep health of living things (Fu, Cheng, & Lu, 2015; Jackson et al., 2001; Nathanson & Ambulkar, 2018; Quiton, Lu, & Huang, 2021).

The most common methods to treat wastewater are chemical precipitation (Shim et al., 2014), ion exchange (Mohammadi, Moheb, Sadrzadeh, & Razmi, 2005), chemical coagulation (Ashraf et al., 2021), flocculation (Zambrano, Cobeña, Ponce, Cedeño, & Briones, 2021), bioremediation (Mingshan et al., 2021), adsorption (Yagub et al., 2014) and advanced oxidation (Q. Li et al., 2018). Among those methods, advanced oxidation processes (AOPs), is a relatively promising method to degrade organic dye to a harmless substance, additionally, the low-cost and energy method called photocatalysis technology is a promising method to remove dyes (Al-Khalid & El-Naas, 2012; Q. Li et al., 2018).

Photocatalysis is a method that uses light to exit electrons from the valence band to the conduction band, and then the chemical reaction by electrons and holes with oxygen and water respectively resulted in the formation of reactive radicals that degrade the organic dyes (Q. Wang & Yang, 2016).

The metal oxide is one of the most effective materials for photocatalytic activity due to its favorable electronic structure, capacity for light absorption, and capacity for charge transport (Danish et al., 2021). TiO_2 (Cavalcante et al., 2016), ZnO (Tian et al., 2012), NiO (Motahari, Mozdianfard, Soofivand, & Salavati-Niasari, 2014), Co_3O_4 (Warang, Patel, Fernandes, Bazzanella, & Miotello, 2013), Fe_2O_3 (Keerthana et al., 2021), WO_3 (Ismail, Faisal, & Al-Haddad, 2018), Cu_2O (Ajmal et al., 2016), MnO_2 (Alzahrani, Al-Thabaiti, Al-Arjan, Malik, & Khan, 2017), etc. are widely used for photocatalyst material.

Manganese dioxide (MnO_2) is one of the common and effective n-type metal oxide used for the degradation of organic pollutants since it is readily available, inexpensive, nontoxic, environmentally compatible, and have a narrow band gap that makes it able to absorb visible light solar spectrum (Kim, Lee, Chang, & Chang, 2013; R. Yang et al., 2021). However, the photocatalytic performance of MnO_2 is limited because of its high agglomeration and recombination rate (Jin, Wang, et al., 2020; Xue, Zhang, Shao, & Yang, 2020).

Building suitable heterogeneous photocatalytic systems is a promising solution for modifying and resolving the problems of single metal oxides like MnO_2 (B. Li et al., 2020). Among various ways of constructing heterojunction direct Z-scheme between the CBs and VBs of n and p-type semiconductors get more attention due to their ability for efficient charge separation and transfer mechanism that results in enhanced photocatalytic activity (Q. Zhang, Peng, Deng, Wang, & Chen, 2020).

Cu_2O is a p-type semiconductor that exhibits excellent visible light absorption and has a low band gap of up to 2.6 eV. Moreover, it is a low-cost, non-toxic, and abundant metal oxide (Y. Zhang, Deng, Zhang, Gao, & Xu, 2010). The conduction band edge (CB) of Cu_2O has been reported as comparatively more negative than MnO_2 (Aguirre, Zhou, Eugene, Guzman, & Grela, 2017). On the other side, MnO_2 has a more positive valance band edge (VB) than Cu_2O (M. Zhang et al., 2021). More importantly, MnO_2 and Cu_2O are n and p-type metal oxides respectively. So those characteristics make them to full fill basic requirements to form direct Z-scheme p-n hetero-junctions (T. Yu, Sun, Zhe, Wang, & Rao, 2017).

The other challenge of metal oxide MnO_2 or the heterojunction is the high agglomeration rate which affects the photocatalyst performance. This problem can be overcome by supporting MnO_2 or heterojunction nanoparticles on the surface of porous material without affecting their distinctive properties (De Gisi, Lofrano, Grassi, & Notarnicola, 2016).

Nowadays, ZeoliteX-supported photocatalytic degradation of dye is getting more attention due to the basic properties of ZeoliteX including thermal stability, high surface area, low Si/Al ratio, and abundant acid sites which makes it able as both adsorbing agent of dye and dispersing agent for photocatalyst (Han et al., 2010; Vickers, 2017). Thus, the combination of Zeolite with the metal oxides has synergic effects by using Zeolite to adsorb the dyes and the metal oxides degrade them (Awuchi, Hannington, Awuchi, Igwe, & Amagwula, 2020).

There are many reports on MnO_2-based composites with different metal oxide and porous support materials such as Fe_3O_4/MnO_2/ZIF-8 ternary composite (Xuelian Li, Raza, & Liu, 2021), Carbon Nanosheet/MnO_2/BiOCl (X. Hong, Li, Wang, Long, & Liang, 2022), Zeolite supported ZnO/Fe_2O_3/MnO_2 (Tedla, Díaz, Kebede, & Taddesse, 2015) and MnO_2 supported on bentonite clay (Nakhaei, Barzgari, Mohammadi, & Ghazizadeh, 2019).

Even though a lot of work and research done to enhance the photocatalytic activity of MnO_2 for the degradation of dye either by making heterojunction or by synergetic effect with support material, still it cannot meet an efficient and cost-effective way. Most commonly the catalyst synthesized have a low yield, use expensive raw material, high electron resistance, and costly or time taking approach taken that make it incapable to meet environmental and economic concern.

In this work, ZeoliteX-supported MnO_2/Cu_2O heterojunctions were synthesized by the wet impregnation method. The material results in a synergetic effect of photocatalytic activity from metal oxide heterojunction and adsorption from ZeoliteX support material which performs degradation of dye under visible light. Additionally, ZeoliteX is synthesized from easily accessible kaolin clay by a simple alkali fusion method. A variety of characterization methods were utilized to assess the synthesized samples and used for the degradation of MB. It is expected that the catalyst could have enhanced degradation performance since catalysts have a low recombination rate, low electron transfer resistance, good absorption of visible light, lower agglomeration, and high surface area.

1.2 Statement of the problem

Wastewater is a major environmental issue that affects communities all around the world (Muga & Mihelcic, 2008). Dyes are one of the water pollutants that, when discharged into bodies of water result in serious consequences for the environment and public health. Among different methods, Photocatalysis is a promising method to remove dyes that involve the use of light and metal oxide as a catalyst (Bora & Dutta, 2014).

Manganese dioxide (MnO_2) is an abundant, affordable, nontoxic, and environmentally compatible metal oxide with narrow band gap energy (1-2 eV) which makes it qualified as a potential photocatalyst (Kim et al., 2013). However, the applicability of MnO_2 semiconductor is still limited due to its fast recombination rate of photo-generated electron-hole pairs, low quantum efficiency, high agglomeration, and low stability (R. Yang et al., 2021; Q. Zhang et al., 2020). To improve the photocatalytic performance of MnO_2, several methods such as doping with metallic and non-metallic elements, coupling with other metals, and supporting on porous adsorbent have been used (Q. Zhang et al., 2020). However, MnO_2 nanoparticles' photocatalytic activities are not effective, and additional research is needed to address these issues. This work focuses on the synergetic effect of ZeoliteX-supported p-n heterojunction of MnO_2 with Cu_2O for photocatalytic activity. Among P-type metal oxide Cu_2O are comparatively accessible and in expensive that can be easily synthesized. Additionally, Cu_2O and MnO_2 make a good band alignment, which lowers the recombination rate and increase quantum efficiency (Aguirre et al., 2017; Y. Zhang et al., 2010). ZeoliteX with large surface area and lewis acid site is made from kaolin clay instead of expensive chemicals and a simple low-cost alkali fusion method is employed. Therefore, this work offers an inexpensive way of coupling and supporting an approach for enhancing MnO_2 performance toward commercial dye degradation.

1.3 Objectives

1.3.1 General objective

Synthesis and Characterization of ZeoliteX supported MnO_2/Cu_2O composite for degradation of methylene blue from aqueous solution.

1.3.1 Specific objectives

- ✓ Synthesizing MnO_2 and Cu_2O metal oxides
- ✓ Synthesizing ZeoliteX from locally available raw kaolin clay by alkali fusion method
- ✓ Examine the effect of Cu_2O on the recombination rate of MnO_2 by coupling MnO_2 with Cu_2O
- ✓ Investigating the effect of ZeoliteX support on agglomeration rate and photodegradation performance of MnO_2 with Cu_2O heterojunction
- ✓ Characterization of prepared material properties including crystallinity, morphology, functional group, surface area, band gap, and thermal analysis
- ✓ Analyze the photocatalytic activity of the synthesized catalyst under different effects on MB degradation

1.4 Scope of the study

This study focuses on the removal of methylene blue dye from an aqueous solution by using a ZeoliteX-supported MnO_2/Cu_2O composite. It started by synthesizing single MnO_2 and Cu_2O followed by making their heterojunction by varying their concentration to reduce recombination rate by the optimized ratio with a good performance on the degradation of MB. ZeoliteX prepared from kaolin clay helps to minimize the cost of precursors for mass production of zeolite and is environmentally friendly. Finally, the ternary composite is made by supporting the MnO_2/Cu_2O heterojunction on ZeoliteX which reduces the agglomeration rate of the metal oxides, increases the active site for adsorption of methylene blue, and enhances photocatalytic activity. Several methods, including XRD, TGA, Uv-Vis, FTIR, SEM, DRS, BET, PL, and EIS are used to characterize those samples.

Additionally, the catalyst's pH impact, catalytic dose, initial dye concentration, kinetics, and reusability are all examined. It further focuses on the application of the synergetic effect of ternary composite by adsorption and photodegradation of methylene blue dyes from aqueous solution.

1.5 Significance of the study

This study primarily benefits the textile, paper, cosmetic, and leather processing industries, since those industries are generating huge amounts of organic dyes. This thesis aims to reduce the environmental pollution of these dyes by designing a synergetic effect from the heterojunction of MnO_2 with Cu_2O photocatalyst and the support ZeoliteX that used for large scale to purify contaminated water since the material can be synthesized in mass production by cost-effective and easy method to perform.

CHAPTER TWO

2. Literature Review

2.1 Wastewater

Uncontaminated water is one of the most valuable resources since no life can survive for some days without water. Additionally, water is very important for various activities starting from home, agriculture, industry purpose, and so on due to this there is a motto, “Water is life” (Sturm, Goldstein, & Parr, 2017). However, urbanization, industrialization, and a lack of understanding among people regarding the necessity of water have resulted in the deterioration of the quality of water (Kemacheevakul & Chuangchote, 2020). Consequently, the wide spreads of diarrhea, cholera, dysentery, and hepatitis are regularly announced because contaminated water contains pathogens, organic and inorganic chemicals, which include heavy metals, dyes, volatile organic compounds (VOC), oil, plastics and pesticides (Hasan, Shahriar, & Jim, 2019; Shaker-Agjekandy & Habibi-Yangjeh, 2016).

About 15% of the total world dye production is wasted during the dyeing process and discharged in textile effluents, which cause non-aesthetic pollution, eutrophication, and disturbances in aquatic life (Dutta, Gupta, Srivastava, & Gupta, 2021). Dyes can be classified as anionic, cationic, and non-ionic dyes. Methylene Blue (MB) is a cationic dye most commonly used substance for dying (H. Yang et al., 2006). MB leads to diseases such as vomiting, shock, increase heart rate, cyanosis, jaundice, and tissue necrosis in humans (Lou, Yan, & Wang, 2019). Those coloring compounds and the effluent requires proper treatment before it is discharged into any water body to save lives and protect the environment (Diallo et al., 2018).

2.1.1 Methods of wastewater treatment

There are several techniques to eliminate or minimize the level of these pollutants from wastewater including chemical precipitation (Shim et al., 2014), ion exchange (Rahimi, Jafari, Abdolahnejad, Farrokhzadeh, & Ebrahimi, 2019), chemical coagulation (Ashraf et al., 2021), flocculation (Jabbar, Barzinjy, & Hamad, 2022), bioremediation (Mingshan et al., 2021), membrane filtration (Hube et al., 2020), adsorption (Mouni et al., 2018) and photocatalytic degradation (Q. Li et al., 2018). The limitation and advantages of those methods are listed in Table 1.

Table 1**:** Methods of wastewater treatment

Type of method	**Material used**	**Advantage**	**Limitation**	**Reference**
Biological	Microorganisms	It is easy and profitable	Necessary to create an optimally favorable environment for maintenance of the microorganisms Inefficient on non-degradable compound	(Machinen i, 2019)
Chemical precipitation	Organic and inorganic chemicals	Require simple equipment Economically beneficial and effective Quite effective at removing metals	Chemical consumption is inefficient at low concentrations Issues with high sludge production, and disposal	(Wang et al., 2015)

Ion exchange	Porous solid with exchanged ions	Technologically simple Interesting and efficient technology	Economic constraints Performance sensitive to pH of the effluent Not effective for certain pollutants	(Rahimi et al., 2019)
Coagulation/ Flocculation	Inorganic and organic coagulant	Procedural simplicity Commercially available compounds come in a wide variety	Includes the addition of non-recyclable substances Increasing the production of sludge	(The et al., 2016)
Membrane filtration	Semipermeable barrier	Minimal space is needed. It is straightforward, quick, and effective	Excessively costly for Investment High operating and maintenance costs	(Hube et al., 2020)
Adsorption	Porous solid material with a large surface area	More applicable on large scale Regard to technology due to low-cost Numerous commercial goods are available.	The active site easily gets inefficient due to saturation Further treatment of adsorbed sludge	(De Gisi et al., 2016)
Advanced oxidation processes	Metal oxide	Little to no chemical consumption No sludge production	On a laboratory scale High-pressure and energy-demanding circumstances	(Deng & Zhao, 2015)

The wastewater properties will determine the procedure that will be employed (Crini & Lichtfouse, 2019). Recently, to treat wastewater containing dye residues, advanced oxidation processes (AOPs) have been viewed as a promising alternative (Foroutan, Peighambardoust, Boffito, & Ramavandi, 2022). In the case of methylene blue, it can be degraded by reactive species that formed by photocatalysts. During the treatment processes, it is important to monitor and compare color, pH, suspended solids, and temperature before discharging the corresponding effluent to the receiving water body (Yaseen & Scholz, 2019).

2.1.1.1 Advanced Oxidation Processes

Advanced oxidation processes (AOPs) are a set of chemical treatment methods that are designed to remove pollutants through a series of oxidation reactions (Atalay & Ersöz, 2015). AOP involves two stages of the reaction, the first to generate a strong oxidant (hydroxyl radical) and followed by the reaction of those strong oxidants with contaminants in water (Atalay & Ersöz, 2021). The high oxidation potential of hydroxyl radicals (2.80 eV), which gives them a wide range of offensive properties, is responsible for AOPs' adaptability (J. Wang & Wang, 2020). These potent free radicals can convert organic pollutants into CO_2, H_2O, or particular inorganic ions without producing any byproducts that would prevent the destruction of the target pollutants (Milenković et al., 2020). Because of its short lifespan and lack of toxicity, OH won't erode equipment parts, making it infrastructure-friendly so it can suit the various need of wastewater treatment (H. Liu, Wang, & Wang, 2020).

AOPs are typically divided into two categories: photochemical processes refer to a reaction initiated by the absorption of light and non-photochemical processes where the reaction occurs in the absence of light (Atalay & Ersöz, 2021). The most prevalent AOPs are wet air oxidation, ozonation, photocatalytic degradation, Fenton's reagent (H_2O_2/Fe^{2+}), and photo-Fenton due to their quick reaction times, potent oxidation abilities, and lower cost photocatalytic advanced oxidation processes have attracted increasing attention (H. Liu et al., 2020).

2.2 Photocatalysis

The term "Photocatalyst" combines the words "photo" which refers to a photon and "catalyst," which refers to a substance that alters the rate of a process or reaction (Pera-Titus, García-Molina, Baños, Giménez, & Esplugas, 2004).

As a result, photocatalysts are compounds that absorb light and act as catalysts for chemical reactions by changing the rate when exposed to light. In other words, it is chemical reactions that make use of light and a semiconductor to enhance the degradation of organic dyes from wastewater (Ameta & Ameta, 2018). Semiconductor nanoparticles (NPs) are energized by various types of wavelengths including ultraviolet, visible, and near-infrared light depending on their band gap energy (Hariganesh, Vadivel, Maruthamani, & Rangabhashiyam, 2020).

The incident light should have higher energy than the metal oxide band gap so the light absorbed by the photocatalyst generates electron and hole pair which involve several redox reactions that lead to the formation of reactive species for the degradation of dye (Tufail, Price, Mohseni, Pramanik, & Hai, 2021). There are two types of photocatalytic reactions which are homogeneous and heterogeneous photocatalysis based on the state of the semiconductor and reactants. Homogeneous refers to when the semiconductor and reactant are both in the same phase (Khor, Khan, Khan, Khan, & Harunsani, 2022). Compared to the homogenous, the heterogeneous photocatalytic method is mostly used to degrade organic pollutants from wastewater because of its capacity to destroy organic pollutants (Salari, 2019).

2.2.1 Working Principle of Photocatalysis for water purification

The working mechanism of the photocatalyst is shown in Fig.1. When a photocatalyst is exposed to the light of the desired wavelength (sufficient energy), the energy of photons is absorbed by an electron (e−) of the valence band and it is excited to conduction band whereas a hole (h+) created in the valence band. This process leads to the formation of the photo-excitation state, and an e− and h+ pair is generated (Hariganesh et al., 2020).

The photo-generated electrons reduce oxygen (O_2) to superoxide radicals and photo-generated holes, in turn, react with water to form hydroxyl radicals. Following the generation of hydroxyl radicals, the pollutants are oxidized, mineralized, and completely degrade then reduced to smaller molecules like CO_2, H_2O, and mineral acids which are not toxic (Antonopoulou, Kosma, Albanis, & Konstantinou, 2021). The appropriate band gap, proper shape, large surface area, stability, and reusability are the key characteristics of the photocatalytic system (Ikram et al., 2021).

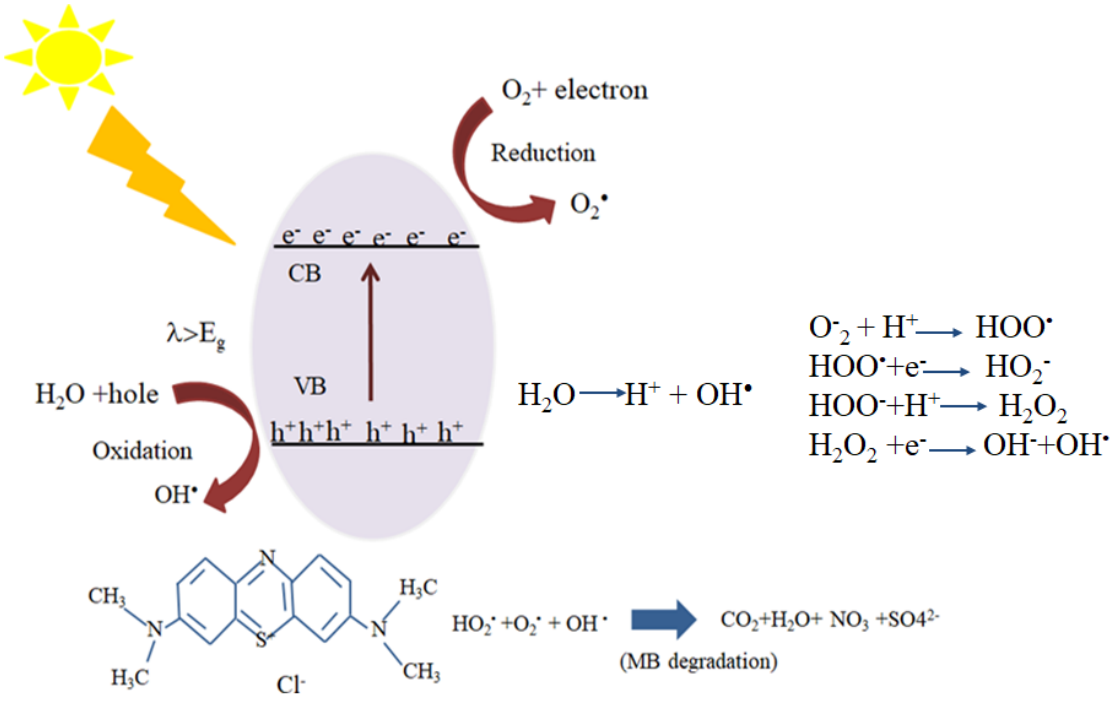

Figure 1: Working mechanism of photocatalyst

2.2.2 Photocatalytic semiconductors

Photocatalytic degradation of dyes has primarily been carried out using a variety of metal oxides such as zinc oxide(ZnO) (Xiaoqing Chen, Wu, Liu, & Gao, 2017), Titanium dioxide (TiO_2) (Lee & Park, 2013), Iron trioxide (Fe_3O_4) (Wu, Jiang, & Roy, 2015), Cadmium sulphide(CdS) (Hullavarad, Hullavarad, & Karulkar, 2008), Tin Oxide (SnO_2) (Prakash, Senthil Kumar, Pandiaraj, Saravanakumar, & Karuthapandian, 2016), Cobalt tetraoxide (Co_3O_4) (X. Hu et al., 2018), Copper dioxide (Cu_2O) (Y. Zhang et al., 2010), Nickel oxide(NiO) (Motahari et al., 2014) and Manganese dioxide (MnO_2) (Xia, Zhu, Cheng, Yu, & Xu, 2018). TiO_2 and ZnO are widely used and applicable metal oxides due to their special qualities like chemical stability, photocatalytic properties, durability, and high redox potential. However, they have wide bandgap energy leading to the absorption of light in the UV region (S. H. S. Chan, Yeong Wu, Juan, & Teh, 2011). Yet, the Uv light spectrum accounts for only 5% whereas the visible light spectrum accounts for around 45% of total solar energy (X. Chen et al., 2019).

So compared to the wide band-gap SC photocatalysts, small band-gap SCs have exhibited highly improved light harvesting ability in the visible range of the solar spectrum, leading to an enhancement in the photocatalytic efficiency (Iyengar, Das, & Balasubramaniam, 2017).

Physicochemical characteristics can be used to categorize different types of metal oxides. Their stability is one of these qualities. Pt, Pd, Ru, Au, and Ag are examples of metals having unstable high oxidation state oxides, which don't truly perform stable solid oxides at normal temperatures. The most commonly used metal oxide catalysts (Ti, V, Cr, Mn, Zn, and Al) have stable oxides with high oxidation states (Ahuja, Ujjain, Kanojia, & Attri, 2021).

2.3 Manganese dioxide (MnO_2)

Manganese dioxide (MnO_2) has several crucial aspects in practical application due to its abundance, cost, nontoxicity, environmental compatibility, and environmental purification activity (R. Yang et al., 2021). These distinctive qualities make it a potential and preferred functional material for different applications (Kim et al., 2013).

The crystal structure, stability, adsorption, electrochemical, photoelectrochemical, optical, and electronic properties of MnO_2 play a major role in the efficiency of MnO_2 for various applications (M. M. Ali & Williams, 2023; Ghosh, 2020).

Due to its narrow band gap (1.3-2.1 eV), MnO_2 is used as a photodegradation catalyst in the visible range of light (Q. Li et al., 2018). But some limitations of MnO_2 which are easily aggregated (R. Yang et al., 2021), slow chemical kinetics (Chang et al., 2019), and high electrons-holes recombination rate (R. Yang et al., 2021) limit its potential applications.

2.3.1 Physical structures of manganese dioxide (MnO_2)

MnO_2 is considerably used for multiple applications over other manganese oxides due to its different polymorphic structures (Tang et al., 2018). Each polymorph has unique pores or tunnel structures that allow specific ions and electrons to enter and leave the polymorph in different ways (Birgisson, Saha, & Iversen, 2018).

While sharing the same fundamental structure as [MnO_6], MnO_2 can be differentiated by the links that are joined by angles or edges, leading to a variety of tunnel and layered structures (Najafpour & Allakhverdiev, 2012). Three categories, namely 1D tunnel structures, 2D layer structures, and 3D mesh structures, can be used to categorize the primary kinds of crystalline MnO_2 α(hollandite), β-(pyrolusite), γ-(nsutite), δ-(birnessite), and λ-(akhtenskite) (Y.-F. Li, Zhu, & Liu, 2016).

The most stable MnO_2 polymorph, the β-MnO_2 phase (1×1 tunnel, rutile structure), keeps its structure up to 500 °C until oxygen release causes phase change to Mn_2O_3. Despite having a huge unoccupied 2×2 tunnel, the α-MnO_2 phase (2×2 and 1×1 tunnel structure) has remarkable thermal stability equivalent to the β phase (Hatakeyama, Okamoto, & Ichitsubo, 2022). The γ-MnO_2 phase shows a stepwise transformation into β-MnO_2 from 400°C after structure relaxation. By removing interlayer K ions, the δ-MnO_2 phase (layered structure) is quickly destabilized, losing the interlayer periodicity below 200°C but each layer is preserved up to about 500°C (Song et al., 2019). The thermally unstable λ-MnO_2 phase (defect spinel structure) changes into β-MnO_2 at about 250°C and then disintegrates into Mn_2O_3 above that temperature (Birgisson et al., 2018).

Due to its distinct physical and chemical characteristics, α-MnO_2 is well known as a precursor material frequently employed in electrochemical sensors (Song et al., 2019), catalysts (Saputra et al., 2012), cathodes of lithium or Mg batteries (Dinh et al., 2020), and molecular sieves (L. Li, Nan, Lu, Peng, & Li, 2012).

α-MnO_2 belongs to the tetragonal crystal system, which is widely found in nature (R. Yang et al., 2021). It has (2 × 2) tunnels of large square vacancies, which can be partially occupied by K^+, Na^+, Ba^+, $Mg^{2+,}$ or Ca^{2+} ions and water molecules. This structure would increase the adsorption ability of α-MnO_2 (Hatakeyama et al., 2022). Each MnO_2 NPs crystal structure has distinct characteristics and a separate method of production. Depending on the needs and resources available, one might choose from a variety of options (Dawadi et al., 2020).

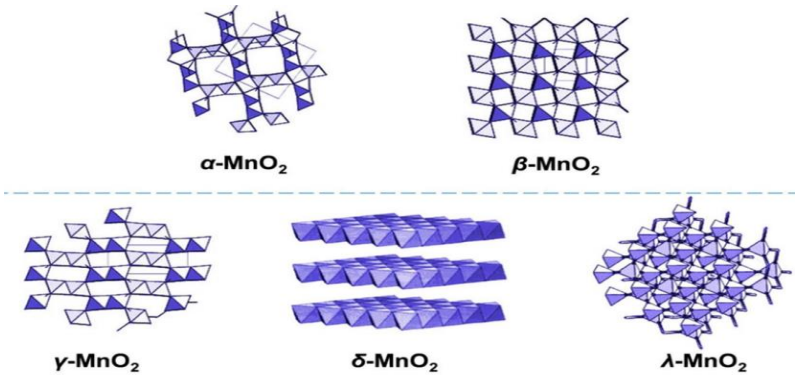

Figure 2:Crystal structures of α-, β-, γ-, δ-, λ-MnO_2 (Yunlong He, Kang, Li, Li, & Tian, 2023)

2.3.2 Synthesis methods of MnO_2 Nano particles

Several techniques have been reported for the control synthesis of nano MnO_2. The most frequently reported methods for the synthesis of MnO_2 nanostructures are solution-based ones, such as hydrothermal (Xiao, Sun, Zhou, Cai, & Hu, 2018), sol-gel (Y.-L. Chan, Pung, Sreekantan, & Yeoh, 2016), wet chemical (Xia et al., 2018), precipitation (J. Chen et al., 2018).

Due to their flexibility, controllability, and minimal energy consumption, solution-based approaches are preferred (Toupin, Brousse, & Bélanger, 2004).

The size and morphology of the desired MnO_2 nanostructures could be obtained by carefully controlling the experimental variables, such as the type of solvents, type of precursors, and reaction temperature (Chiam, Pung, & Yeoh, 2020).

The hydrothermal method is most frequently used to create MnO_2 due to its various advantages including the ease of use, generating homogeneous and controlled crystal development, and performing both synthesis and crystallization in a single step with high repeatability and reliability (Chiam et al., 2020). Yet, the hydrothermal process has drawbacks that include the need for waste liquor treatment, specialized equipment, organic solvents, and low yields so very difficult to produce industrial amounts (Z. Li et al., 2019).

Sol-gel is a straightforward method that can regulate chemical reactions, resulting in fine, extremely pure products with consistent crystal structure and shape (Franger, Bach, Farcy, Pereira-Ramos, & Baffier, 2002). For the manufacture of thickness-controlled multi-component oxide films, this method is quite helpful. However, the fundamental drawback of the sol-gel technique is the lengthy synthesis time and increased possibility of agglomeration (Baral, Satish, Zhang, Ju, & Ghosh, 2021).

Chemical co-precipitation is a straightforward technique for making nano material since it is simple to use, can be carried out at low temperatures with good yields, and is inexpensive. Nowadays, manganese salts with two distinct anions in equal concentration for instance, manganese(II) sulfate and manganese oxalate are used to accomplish the co-precipitation procedure (Chand, Joshi, Lal, & Singh, 2021).

The fabrication of MnO_2 nanostructures has also been documented using the mechanochemical dry route technique. It is a method of solvent-free synthesis that addresses chemical transformations brought on by mechanical energy (Achar, Bose, & Mal, 2017). This method can be accomplished without a surfactant and has benefits like fast preparative synthesis and simple control of particle size (S. Chen et al., 2009).

Through a redox reaction involving the oxidation of manganese (II) ions (Mn^{2+}) to manganese (IV) oxide (MnO_2) by an oxidizing agent such as hydrogen peroxide (H_2O_2) or potassium permanganate ($KMnO_4$), manganese dioxide (MnO_2) can be formed by a redox reaction. High yield with desired product and minimum formation of unwanted byproducts can be obtained by such a synthesis method (Toupin, Brousse, & Bélanger, 2002).

In addition, several advanced techniques such as green synthesis (Hoseinpour, Souri, & Ghaemi, 2018) and refluxing routes (Julien & Mauger, 2017) have undergone substantial development.

Although manganese dioxide NPs have been produced using a variety of techniques, getting the needed NPs remains difficult. Temperature and reaction time including aging must be taken into account when preparing since the particles' phase and morphology vary when the parameters are altered (Dawadi et al., 2020).

2.4 Surface Modification of MnO_2 Nanoparticle

The surface modification of NPs may enhance their physical, chemical, and other characteristics like activity and stability (Sun & Liu, 2008). The surface modification of NPs should be accomplished by doping either chemical or physical doping, junction with other semiconductors, and dispersion with in-support material (Toupin et al., 2004).

2.4.1 Doping

Doping refers to the deliberate introduction of impurities into pure semiconductors. It is generally known that doping with contaminants has a significant impact on fundamental physical characteristics (e.g., electrical, optical, and magnetic properties). Physical doping involves coating the dopant on the surface of the NPs, and the bond between them is weak, whereas chemical doping involves creating the NP on the surface of the dopant, and the bond is stronger (Erwin et al., 2005; C. Yu et al., 2012).

MnO_2's properties, such as its morphology, specific surface area, crystal structure, electronic structure, oxygen-manganese bond strength, surface species, etc., can also be enhanced by atom doping (R. Yang et al., 2021). As a result, several scientists have tried to dope MnO_2 with metal cations or nonmetals, respectively (McFarland & Metiu, 2013).

According to reports, the following elements have been added to MnO_2 to improve its performance in environmental applications: potassium (K), calcium (Ca), magnesium (Mg), iron (Fe), cobalt (Co), nickel (Ni), copper (Cu), zinc (Zn), aluminum (Al), titanium (Ti), vanadium (V), tungsten (W), molybdenum (Mo), zirconium (Zr), tin (Sn), lanthanum (Se) (R. Yang et al., 2021). According to several studies, the doping of alkali metal ions or alkaline earth metal ions has a significant impact on the shape, crystal structure, and catalytic and adsorption performances of materials based on MnO_2 (X. Hu et al., 2018; F. Liu, Xiao, Liu, Han, & Qin, 2020).

2.4.2 MnO_2-Based Composites

Even though MnO_2 has a good photocatalytic performance, the lower photoreduction ability due to the high conduction band potential and the high recombination efficiency of photogenerated carriers due to the small band gap limits the extensive usage of MnO_2 in the photocatalytic industry. Fortunately, the development of composite nanomaterials and the application of the junction catalysis idea have substantially improved this flaw (M. Zhang et al., 2021).

2.4.2.1 Homo junctions

Homo junctions are layers of junctions constructed from the same semiconductor components (Ma et al., 2016). It is well acknowledged that the creation of homo junctions can facilitate the improvement of the materials' photo-electrochemistry capabilities, as well as their capacity for adsorption and catalysis, due to the interface polarizations or preferred impedance matching characteristics (Su, Zhao, Fan, Li, & Zhang, 2019).

Hence, constructing a MnO_2/MnO_2 iso-type homo junction by joining different crystalline phases, crystal facets, or dimensions can offer a creative way to enhance adsorption and catalytic performances without the need for additional semiconductors. For environmental applications, a variety of MnO_2/MnO_2 iso-type homo junctions have been developed (Guo et al., 2019).

Despite considerable efforts, there are still significant shortcomings in the development of MnO_2-based homo junctions for environmental applications, hence there is still much potential for improvement by similar homo junctions composed of different crystal facets or dimensions, which is also helpful for enhancing catalyst performance (R. Yang et al., 2021). To date, only the core-shell structure between the two types of MnO_2 has been described, which restricts the further improvement of its specific surface area and interface active sites. Therefore, it is important to create more sophisticated structures, such as void-shell structures, ultrathin 2D/2D structures, etc (Su et al., 2019).

2.4.2.2 Heterojunction Semiconductor

Instead of being used in surface reactions to create the necessary reactive species, some of the photo-generated electrons mix back with the holes (Schneider et al., 2014). The absorbed energy is released as heat or light due to surface or bulk recombination, which lowers the photocatalytic efficiency. One of the greatest choices is connecting it with other semiconductors with compatible band structures to increase the separation efficiency of the electron-hole pairs and the durability of the produced reactive species (Su et al., 2019). When two different semiconducting materials are linked together, it creates a heterojunction whereas metal oxides with distinct band gaps and electrical configurations form band bending at the interface (Schneider et al., 2014). There are several different schemes for heterojunctions, depending on the alignment of the energy bands at the interface between the two semiconducting materials (Klein, 2012).

As shown in Figure 3(a) the band edges of semiconductor B with the lower band gap are encompassed within the VB and CB edges of semiconductor A with the bigger band gap in the type-I category, also known as straddling band alignment. Since both photo-generated charge carriers aggregate across the VB and CB of semiconductor B after light irradiation, the effective separation of charge carriers is not visible and the redox ability is significantly decreased in the case of the type-I heterojunction (Yuan, Yi, Tang, Liu, & Luo, 2020).

The type-II heterojunction (staggered type) is the most common type of charge transfer shown in Figure 3(b), the VB and CB of semiconductor A are situated above the corresponding energy levels of semiconductor B. Because of this, when a semiconductor is exposed to light, photo-generated electrons rush to the CB of semiconductor B while photo-generated holes migrate to the VB of semiconductor A, ensuring spatial electron and hole separation (Acharya, Nayak, Pattnaik, Acharya, & Parida, 2020).

The third kind, often referred to as the broken type or type-III, is made so that neither semiconductor's band gaps overlap, meaning that semiconductor B's VB and CB bands remain above those of semiconductor A's CB band (Figure 3(c)). The abovementioned band topology makes it unsuitable for charge separation since there is no charge carrier movement and hence no spatial separation (Yi et al., 2019).

The oxidation and reduction capabilities of the migrating holes and electrons decrease as they go to semiconductor B's CB, which has a lower reduction potential, and semiconductor A's VB, which has a lower oxidation potential. Building a unique photocatalytic system is essential to resolving the aforementioned problems (T. Yu et al., 2017). As shown in Figure 3(d), Z-scheme photocatalysts have recently grown in popularity because they not only stop the recombination of photo-generated electron-hole pairs but also maintain high redox activity (N. Yang et al., 2018; Zhou, Yu, & Jaroniec, 2014).

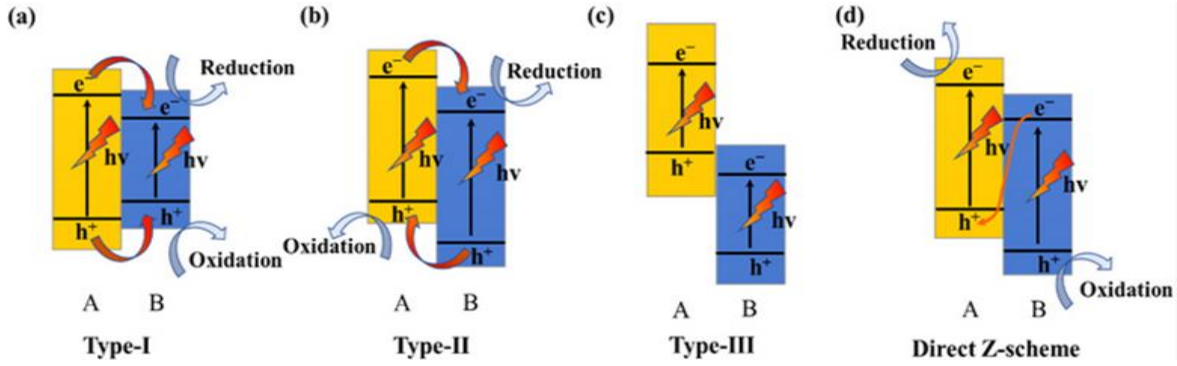

Figure 3 The charge-carrier separation mechanism on the type-I heterojunction (a), type-II heterojunction (b), type-III heterojunction (c), and the direct Z-scheme (d) (Xing Chen et al., 2022)

Numerous studies have shown that MnO_2 mixed with another semiconductor in one of the above-mentioned mechanisms can significantly increase their photocatalytic activity by enhancing their charge transfer property and reduced recombination rate when compared to pure nanostructures.

For instance, Zheng et al. (Zheng et al., 2016) obtained hybrid 3D Co_3O_4@MnO_2 heterostructures by a facile and highly efficient solution-based method on nickel foam, and the as-synthesized 3DCo_3O_4@MnO_2 heterostructures exhibited remarkable photocatalytic activity and recycling stability for the degradation of organic dyes. Liu, Suqin, et al. (S. Liu, Liu, Jin, & Yuan, 2015) synthesized a flower-like MnO_2/BiOI composite by a simple and cost-effective approach and demonstrated a photocatalytic degradation efficiency of 97.8% under visible light and 93.4% under simulated solar light irradiation for methyl orange (MO) within 40 min.

David, A. & Vidhi (A. David & Vedhi, 2022) prepared ternary composite Co_3O_4-MnO_2-ZnO NPs which exhibits the best performance (91.98%) for the degradation of MB in 90 min of irradiation time under sunlight. Recent studies on MnO_2-based heterojunction for the degradation of dye are summarized in Table 2.

Table 2**:** MnO_2-based heterojunction photocatalyst for degradation dye

No	**Material**	**Methodology**	**Targeted material**	**Efficiency**	**Degradation time**	**Reference**
1	α-MnO_2 - MoO_3	Ultrasonic	AB92	92%	50min	(Salari, 2020)
2	Co_3O_4 - MnO_2 - ZrO_2	Co-Precipitation	MB	68.24%	90min	(S. A. David & Vedhi, 2017)
3	3DCo_3O_4 - MnO_2	Wet impregnation	Eosin red, MB Congo red	68% 76.5% 95.7%	25 min	(Zheng et al., 2016)
4	MnO_2-BiOI	Wet impregnation	MO and RhB	97.8% 91.7%	40min	(S. Liu et al., 2015)
5	α -MnO_2 - AgBr	Wet impregnation	MB	96%	50min	(Salari & Hosseini, 2021)
6	CuO_x-MnO_2	Wet impregnation	MB	96%	140min	(T. Yu et al., 2017)
7	Fe_3O_4-α-MnO_2	coprecipitation	Crystalline violet	100%	70min	(Dubey, Challagulla, Wadhwa, & Kumar, 2021)
8	Mn_3O_4-MnO_2	Wet impregnation	MB	93.5%	1 min	(J. Zhao et al., 2017)
9	ZnO-MnO_2–Cu_2O	coprecipitation	RhB	98%	40min	(Hoseinpour & Ghaemi, 2018)
10	g-C_3N_4 / MnO_2 /GO	ultrasonic	Tetracycline hydrochloride	91.4%	60min	(Du et al., 2021)

11	3D Bi_2WO_6 /MnO_2	Hydrothermal	RhB and Acid Blue 92	100% and 87%	100min	(Salari & Yaghmaei, 2020)
12	TiO_2–MnO_2	Precipitation	Toluene	43%	60min	(Nevárez-Martínez et al., 2017)

On the other side due to their low band gap, low cost, abundance, and non-toxicity, copper-based materials are frequently used in the degradation of pollutants. Copper dioxide (Cu_2O) is one of the inexpensive p-type semiconductors that exhibits a low recombination rate and excellent visible light absorption (Y. Zhang et al., 2010). Their band structure (more negative conduction band edge and less positive valance band edge) than MnO_2 makes it suitable to form band alignment that enhances their performance. In addition, MnO_2 and Cu_2O are n and p-type semiconductors respectively so they make p-n heterojunction that would play the main role in enhancing charge transfer properties and catalytic performance of MnO_2 (D. Hong, Cao, Qu, Deng, & Tang, 2018).

The other limitation of MnO_2 is the high agglomeration rate and small active site. Also due to their small size the MnO_2 NPs might readily be washed away by running water so they could turn into secondary contaminants in the water system which require further treatments with more time and money, neither of which are economically viable (Z. Zhao, Liu, Cui, Feng, & Zhang, 2012). To address those shortcomings of MnO_2, supporting systems have been developed recently (R. Yang et al., 2021).

2.4.3 Synthesis of MnO_2 photocatalyst on supporting system

One strategy to disperse and improve the degradation performance of MnO_2 or MnO_2-based heterojunction is supporting porous adsorbent material which fulfills the basic criteria including non-toxicity, low cost, reproducibility, compatibility with the metal oxide to ensure good adhesion and stability (Upadhyay, Soin, & Roy, 2014).

Those support materials' adsorption abilities may attract organic pollutant molecules close to the catalytic surface, where hydroxyl and superoxide radicals are generated. Additionally, the dispersion effect of support not only inhibits aggregation but also makes it easier for the reclamation of photocatalysts from bulk media (G. Hu et al., 2021).

Inorganic support materials including activated carbon, zeolite, glass, and carbon nanotubes have been investigated to support MnO_2 to enhance photodegradation performance (Rao et al., 2020). Few studies have combined the aforementioned strategies to improve the photocatalytic properties of MnO_2 which are summarized in Table 3.

Zeolites one of the widely recognized promising candidates for hybrid adsorbents-photocatalyst applications due to their distinctive structural characteristics and chemical makeup, such as their high surface area, high adsorption, and condensation properties, an abundance of acid/base sites that can reduce the recombination of electron-hole pairs, adjustable surface property, nontoxicity, low cost, and hydrophilic quality (Shirzadi & Nezamzadeh-Ejhieh, 2016). Alumina silicate-type microporous materials made of tetrahedral SiO_4 and AlO_4 units make up conventional zeolite (Pang, Yu, Xu, Huo, & Chen, 2009).

From around 200 types of zeolite, faujasite is one of a naturally occurring mineral, and ZeoliteX and ZeoliteY are synthetic versions of it. In numerous industrial applications, including catalysis, adsorption, and separation procedures, zeolites X and Y are both extensively employed. Both have a low Si/Al ratio which implies more aluminum content that increases the probability of uncoordinated Aluminum. So, Lewis acid site form has strong interaction with electron-rich species that play a role in reducing the recombination rate of supported metal oxide or heterojunction (Day et al., 2021). Although these materials have similar structures, they vary in terms of composition, pore size distribution, and framework topology (Xu, Pang, Yu, Huo, & Chen, 2009).

ZeoliteX has a two-dimensional structure with small pore size and high surface charge density which provide an advantage for the selective and tighter adsorption of Methylene Blue (MB) molecules (Jamil, Ghafar, Ibrahim, & Abd El-Maksoud, 2011). This small pore size can provide a better confinement effect for the supported photocatalyst, which can enhance uniform distribution with stability and prevent it from diffusing out of the zeolite (Sethia, Somani, & Bajaj, 2015).

ZeoliteX can be manufactured from both natural and artificially found materials, however, from an economic standpoint, not all raw materials can be used to create zeolite. They should be affordable, easily accessible, low-cost to produce, selective, high-yield, and less abundant in foreign chemicals. Kaolin is one of the readily available raw materials that satisfy those requirement (Johnson & Arshad, 2014).

Table 3 MnO_2 supported on different metal oxides for degradation of dye

No	Material	Synthesize method	Targeted material	Efficiency (%)	Degradation time	Reference
1	MnO_2 /AC	wet chemical	MO	89	120min	(Pargoletti et al., 2019)
2	Fe_3O_4/MnO_2/ ZIF-8	Co-precipitation	Biphenyl A and TOC	100 and 80	15min and 9min	(Dong, Li, Chen, Chen, & Zhang, 2020)
3	MnO_2/BC	Co-precipitation	MB	98	120min	(Siddiqui, Manzoor, Mohsin, & Chaudhry, 2019)
4	rGO-MnO_2/BC	Wet impregnation	MB	99	75 min	(Tara, Siddiqui, Bach, & Chaudhry, 2020)
5	MnO_2@ZIF-8	Green method	RHB	96.0	80min	(Cao et al., 2022)
6	Zeolite-supported ZnO/Fe_2O_3/MnO_2	Wet impregnation	MB	93	120min	(Tedla et al., 2015)

7	Phosphorus doped MnO_2 with activated carbon	Hydrothermal	MO and RhB	96.31 and 97.57	180min	(Manikandan & Sasikumar, 2022)
8	Carbon nanosheet/MnO_2/BiOCl	Co-precipitation	RHB And MB	97 98	25min and 40min	(X. Hong et al., 2022)
9	MnO_2/bentonite	Co-precipitation	MB	87	2hr.	(Nakhaei et al., 2019)
11	Fe_3O_4/MnO_2/ZIF-8	Wet impregnation	RB19	99.5	60min	(Le et al., 2022)
	ZeoliteX supported MnO_2/Cu_2O	Wet impregnation	MB			Present work

As already been discussed various works have been done to enhance the performance of MnO_2 photodegradation activity. However, whether the cost of support material (Pargoletti et al., 2019), a small yield of catalyst prepared (Nakhaei et al., 2019), small degradation performance (Manikandan & Sasikumar, 2022), or a fast recombination rate (Thenmozhi, Harshavardhan, Kamala-Kannan, & Janaki, 2022) makes it still unable to overcome limitations related to MnO_2. This work collaborates the synergetic effect of the heterojunction MnO_2 with Cu_2O which is synthesized by the optimized amount and supported on ZeoliteX with a different ratio by the wet impregnation method. ZeoliteX is prepared by the alkali fusion method from easily accessible kaolin clay. Different techniques are used to characterize the synthesized samples, and the efficiency of the MB degradation is assessed. The pH impact, catalytic dose, initial dye dosage, and stability of the ternary composite are studied.

CHAPTER THREE

3. Methodology

3.1Chemicals and Materials

Chemicals and reagents were analytical grades and used without further purification. Manganese sulfate ($MnSO_4 \cdot H_2O$) (98% purity, India), potassium permanganate ($KMnO_4$) (99% purity), Copper sulfate pentahydrate ($CuSO_4.5H_2O$), and ascorbic acid($C_6H_8O_6$). Methylene blue($C_{16}H_{18}ClN3S$) is purchased from Sigma Aldrich, 98 % purity, India, NaOH(97 %, Mumbai, India), Ethanol (C_2H_5OH) (98 % purity), and distilled water was used throughout the experiment. The raw kaolin sample was collected from Di Yuan Ceramic Factory which is found in the Eastern Industry Zone, Ethiopia.

3.2 Experimental Procedure

3.2.1 Synthesis of Manganese dioxide (MnO_2)

MnO_2 nanoparticles were synthesized via the redox reaction process as previously reported (Lyu et al., 2020) with some modifications. Manganese sulfate and potassium permanganate ($KMnO_4$) were used as the starting materials. In the synthesis process, 0.05mol manganese sulfate dissolved into 70 ml of distilled water and further stirred for 30 min at 60°c. Then 70 ml of 0.035 mol potassium permanganate solution was dropped slowly into $MnSO_4$ solution and 1M NaOH was added drop wisely until pH maintained at 12. Then the solution was vigorously stirred for 1 hr. until the brownish color of the solution resulted. The resulting suspensions were aged for 12 hr. at room temperature and then filtered and rinsed with distilled water. The synthesized powder was dried at 100 ℃ for 8 hr. and calcined at 400°c in a muffle furnace for 3 hr. After being ground to a powder, the calcined MnO_2 was recovered from the furnace and used in future studies.

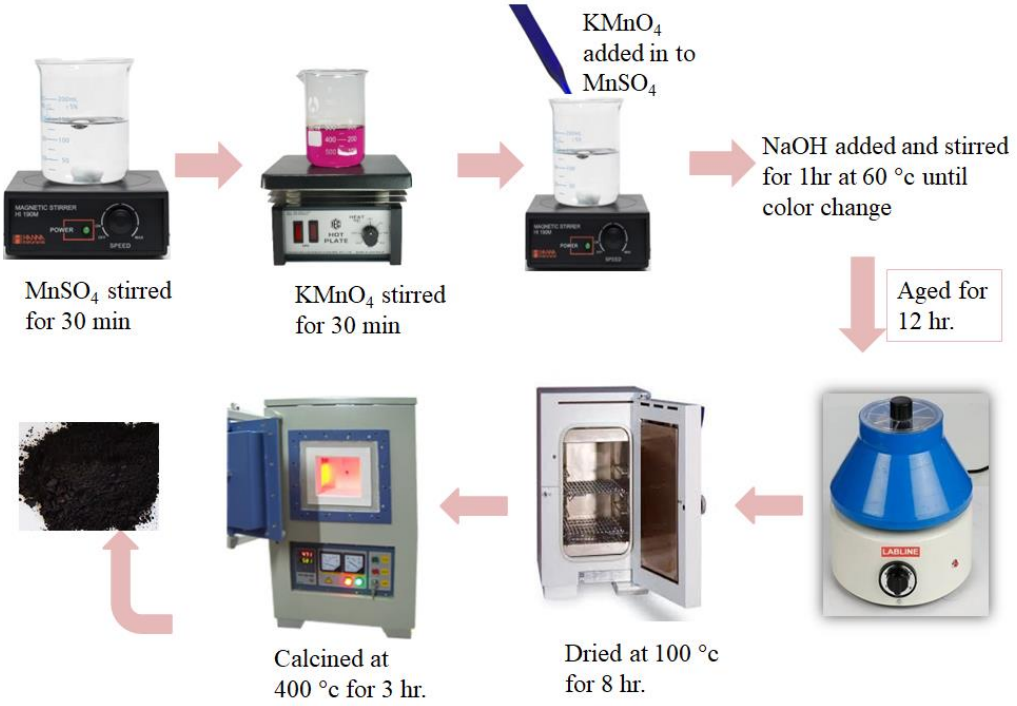

Figure 4: The schematics representation of the preparation of MnO_2

3.2.2 Synthesis of Copper dioxide (Cu_2O)

Cu_2O was prepared as reported (Paul et al., 2020)with little modification. In the particular procedure, 0.01 M $CuSO_4 .5H_2O$ was added into 50 ml distilled water and stirred for 20min to ensure adequate dissolution. It was followed by a solution of 0.004 M ascorbic acid in 20 ml distilled water added into the solution as a reducing agent. The pH of the prepared solution was raised to 10 by adding 1 M NaOH dropwise with continuous stirring. Then the solution was stirred for 1 hr. at 60°c until the solution becomes dark orange indicating the formation of Cu_2O. The precipitate was centrifuged and washed with distilled water followed by ethanol. After washing, the precipitate was recovered and dried in an oven at 60°C for 12 hr.

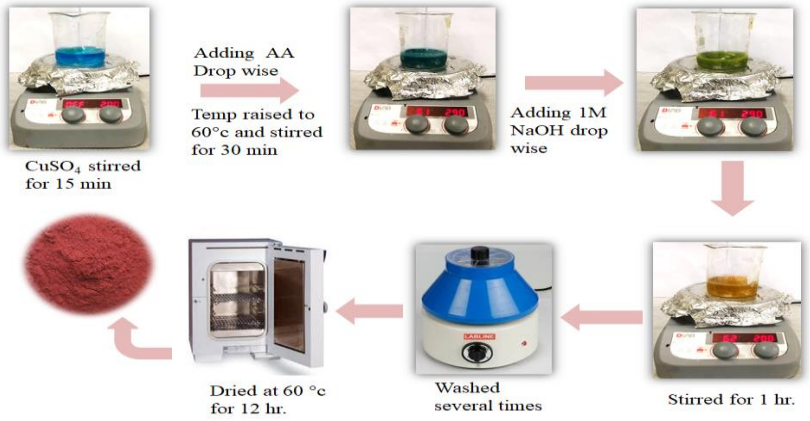

Figure 5: The schematics representation of the preparation of Cu_2O

3.3.3 Synthesize ZeoliteX

The raw kaolin sample was collected from Di Yuan Ceramic Factory. For the activation of kaolin same procedure as a previous report (Ayele, Pérez-Pariente, Chebude, & Díaz, 2016) with some modifications taken. First, the collected kaolin powder was crushed and sieved in homogenous size. Activation of the raw kaolin was carried out via mechanical method by crushing and mixing raw kaolin with pellet NaOH for 30 min followed by calcining at 600 °C for 1 hr. Whereas the ratio of NaOH to kaolinite was fixed at 1.2. The fused product was grounded in a mortar and further mixed with distilled water at 50 °C for 1 hr. under stirring at 500 rpm until the gel formed. The gel formed was then aged at room temperature for 8 hr. Crystallization was carried out in a water bath under static conditions for (3,6 and 9 hr.) at 95 °C. After cooling down at room temperature the solution was filtered out and washed repeatedly with distilled water until the pH gets neutral. Finally, oven dried for 12 hr. at 80 °C.

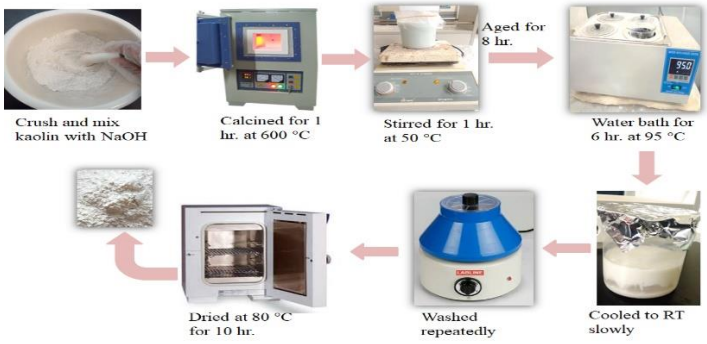

Figure 6: The schematics representation of the preparation of ZeoliteX from Kaolin clay

3.3.4 Synthesis of the MnO_2 and Cu_2O composite

was prepared as reported on previous works on metal oxide heterojunction (S. Wang et al., 2022). A wet impregnation process was used to synthesize the MnO_2/Cu_2O composite (Figure 7). Typically, the different weight ratio of as prepared MnO_2 sample was sonicated in 50 ml of distilled water for 40 min until a homogenous solution formed and then placed on the hot plate at 60 °C. While stirring $CuSO_4.5H_2O$ with different amounts added to each MnO_2 solution and stirred for 20 min. Ascorbic acid and NaOH were added and continued stirring for another 1 hr., namely 10% (1-MC), 30% (3-MC), 50% (5-MC), 70% (7-MC), and 90% (9-MC) MnO_2. The obtained solution was then dried for 12 hr. at 60 °C.

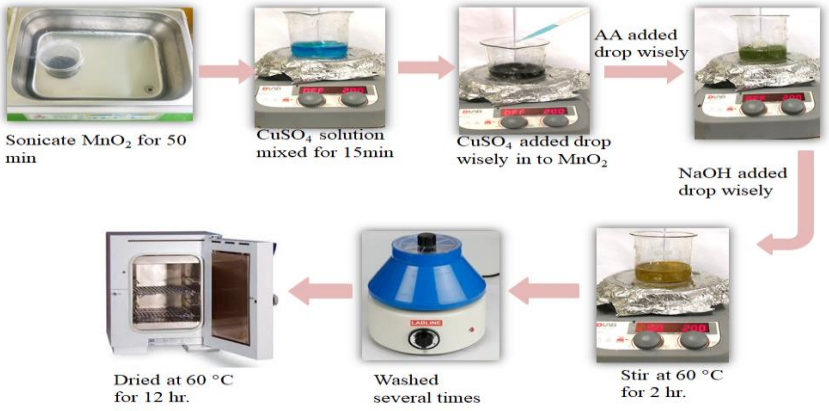

Figure 7: The schematics representation of the preparation of MnO_2 with Cu_2O heterojunction

3.3.5 Synthesis of zeoliteX supported MnO_2 / Cu_2O ternary composite

A wet impregnation process was used to prepare the zeoliteX/MnO_2/Cu_2O composite (Figure-8). Typically, the different weight ratio of as prepared zeolite sample sonicated in 25ml of ethanol solution for 40 min while stirring the synthesized and optimized heterojunction MnO_2/Cu_2O (7MC) in 25 ml of ethanol. Then stirred solution of MC was added to zeolite, namely 10% (1-ZMC), 20% (2-ZMC), 30% (3- ZMC), 40% (4-ZMC), and 50% (5- ZMC). The mixed solution was stirred for 2 hr. Finally obtained solution was then dried for 12 hr. at 60 °C. The dried sample was then calcined in a muffle furnace at 200°c for 3 hr. A similar procedure was used to prepare the zeoliteX-supported MnO_2 (ZM) and zeoliteX-supported Cu_2O (ZC).

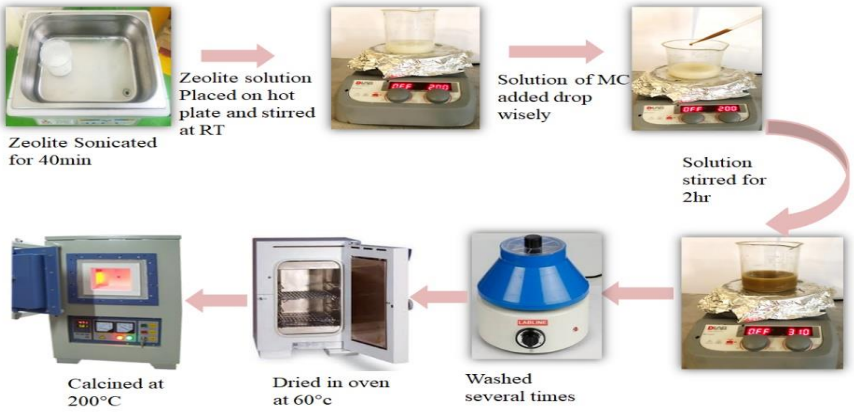

Figure 8: The schematics representation on the preparation of ZeoliteX supported MnO_2 with Cu_2O heterojunction

3.2 Characterization

The crystallinity, crystalline size, and phase of the catalyst were characterized by X-Ray Powder Diffraction (XRD) (Shimadzu XRD-7000). Fourier transform infrared (FTIR) analysis was done by using Spectrum 65 FT-IR (Perkin Elmer) in the range 4000 – 400cm^{-1} using KBr pellets. Differential Thermal Gravimetric (DTG) (Shimadzu DTG-60H) was used to know the thermal stability. Bruner-Emmett-Teller (BET) specific surface area measurements were recorded by N_2 adsorption using an ASAP 2020 HD88 surface area analyzer. Absorption properties of nanoparticles were measured by UV-Vis absorption Spectrum using a JASCOV-670UV-Vis at room temperature. The band gap of samples was determined by DRS using a tauc plot. Photoluminescence (PL) spectra of the prepared samples to investigate the recombination at a certain excitation wavelength were recorded using a fluorescence spectrophotometer (PE-LS55, USA) fitted with a xenon lamp at an exciton wavelength of 328 nm. Scanning Electron Microscopy (SEM) using JSM 6500F JEOL was used for morphology, analysis. A Shimadzu–3600 Plus UV–vis spectrophotometer was used to assess the MB dye degradation.

The electrochemical characteristics of the samples were studied using three-electrode quartz cells on an Electrochemical Potentiostate (Gamry Interface 1000) with 0.5 M Na_2SO_4 as an electrolyte solution (Lam et al., 2021). The EIS was obtained with a 10 mV AC voltage amplitude in the frequency range of 100 kHz to 0.1 Hz

3.3 Photocatalytic Activities

Photocatalytic activities of the as-synthesized samples were evaluated by the degradation of MB dye according to the method report (Uddin et al., 2012). All of the trials were carried out in the open room temperature. In each experiment, 0.04 g of metal oxide catalyst was added into 100 mL of MB solution (10 mg/L), followed by stirring for 30 minutes in the dark to validate the catalyst pollutant adsorption-desorption equilibrium. After 30 minutes of stirring in the dark, the light was turned on, and a 150 W halogen bulb was employed as the visible light source. 6 mL of the suspension was collected at predetermined irradiation times and centrifuged (4000 rpm, 10 min) to separate the photocatalyst particles. The MB concentration was evaluated by UV−visible Spectrophotometer (Shimadzu, UV-1650 pc) monitoring the absorption maximum at λmax = 664 nm.

The reusability of the Zeolite supported MnO_2/Cu_2O catalyst was also checked by dispersing 0.4 g of the catalyst in 500 mL MB (10 mg/L) solution. Then, the remaining solution was separated from the catalyst and the supernatant solution removed by decantation. The catalyst that remained in the bottom of the beaker left was reused for the next photocatalytic reaction by washing repeatedly and drying at 60 °C then run with a similar procedure five times. The degradation efficiency (η) of the MB dye was calculated as follows:

$$\eta = ((C_O - C_t)/C_O) \times 100\% \quad (1)$$

Where C_o and C_t are the concentrations of the MB dye at the initial and specified irradiation times, respectively.

CHAPTER FOUR

4. Results and Discussions

4.1. Structural Characterization by XRD

The crystal structure, phase purity, and crystalline size of synthesized material (MnO_2, Cu_2O, ZeoliteX, ZM, MC, ZM, and ZMC) were analyzed by powder X-ray diffraction (XRD). The diffraction peaks of pure MnO_2 as shown in Figure 9 (a) located at 12.94°, 18.34°, 21.58°, 26.1°, 28.78°, 33.12°, 37.66°, 42.14°, 43.98°, 47.74°, 49.90°, 56.44°, 60.26°, 69.74°, 71.34°, 73.72° and 78.8° belongs to (110), (200), (202), (332), (310), (220), (211), (301), (330), (400), (411), (600), (521), (541), (222), (730) and (324) facets, respectively. It is in good match with XRD standard card (JSPDS File No. 44-0141) and space group I4/m. This indicates that tetragonal crystals of α-MnO_2 were effectively synthesized. Additionally, no impurity-related peak was seen, confirming the good purity of MnO_2 (Wan et al., 2019).

X-ray diffraction patterns of Cu_2O particles are shown in Figure 9 (b) and well-defined peaks from Cu_2O were located at 29.6°,36.4°,42.3°,52.3°,61.5°,73.6°,and77.45°which belongs to (110), (111), (200), (211), (220), (311) and (222) in good agreement with XRD standard card (JCPDS File No. 005-0667) and crystallizes in cubic Pn-3m space group (Y. C. Chen et al., 2019; Plascencia-Hernández et al., 2019).

Figure 9(c) shows the X-ray diffraction pattern of ZeoliteX crystallized for 6hr. and found in total agreement with the XRD standard card (JCPDS File No.-038-0237). The diffraction peaks are shown at 12°,15.5°,18.5°, 20.05°, 23.5°,26.7°, 29.4°, 30.7°,34.1°,37.5°,41.2°,53.5°and57.9° corresponds to (220), (311), (331), (440), (533), (642), (330), (751), (840), (664), (500), (510) and (624) respectively (Ke, Shen, & Yang, 2019).

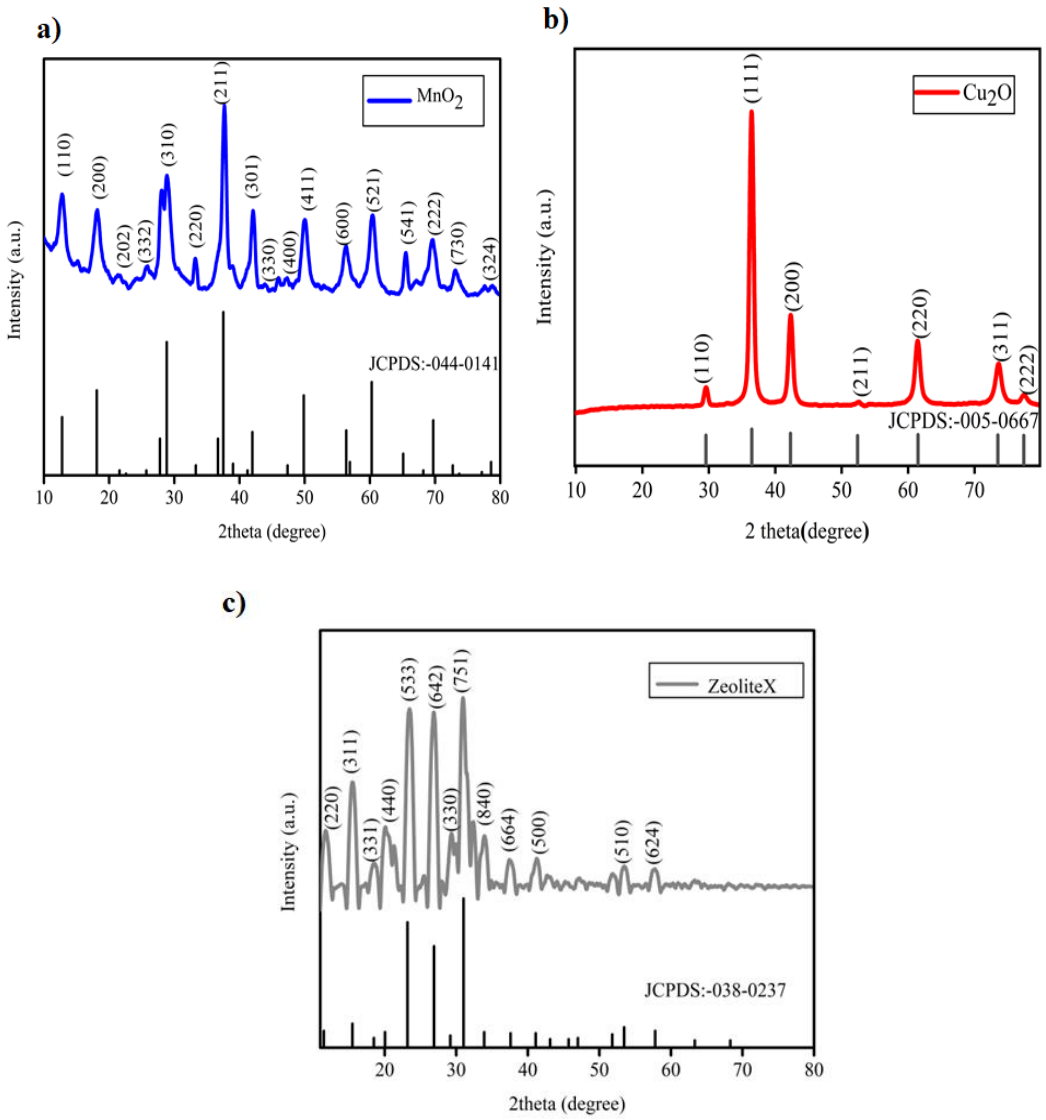

Figure 9: XRD pattern of a) MnO_2 b) Cu_2O c) ZeoliteX

Figure 10 depicts the XRD patterns of MnO_2, Cu_2O, ZeoliteX, ZM, MC, and targeted ZMC composite catalysts with varying weight percent of ZeoliteX. The equivalent diffraction peaks of MnO_2, Cu_2O, and ZeoliteX are visible in the ZeoliteX/MnO_2/Cu_2O composite display. This means that the interaction of Cu_2O and ZeoliteX as a support does not affect MnO_2 initial lattice structure. Furthermore, no additional peak is visible in any of the samples. However, the diffraction peaks of ZeoliteX steadily strengthened at the cost of the heterojunction peaks and peaks gets broader as the zeolite concentration increased.

Also, it was observed diffraction peaks of Cu_2O at low content are stronger than MnO_2, which may be related to the high dispersion of Cu_2O which makes it easily detectable by XRD (Uddin et al., 2017).

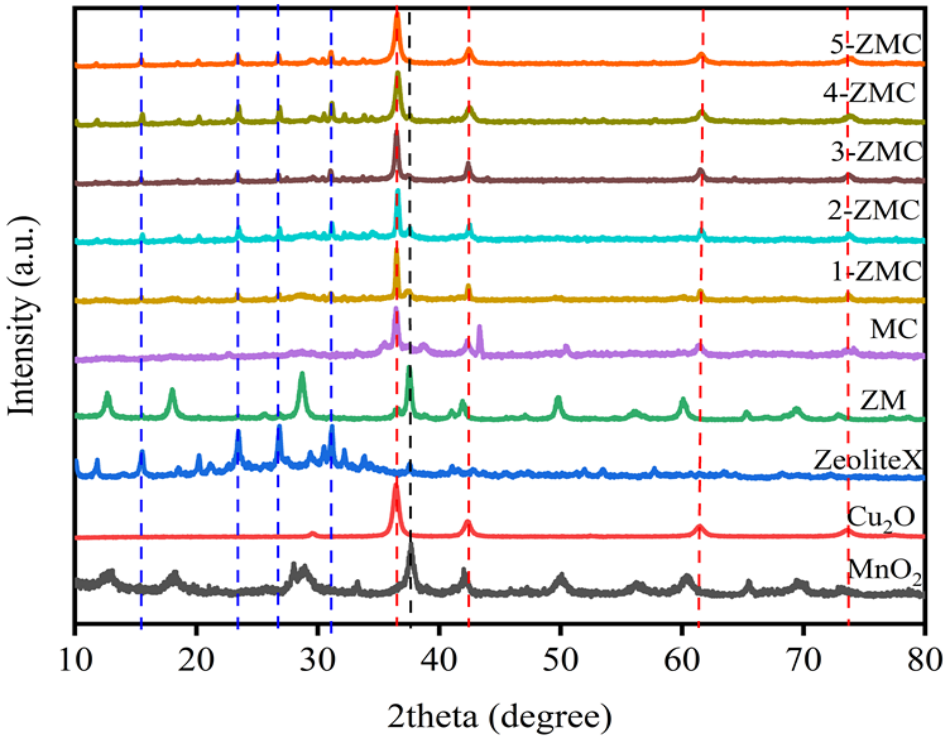

Figure 10: XRD pattern of MnO_2, Cu_2O, ZeoliteX, ZM, MC, ZC, 1-ZMC, 2-ZMC, 3-ZMC, 4-ZMC and 5-ZMC

The crystallite size can be calculated by using Debye–Scherer strategy of equation (2):

$$D = \frac{0.9\lambda}{\beta Cos\theta} \qquad (2)$$

Where the crystal size is D, the X-ray wavelength is (1.5418 Å), the full-width half maximum of the diffraction peak is the β and the scattering angle is the θ (Rodriguez, Puzenat, & Thivel, 2016). As shown in Table 4 the crystalline size (D) of MnO_2, Cu_2O, and ZeoliteX were calculated by using equation (2) and resulted in 27.36 nm, 21.1 nm, and 11.5 nm respectively. The crystallite size of MnO_2 increased when it forms a composite with Cu_2O (MC) since heterojunction can act as a nucleation site for the growth of the metal oxide crystals. It was confirmed by the peak getting more sharper (S. Wang et al., 2022).

In the case of single MnO_2 or the heterojunction MC supported on ZeoliteX, the crystallite size gets reduced. As the amount of ZeoliteX in the ternary composite the peak gets more broader confirming the reduction of crystallite size. It occurs due to ZeoliteX having a high surface area the metal oxide MnO_2 or the heterojunction MC gets well dispersed so it will have limited availability for neighboring which gives a high surface area to volume ratio than clusters and agglomerates. So the probability to increase in size would be low (Luévano-Hipólito, Torres-Martínez, & Fernández-Trujillo, 2021). This shows that using ZeoliteX as a support can prevent MnO_2 and Cu_2O crystals from growing to their final crystal sizes (G. Zhang, Sun, Hu, Song, & Zheng, 2017).

In general, the high surface area of the ZeoliteX material creates a lot of active sites for the deposition of metal oxide particles. As a result, smaller, more distributed metal oxide nanoparticles are created, which reduces the heterojunction's overall crystallite size.

Table 4:The average crystallite size, corresponding theta, FWHM for MnO_2, Cu_2O, ZeoliteX, ZM, MC,1-ZMC,2-ZMC,3-ZMC,4-ZMC,5-ZMCfrom XRD pattern.

Sample name	Theta(degree)	FWHM Radians (β)	βcosθ	D-size (nm)
MnO_2	37.67	5.067×10^{-3}	5.066×10^{-3}	27.36
Cu_2O	36.45	0.01108	0.0111	21.1
ZeoliteX	28.5	0.0217	0.222	11.5
ZM	37.65	9.62×10^{-3}	9.6×10^{-3}	14.44
MC	36.45	4.06979×10^{-3}	4.0694×10^{-3}	30.1
1ZMC	36.48	6.61×10^{-3}	6.6×10^{-3}	20.97
2ZMC	36.5	7.078×10^{-3}	7.077×10^{-3}	19.5
3ZMC	36.48	9.286×10^{-3}	9.285×10^{-3}	14.9
4ZMC	36.5	0.0128	0.0103	13.44
5ZMC	36.5	0.01119	0.0112	12.38

4.2. Thermo-Gravimetric Analysis (TGA)

Thermal evaluation TGA/DTA is a crucial experimental technique that is frequently used to examine how thermally degraded synthesized materials are (Raza, Faisal, Owais, Bahnemann, & Muneer, 2016). Figure 11 (a, b, c) displays the TGA and DTA traces of MnO_2, Cu_2O, ZeoliteX, Kaolin, 3-ZMC, and thermal stability comparison of MnO_2 with 3-ZMC samples that were heated from 0 to 800 °C at a rate of 10 °C/min.

In the TGA curve of pure MnO_2, the first weight loss of 0.32mg was observed in the range between 31 and 210 °C and the corresponding endothermic peak was observed at 50 °C which is due to the release of adsorbed water and some dust on the surface (Worku, Ayele, & Habtu, 2021). The next weight loss of 0.13 mg ranges from 210 °C to 390 °C was for a loss of strongly bonded organic then it was stable up to 600 °C but further heating resulted in a high amount of weight loss of about 0.55 mg due to the phase change of MnO_2 to Mn_2O_3. Moreover, in the DTA curve of pure MnO_2 the two sharp exothermic and endothermic peaks that arise at 623 °C and 641 °C, respectively might be due to a variation in crystallinity or possibly due to a phase transition in the NPs (Durai, Prasad, Kumar, Muthuraj, & Jothy, 2018). A final weight of 8.106 mg was obtained from the initial weight of 9.147 mg which corresponds to 11.38 % weight loss when heated to 800 °C (Figure 11(a)).

As shown from the TGA/DTA of the Cu_2O Figure 11(b) initial weight loss of about 0.428 mg occurred in the range between 20 to 204 °C supported by exothermic peaks from DTA at 206 °C which is caused by evaporation of water and organics absorbed on the surface of the samples. It remained stable up to 215 °C but when further heated a positive slope in the TGA curve was shown which indicates the weight gain by 0.29 mg as a result of oxygen taken into Cu_2O as result oxidized to and conversion of Cu_2O (copper(I) oxide) to CuO (copper (II) oxide) takes place. The result suggests that the oxidation of Cu_2O might be initiated around 215 °C and fully completed at 365 °C for the conversion from Cu_2O to CuO. Heat is released during this exothermic reaction which is supported by DTA data for an exothermic peak at 317°C. (Wei, Yang, Pang, & Ge, 2018).

The DTA/TGA curves of the synthetic ZeoliteX are shown in Figure 11 (c). The DTA curve of zeolite displays a characteristic endothermic minimum below 200°C, caused by dehydration and from TGA resulting in 0.196 mg weight loss. The second weight loss of 1.02 mg occurred between 110 °C and 430 °C attributed to the desorption of the remaining water that may place in the pore enclosed in the zeolite matrix supported by an exothermic peak in the temperature ranges from 250 to 600 °C. The small endothermic peak in the DTA curves at 590 °C corresponds to the effect of high temperatures that cause sodium cations to begin to migrate outside of the zeolite structure, which causes the zeolite framework to disintegrate. As a result, an amorphous that lacks the ordered structure of the original zeolite may emerge which may have an impact on the zeolite's characteristics and uses (Nicholas Mulei Musyoka, 2012).

To synthesize ZeoliteX the raw kaolin clay needs to be calcined, activated, and dust-free, so thermal analysis of the material is crucial. According to TGA analysis from Figure 11(d), the virgin raw kaolin's (9.136 mg) first weight loss of 0.098 mg occurred from 18 up to 114 °C attributable to the release of moisture and loosely bound absorbed water from the surface. Also, endothermic peaks at 55 and 123 °C from DTA support the data. The second weight loss of 0.34 mg amount occurred between 123 and 185 °C and from DTA small endothermic peaks were shown at 277 °C and 453 °C that related to loss of dust and water in the pore site, after that it remained stable up to 480 °C and more significant weight drop by 0.41 mg occurred between 480 °C and 560 °C that supported by endothermic peak at 526 °C which indicates a shift as a result of the structure's dissociation via de hydroxylation to meta kaolin which has an amorphous structure and very reactive (Caponi et al., 2017). Thermal analysis of 3-ZMC shows weight loss up to 215 °C which is then stable up to 310°C. Further heating result in gain in weight that indicate phase transition of Cu_2O to CuO (Figure 11(e)) (Nicholas M Musyoka, Petrik, Hums, Kuhnt, & Schwieger, 2015).

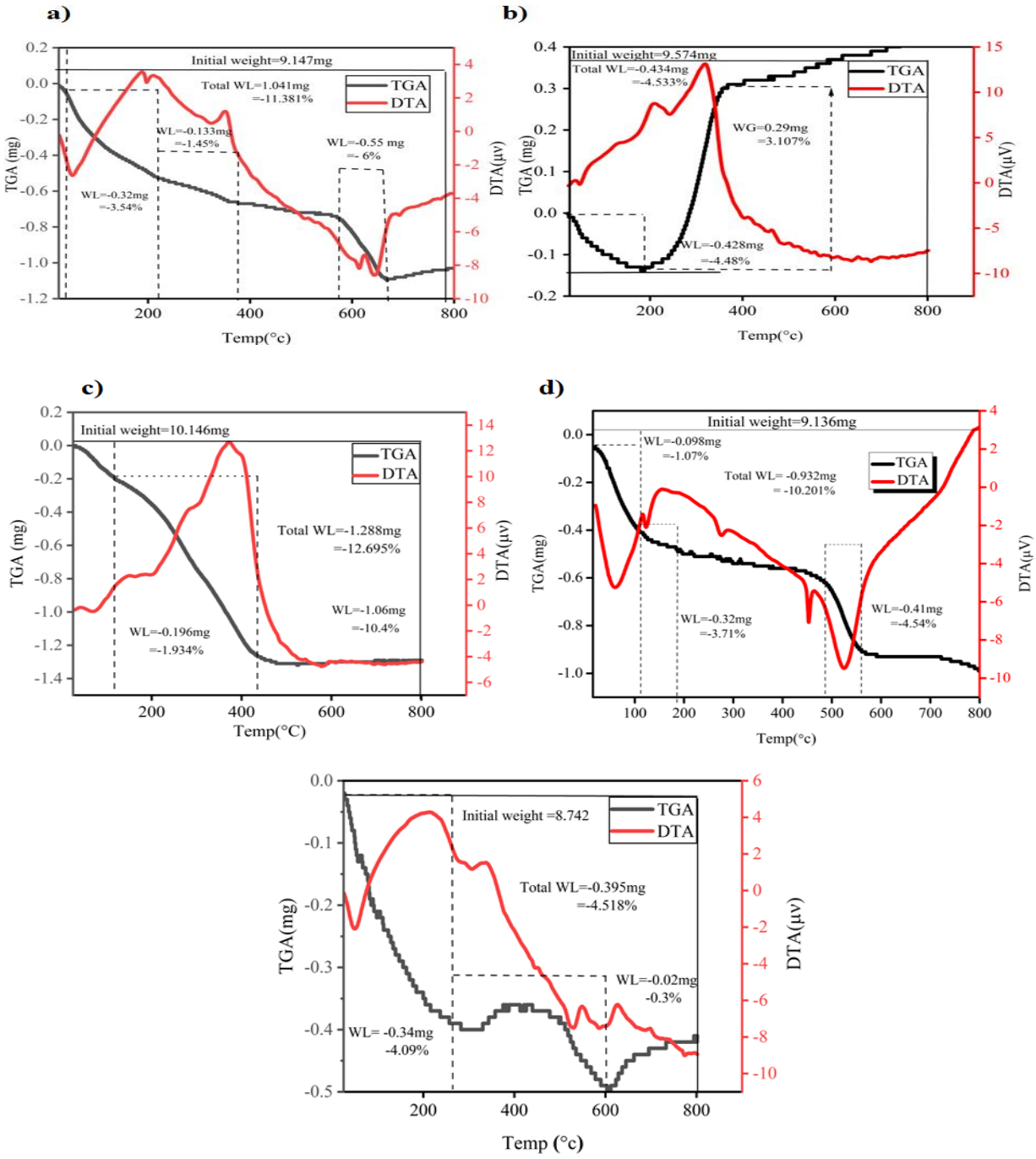

Figure 11: The TGA-DTA graph of synthesized (a)MnO_2 (b)Cu_2O (c) ZeoliteX (d) Kaolin (e) 3-ZMC

4.3. Uv-Vis diffusion reflectance spectra (Uv–Vis DRS)

The energy band gap of samples was evaluated by using Uv-Vis diffusion reflectance spectra. As shown in Figure 12 the band gap was calculated by using a tauc plot which resulted in 1.763 for MnO_2 which is close to previous work (Xiang Li, Fang, Qian, & Tian, 2022). For Cu_2O, MC, ZM, and 3-ZMC resulted in 2.43, 2.38, 2.1, and 2.45 eV respectively.

For sample MC heterojunction made with Cu_2O tuned the band gap since the creation of a metal oxide heterojunction causes a band bending effect at the interface that would enhance the separation and migration of photo-generated charge carriers, leading to higher photocatalytic activity and improved efficiency (Salari & Yaghmaei, 2020).

In Figure 12 (e), the effects of ZeoliteX support on heterojunctions were specifically displayed. The reduction in crystallite size with the high surface area due to ZeoliteX support results in increasing the heterojunction bandgap from 2.38 eV to 2.45 eV (Karimi-Shamsabadi, Behpour, Babaheidari, & Saberi, 2017; Singh, Goyal, & Devlal, 2018).

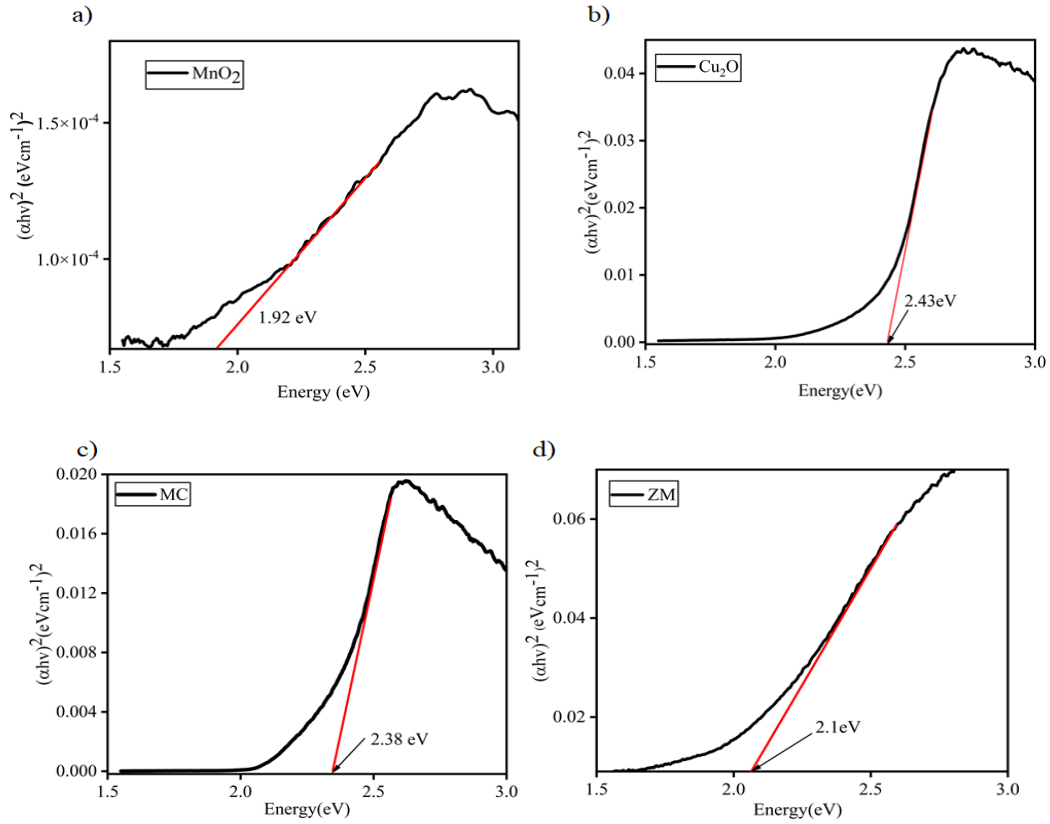

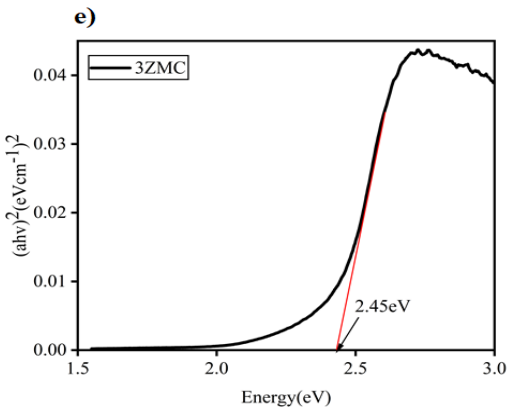

Figure 12: Talc plots for the optical energy gap calculation of (a) MnO_2 (b) Cu_2O (c) MC (d) ZM (e) 3-ZMC

4.4. Fourier Transform Infrared Spectroscopy (FT-IR) Analysis

The FT-IR spectrum was used to identify the functional groups and other impurities present in the final product which was accomplished within 400 to 4000 cm^{-1} ranges of the electromagnetic spectrum. In Figure 13, the FTIR spectra of MnO_2, it was revealed that OH stretching and bending vibrations are represented by a broad band centered at 3416 cm^{-1}, a sharp band at 1627 cm^{-1}, and 1080 cm^{-1} which suggests that residues of adsorbed water are vibrating along the O-H direction. The absorption band located at 524 cm^{-1} was attributed to the typical stretching collision of O–Mn–O, which indicated the presence of MnO_2 in the prepared sample (Worku et al., 2021).

From FTIR spectra of Cu_2O the O-H stretching vibration, or (OH), is responsible for the strong peak at 3419 cm^{-1} (Joshi, Ippolito, & Sunkara, 2016).

The weak bands at 1620 and 1380 cm^{-1} are assigned to the –OH bending vibrations. While the band for the C–O stretching vibrations are observed in the 1070 cm^{-1} region. Moreover, the very strong band at 622 cm^{-1} is attributed to the stretching vibration of copper (I)–O (Cu_2O) (C. Chen et al., 2013).

The creation of the zeolite structure is shown by the first infrared peak patterns in FTIR spectra (Figure 13). Transmittance peaks were measured at 461 and 668 cm^{-1}, indicating the band of internal deformation vibration modes of T-O-T bridges.

More sensitive to the Si/Al ratio is the band connected to the asymmetric external vibration of the double four-ring zeolite structure, which is 562 cm^{-1}. At 752 cm^{-1}, the band of valence T-O-T vibrations reaches its maximum. Lower wave numbers (976cm^{-1}) are where the internal vibration of T-O asymmetric stretching reaches its climax. The O–H group of H_2O is observed to be responsible for the formation of a large absorption peak at 3451 and a sharp peak at 3780 $cm^{-1.}$ 1650 cm^{-1} (T. Hu, Gao, Liu, Zhang, & Meng, 2017; Tsitsishvili et al., 2019).

The ZMC-4 composite's FTIR spectra show bands associated with the relevant Zeolite, MnO_2, and Cu_2O functional groups after the inclusion of these materials, confirming the successful production of the Zeolite, MnO_2, and Cu_2O composite as shown in Figure13.

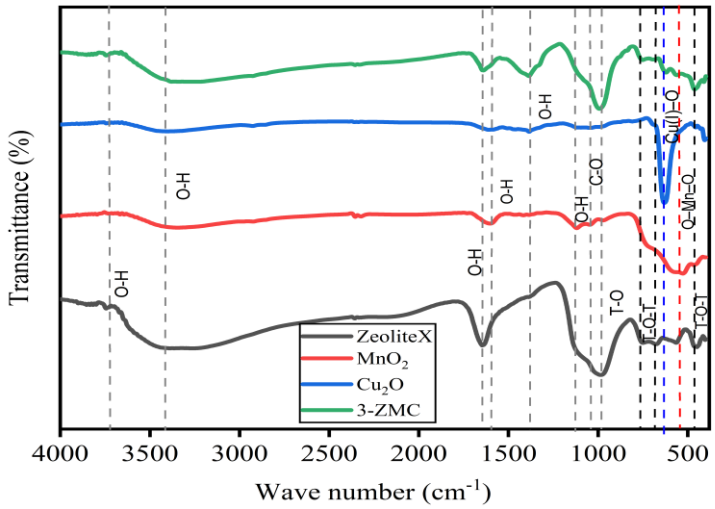

Figure 13: The FTIR spectra of ZeoliteX, MnO_2, Cu_2O, and 3-ZMC

4.5. Scanning Electron Microscope (SEM) Analysis

To study the surface morphology for MnO_2 Cu_2O, ZeoliteX, MC, and 3-ZMC nano particle Scanning Electron Microscopy (SEM) was taken. As shown in Figure 14 (a) agglomerated cactus-like morphology is visible in the SEM images of α-MnO_2. Cactus-like morphology, which imitates the form and shape of cacti plants has several benefits that make it appealing as a photocatalyst including a high surface area to volume ratio, and their structures spines, and grooves can improve light trapping. The morphology of ZeoliteX shows an spherical shape with small pore sites (Figure 14 (b)) (Parsapur & Selvam, 2018).

The heterojunction (7MC) morphology consists of agglomerated cactus-like and spherical morphology with large size emerged in Figure 14(c) and in comparison, the ternary composite (3-ZMC) has the morphology of dispersed, less agglomerated, and porous structure that indicates the support material ZeoliteX provide an active site for dispersion of the heterojunction and in turn result in a reduction of their size (Figure 14 (d)) (Derikvandi & Nezamzadeh-Ejhieh, 2017a).

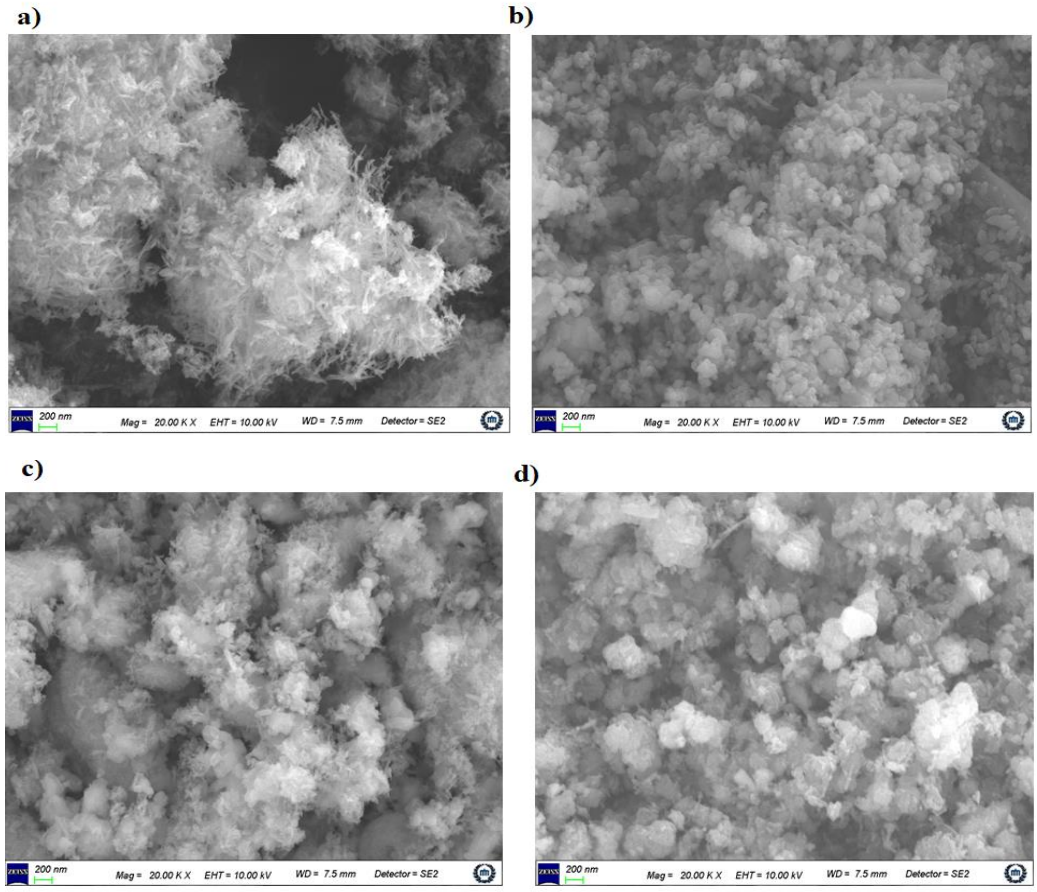

Figure 14: The SEM image for nano particle of (a) MnO_2 (b) ZeoliteX (c) 7MC (d) 3-ZMC

4.6. Brunauer-Emmett-Teller (BET) Analysis

As shown in Table 5 the BET measurement specific surface area of MnO_2 was increased when it makes heterojunction with Cu_2O (7MC) from 459.796 m^2/g to 480.420 m^2/g which implies the composite provides more active site (Jing et al., 2022).

In comparison, ZeoliteX supported heterojunction (3-ZMC) had shown a larger specific surface area than the heterojunction which enhances from 480.42 m²/g to 523.12 m²/g. The outcomes showed that the catalyst's specific surface area increased in the presence of heterojunction with Cu_2O and the support ZeoliteX. This improved surface area allowed for more active locations and organic pollutant adsorption on catalyst surfaces (G. Zhang et al., 2017). These designs ultimately enable the catalyst to perform efficient MB degradation in a shorter amount of time.

Table 5: BET data of MnO_2, 7MC, and 3-ZMC

	MnO_2	7-MC	3-ZMC
Specific surface area (a_s)	459.796 (m²/g)	480.420 (m²/g)	523.120 (m²/g)
Total pore volume ($\frac{Po}{P}$)	1.741 (cm^3 /g $^{-1}$)	1.794 (cm^3 /g $^{-1}$)	2.003 (cm^3 /g $^{-1}$)
Mean pore diameter	1.45 (nm)	1.4 (nm)	1.32(nm)

4.7. Photoluminescence (PL) Analysis

The MnO_2, ZM, MC, and 3-ZMC photocatalysts' photoluminescence (PL) spectra were measured at room temperature at the excitation wavelength of 380 nm to examine the extent of recombination of the photo-generated e^-/h^+ carriers in the prepared samples and the impact of heterojunction and support on the Photoluminescence of MnO_2 (Panimalar et al., 2020).

As shown in Figure 15 MnO_2 exhibits the highest PL spectra due to its high recombination property. When MnO_2 is coupled with Cu_2O and made the heterojunction 7MC the recombination rate is greatly reduced due to the built electric field generated at the interface of the p-n heterojunction and also direct Z-scheme improves the separation and transmission of photogenerated carriers across the junction (M. Zhang et al., 2021).

Electrons in the n-type semiconductor's conduction band are transported to the p-type semiconductor valance band. Similar to this, the holes in the p-type semiconductor's valence band are transported to the conduction band of the n-type semiconductor material. This mechanism reduces the likelihood of recombination of holes in VB and electrons in CB of n-type and p-type semiconductors respectively which increase the effectiveness of the composite (Xia et al., 2018).

Also, ZeoliteX support effect on reducing of recombination rate of MnO_2 was shown from ZM by lower emission intensity than single MnO_2, since ZeoliteX has a low Si/Al ratio it will result in more uncoordinated Al atom on zeolite framework which are lewis acid site that interacts with electron-rich species and reduces recombination rate. Along with the controlled size and distribution of the MnO_2/Cu_2O particles on the ZeoliteX surface, the confinement effect may also restrict their mobility and prevent recombination (Karimi-Shamsabadi et al., 2017). Finally, very small emission intensity for ZeoliteX supported MnO_2/Cu_2O composite due to the impact of both heterojunction and ZeoliteX support.

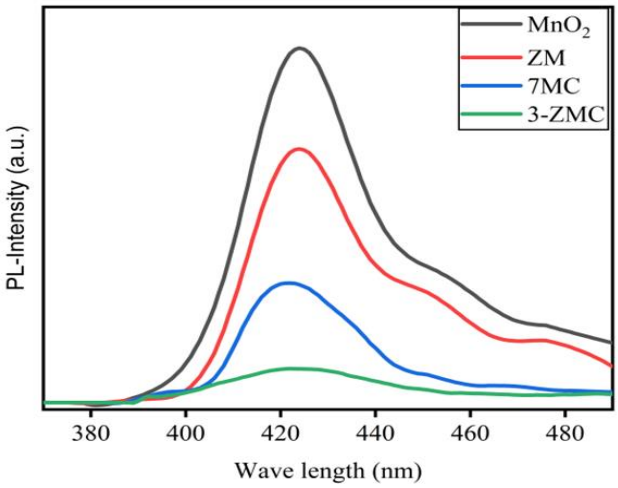

Figure 15: Room temperature PL spectra of MnO_2, ZM, MC and 3-ZMC

4.8. Electrochemical Impedance Spectroscopy (EIS) Study

Using electrochemical impedance spectroscopy (EIS), more investigation on the dynamics of interfacial charge transfer in the photocatalyst was done. The Nyquist plot (a graphical representation of the impedance of the system as a function of frequency) EIS of MnO_2, 7MC, ZM, and 3ZMC samples was carried out as shown in Figure 16 to better understand the impact of making heterojunction and the support effect on the separation of photogenerated electron-hole pairs. Charge carrier separation is shown by an arc radius diagram which corresponds to the size of the charge transfer resistance and the separation efficiency of the photoelectron-hole pair (L. Zhao et al., 2022).

Since the arc radius on the EIS spectra indicates the resistance of the interface layer at the electrode surface the smaller arc radius confirms higher charge transfer (Derikvandi & Nezamzadeh-Ejhieh, 2017b).

The EIS findings confirm the idea that the 3ZMC catalyst increased photodegradation activity as a result of its improved charge separation efficiency. The composites have the smallest EIS semicircle radius during interfacial transport when compared to bare MnO_2, indicating the lowest impedance, allowing for the fast transfer of photo charges which will prolong photocarrier lifespan and improve the effectiveness of photocatalysts (G. A. Ali, Yusoff, Algarni, & Chong, 2018). This analysis was also confirmed by the photoluminescence result.

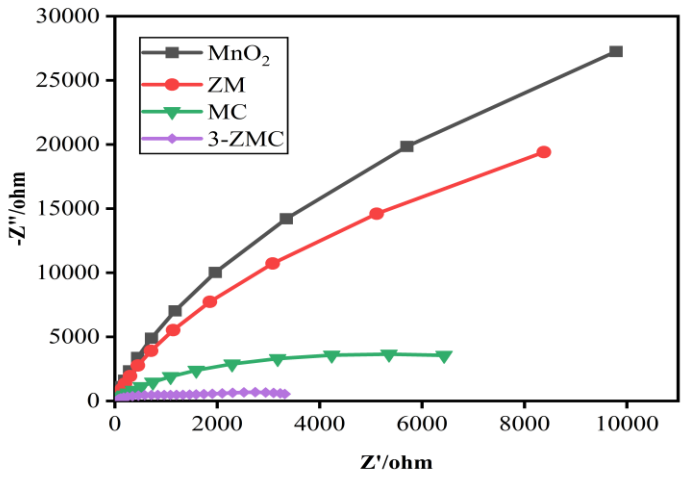

Figure 16: the Nyquist plot EIS of MnO_2, ZM, MC and 3-ZMC

4.9. Photocatalytic Activity Evaluation

To check the photocatalytic degradation efficiencies of pure MnO_2, heterojunction of MnO_2 with Cu_2O at different concentrations and zeolite supported heterojunction with a range of ZeoliteX amount, Methylene blue (MB) dye which is a major pollutant in water discharged by factories in the textile industry was chosen as the model of organic pollutant while experimenting visible light irradiation.

Figure 17 (a, b, c) shows the UV-Vis absorption of MnO_2, Cu_2O, and ZeoliteX photocatalysts respectively, where a peak of absorbance at 664 nm for the UV-Vis of the MB solution.

This presence of the peak is attributed to the absorbance of the transitions of the MB (Santhoshkumar & Murugan, 2021). Except for the ZeoliteX and ZM samples (the whole reaction takes place without light), the degradation was divided into two phases: the dye/catalyst solution was kept under continual sonication for 30 minutes in the first phase (without turning on the visible light). While the second stage (the visible light on), has an 80 min reaction time under light. The reaction takes place at room temperature, with pH 7 within. The degradation efficiency (η) of the synthesized sample can be achieved by the following equation:

$$\eta = \frac{C0-Ct}{c0} x\ 100\ \% \qquad (3)$$

Where, C_0 and C_t are the concentration of the dye at the irradiation for time, "0" and "t" minutes, respectively (Yi He, Jiang, Chen, & Zhang, 2018). In the case of pure ZeoliteX, full adsorption was taken place under a dark environment. The photocatalytic activity of pure MnO_2 was 47 % during 80 minutes of reaction time. The high agglomeration and recombination rate of MnO_2 is the reason for the low degradation rate. Cu_2O and ZeoliteX were also calculated and performed at 55%, and 52 % degradation of dye respectively.

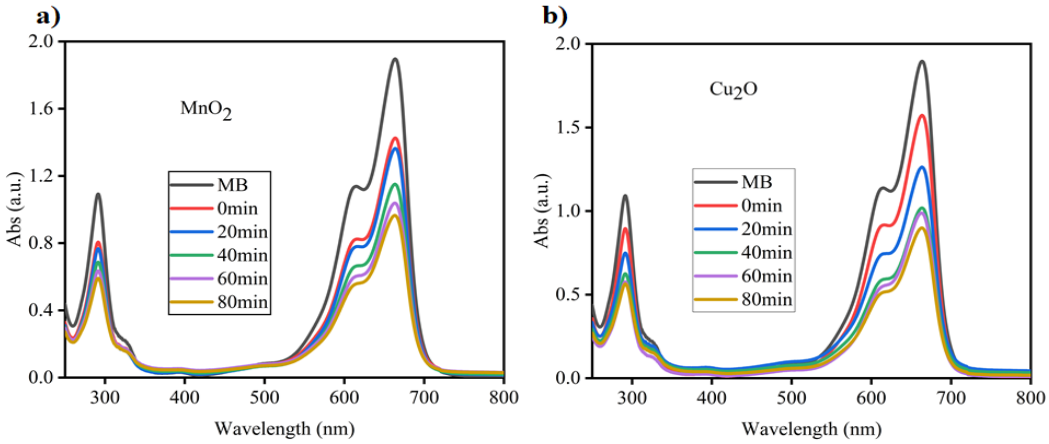

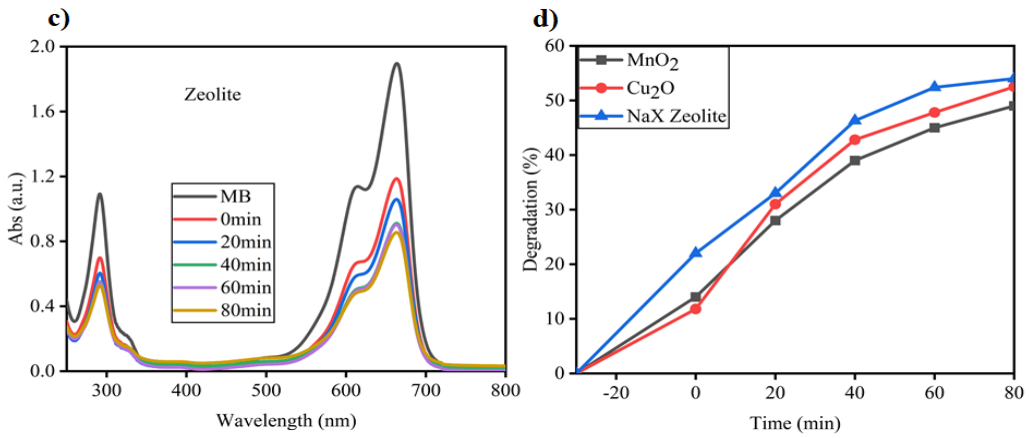

Figure 17: Photocatalytic Activity of (a)MnO_2, (b)Cu_2O, (c) ZeoliteX (d) percentage degradation

To analyze the effect of ZeoliteX on the photodegradation of single metal oxide MnO_2 and Cu_2O were conducted. As shown in Figure 18 (a, b) sample ZM and ZC photodegradation performance enhanced which is related to the ZeoliteX support that provides more surface area, more interaction of reactive species with MB due to the more active site provided, and decrease agglomeration rate of metal oxides. Also, some uncoordinated Al^{3+} on the ZeoliteX surface play role in reducing the recombination rate of electron and hole pairs that enhance the photodegradation performance (Karimi-Shamsabadi et al., 2017).

On the other hand, the heterojunction formed between MnO_2 and Cu_2O increased the performance of single metal oxide MnO_2 which is due to the band alignment that reduces the recombination rate of electron and hole pairs and enhanced active site (Salari & Hosseini, 2021).

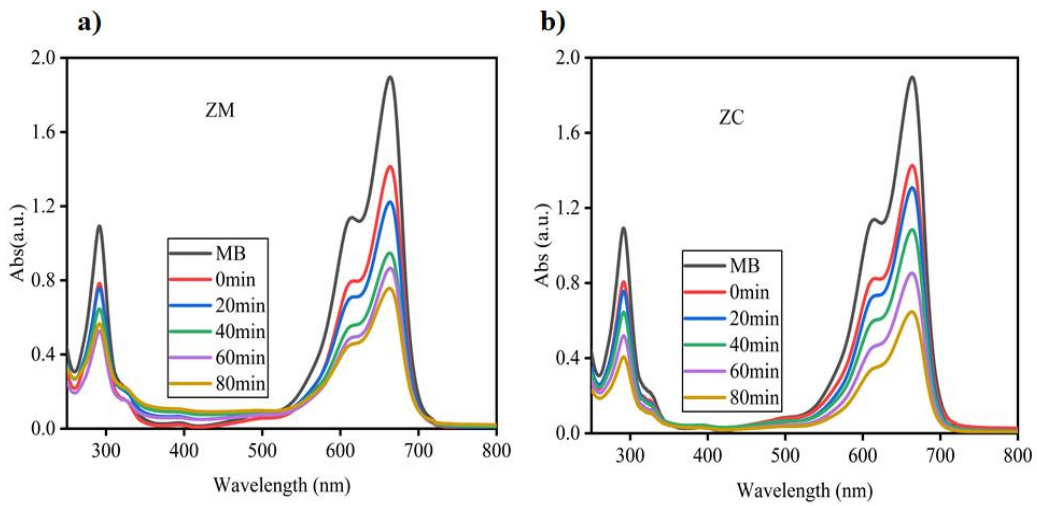

Figure 18: Photocatalytic Activity of (a) ZM and (b) ZC

Different concentrations of heterojunction's photocatalytic activity in Figure 19 (a-g)1MC, 3MC, 5MC, 7MC, and 9MC catalysts were crucial in determining how Cu_2O affected the performance of the MnO_2 Catalyst. In comparison to MnO_2, 1MC, 3MC, 5MC, and 9MC samples (49%, 63%, 66%, 70.1%, and 72.9%, respectively), it is shown that the 7MC sample has the highest photocatalytic activity (74.7%) throughout an 80minute reaction period.

The band alignment of the two materials at the heterojunction can prevent the recombination of photo-generated electron-hole pairs specially the direct Z-scheme provides suitable band alignment that results in better redox reaction in turn a great enhancement of photodegradation. In addition, the formation of a heterojunction can lead to more active sites for catalysis to occur. This was shown by the enhancement of the adsorption of pollutants in the first stage photocatalytic degradation process (Salari & Hosseini, 2021).

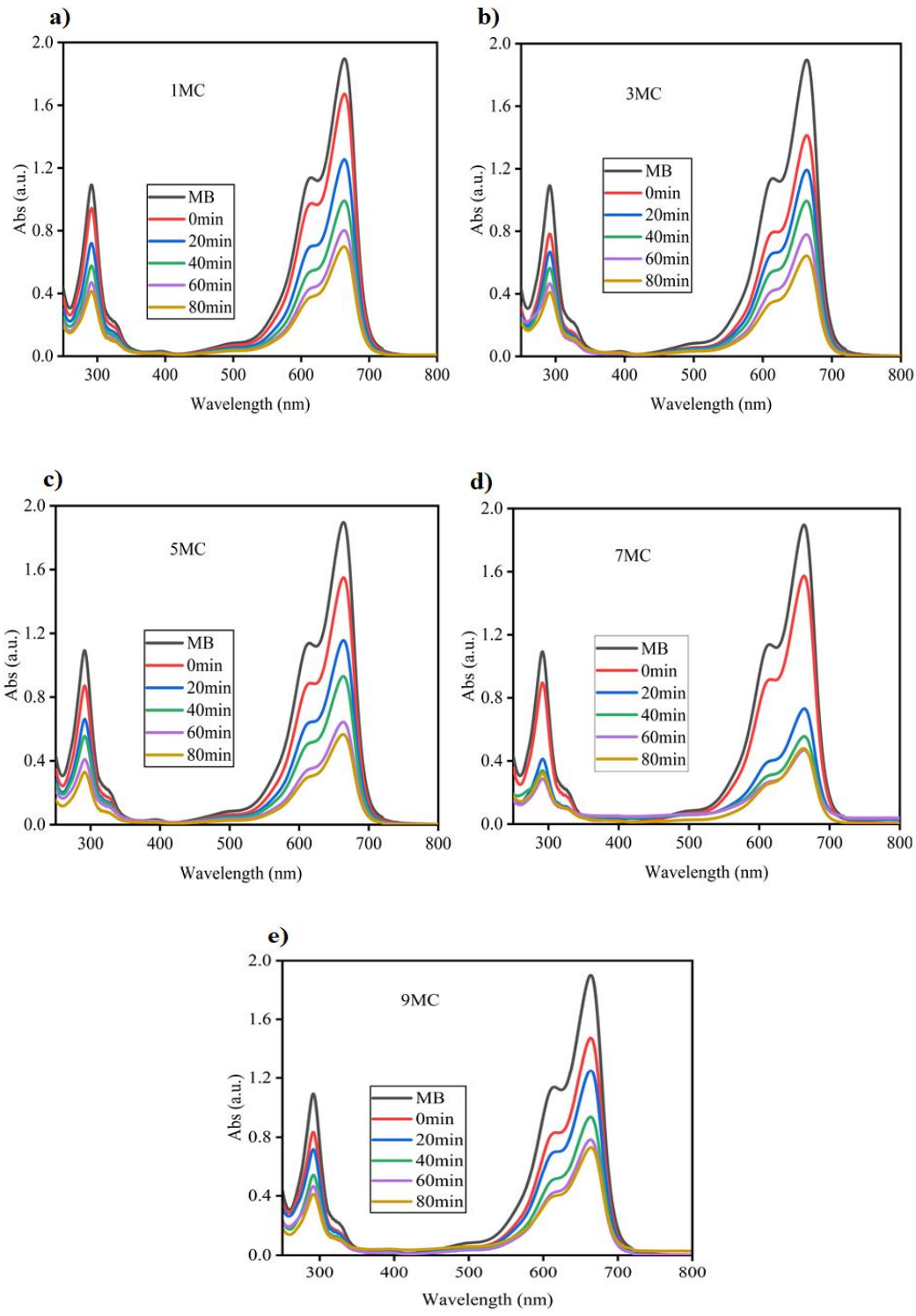
a)
1MC
b)
3MC
c)
5MC
d)
7MC
e)
9MC
MB
0min
20min
40min
60min
80min
Abs (a.u.)
Wavelength (nm)

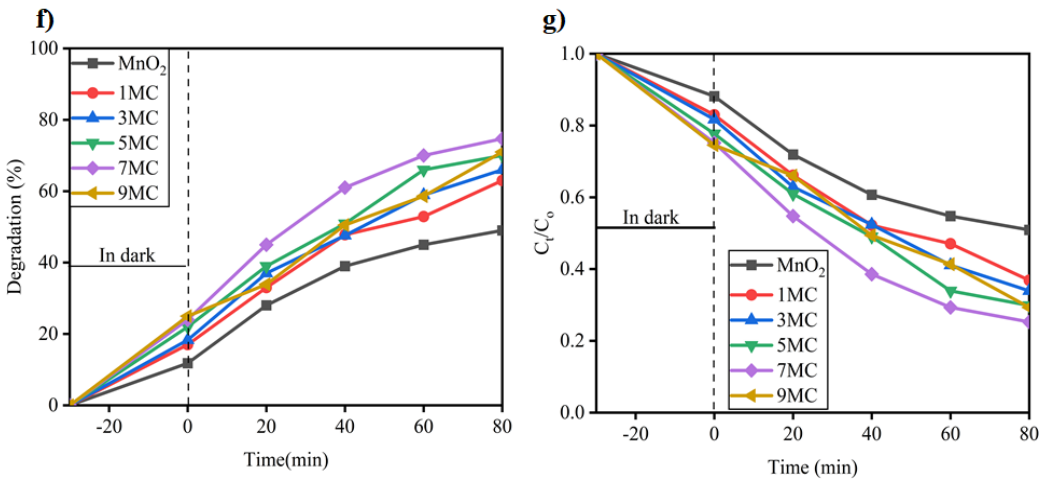

Figure 19: Photocatalytic Activity of a)1MC, b)3MC, c) 5MC, d) 7MC, e)9MC catalysts by varying MnO_2 and Cu_2O concentration, f) percentage degradation, g)C_t/C_0 of the degradation

Figure 20 (a-h) depicts the photocatalytic activity of all ternary composites 1ZMC, 2ZMC, 3ZMC, 4ZMC, and 5ZMC. All samples including MB solution without any catalyst which is named blank are compared to determine which catalyst has the highest photocatalytic activity as a result of various impacts. When the metal oxide heterojunction is bonded to the zeolite support material, the resulting composite material can exhibit improved stability, durability, surface area, band gap, reduced agglomeration, and recombination.

When MnO_2 make a junction with Cu_2O the degradation increased from 49% to 74.7 %. While this junction supported on ZeoliteX like 1-ZMC, 2-ZMC,3-ZMC,4-ZMC, and 5-ZMC degradation efficiency highly increased to 87 %, 91%, 99.01%, 97%, and 89.1 % respectively. Hence, the 3-ZMC catalyst exhibits the enhanced separation rate of electron-hole pairs; these in turn effectively degrade MB dye within 80 min under visible light which is due to a sufficient amount of ZeoliteX supported the heterojunction with good band alignment. It is seen that the ZeoliteX-supported heterojunction has a modified crystal structure, improved surface area, less agglomeration, and increased band gap, and the recombination is highly reduced, hence generating more active sites on the photocatalyst surface. The main role of the synergetic effect was proven by checking the performance of sample 3-ZMC without any light and labeled as D-ZMC. It resulted in 75% of MB removal which is far small than other ternary composites.

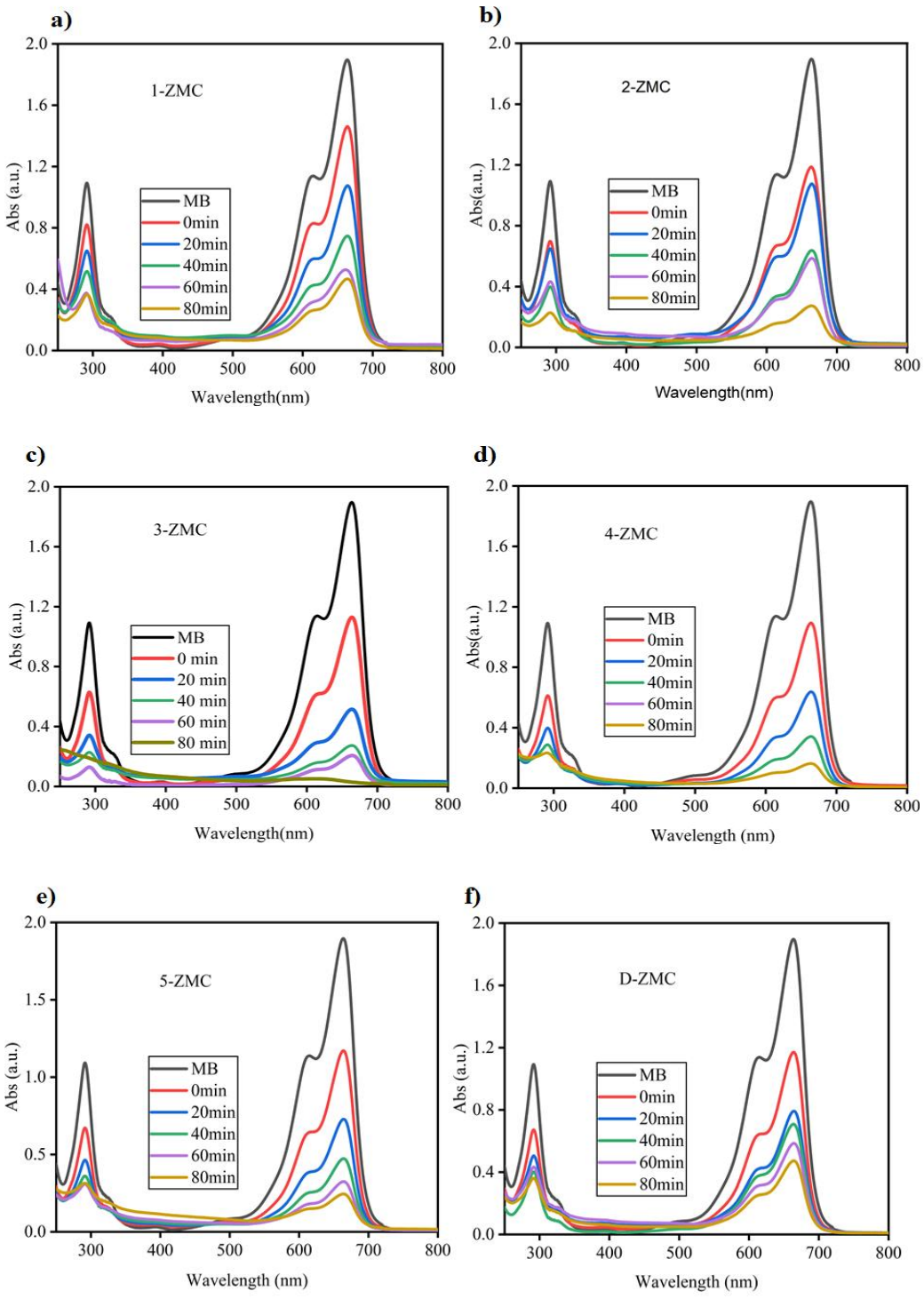
a)
1-ZMC
MB
0min
20min
40min
60min
80min
Abs (a.u.)
Wavelength(nm)
b)
2-ZMC
MB
0min
20min
40min
60min
80min
Abs(a.u.)
Wavelength(nm)
c)
3-ZMC
MB
0 min
20 min
40 min
60 min
80 min
Abs (a.u.)
Wavelength(nm)
d)
4-ZMC
MB
0min
20min
40min
60min
80min
Abs(a.u.)
Wavelength (nm)
e)
5-ZMC
MB
0min
20min
40min
60min
80min
Abs (a.u.)
Wavelength (nm)
f)
D-ZMC
MB
0min
20min
40min
60min
80min
Abs (a.u.)
Wavelength (nm)

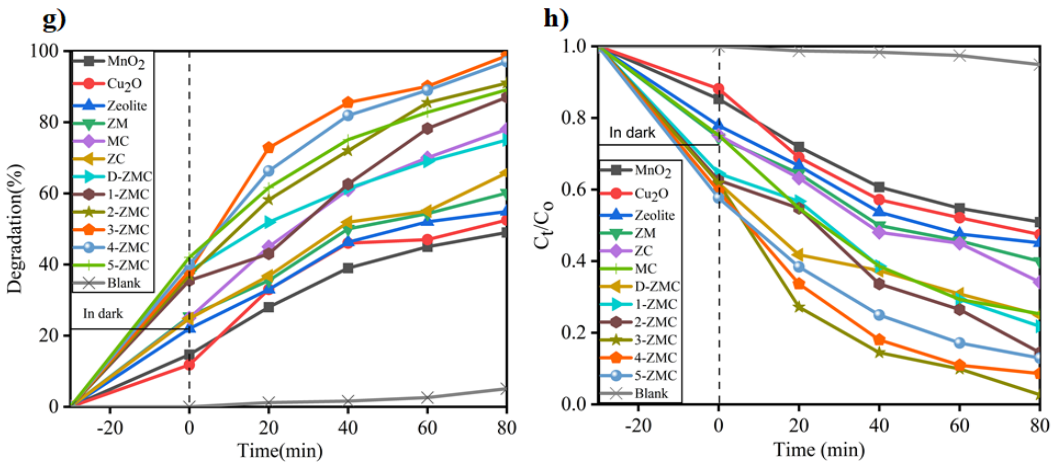

Figure 20: Photocatalytic Activity of a)1-ZMC, b)2-ZMC, c) 3-ZMC, d) 4-ZMC, e)5-ZMC catalysts by varying ZeoliteX concentration, f) percentage degradation, g) Ct ⁄C0 of the degradation.

4.9.1 Photodegradation Kinetic

Understanding the behavior and fate of pollutants and other compounds in the environment is crucial to understand the kinetics of the synergetic effect of adsorption and photodegradation (Luo et al., 2019). A rate law that takes into consideration the substance concentrations, the light intensity, and the characteristics of the surface where the substance is adsorbed can be used to characterize the kinetics of the synergistic effect of adsorption and photodegradation. Other elements that might affect the degradation process, like the presence of other compounds or the environment's temperature and humidity, can also be considered by the rate law (Natarajan et al., 2018).

The kinetics of the **s**ynergetic effect of adsorption and photodegradation were calculated by using Langmuir Hinshelwood kinetic equations:

$$lnC = -Kt + lnC_o \qquad (4)$$

While by rearranging equation (4) it gives: $ln\ Co/C = kt$ (5)

Where Co and C are the initial dye concentration (mg L^{-1}) and the dye concentration (mg L^{-1}) at time t, and k is the pseudo-first-order reaction rate constant (min^{-1}), the initial concentration (Co) and the ratio of dye concentration at time t (C) were plotted versus time (Luo et al., 2019).

The slope of the Langmuir isotherm plot was related to the Langmuir constant K and used to estimate the maximum adsorption capacity of the surface. The degradation by the pseudo-kinetic equation and the rate constants (k) of MnO_2, Cu_2O, ZeoliteX, ZM, ZC, and MC samples are shown in Figure 21 (a, b), and Table 5 shows the Percent Degradation Efficiency (PDE), kinetic rate constant (k) and correlation coefficients (R^2).

Figure 21 (c, d) shows the kinetic study of MnO_2, Cu_2O, 1MC,3MC,5MC,7MC, and 9MC degradation using pseudo-first-order kinetic plot and the rate constants (k) of those samples, and Table 6 reveals due to the optimum amount of MnO_2 and Cu_2O in the formation of heterojunction 7MC had the greatest degradation efficiency (74.7%) and degradation rate constant (17.45×10^{-3} min^{-1}). The Figure 21(e, f) shows the kinetic study of MnO_2, Cu_2O,7MC, 1-ZMC,2-ZMC,3-ZMC,4-ZMC,5-ZMC, and D-ZMC degradation using pseudo-first-order kinetic plot and the rate constants (k) of those samples, and Table 7 revels sample 3-ZMC had the greatest degradation efficiency (98.7 %) and highest degradation rate constant (44.2×10^{-3} min^{-1}) due to optimum amount of ZeoliteX support, high surface area, low agglomeration rate, a good band alignment, a lower charge carrier recombination rate, and effective separation of photo-excited electron-hole pairs (Karimi-Shamsabadi et al., 2017).

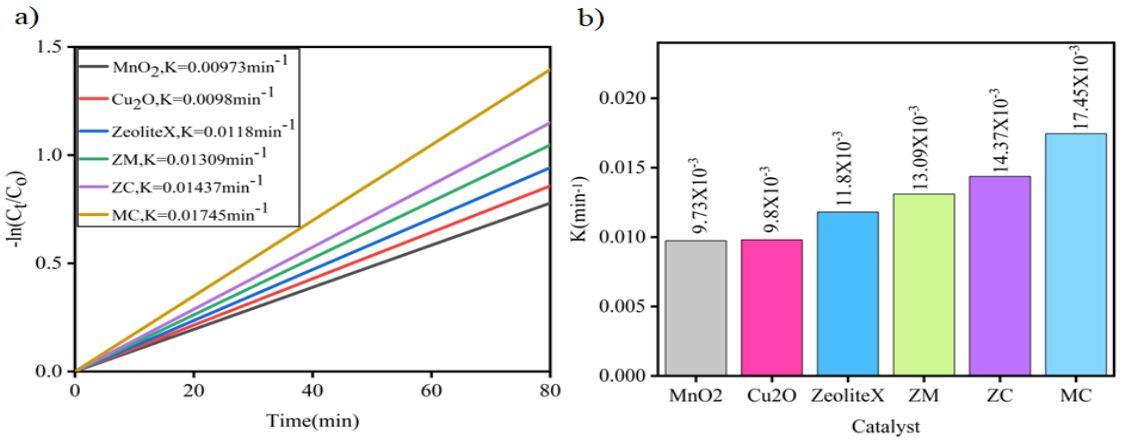

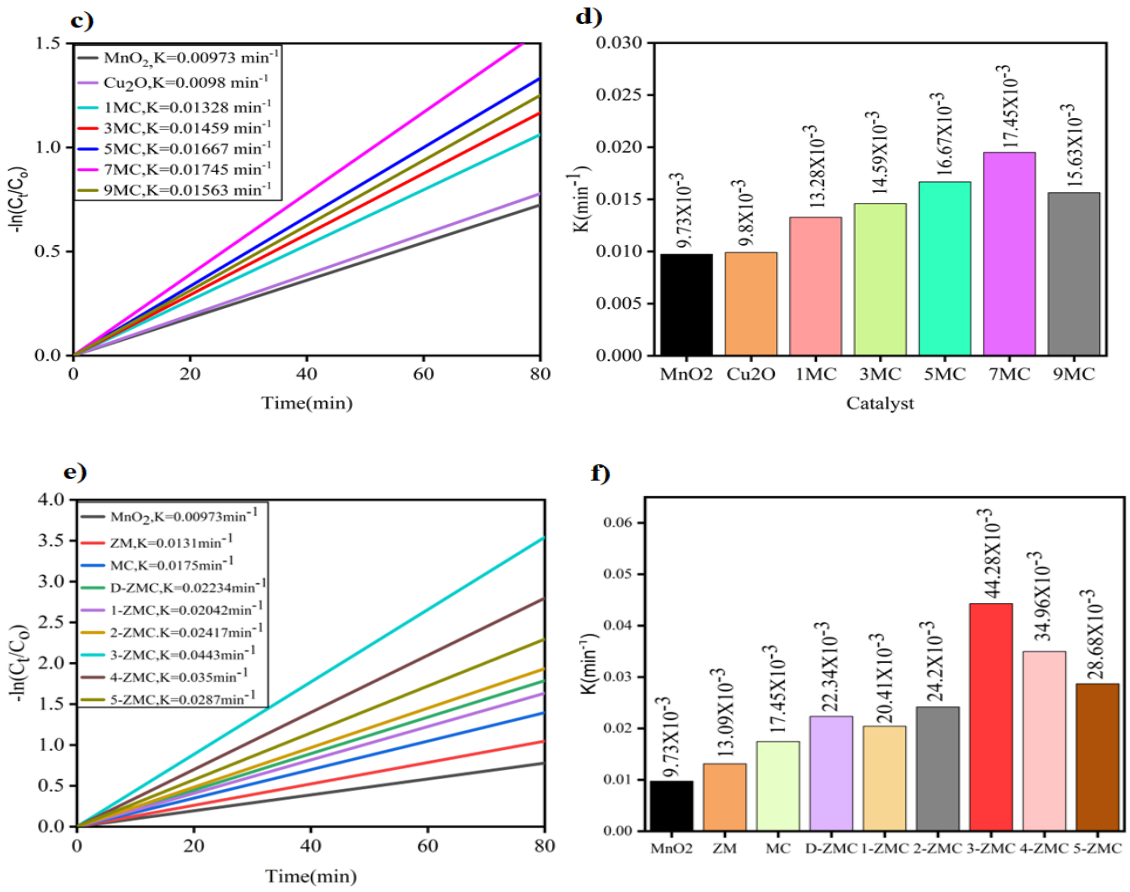

Figure 21: the kinetics study of (a) MnO_2, Cu_2O, ZeoliteX, ZC, and MC degradation on the effect of Zeolite support and heterojunction with Cu_2O (c) MnO_2, 1MC,3MC,5MC,7MC, and 9MC degradation on the effect of concentration varying MnO_2 and Cu_2O (e) MnO_2, ZM, 7MC, D-ZMC,1-ZMC,2-ZMC,3-ZMC,4-ZMC, and 5-ZMC and (b, d, f) the rate constants of those catalysts.

Table 6: The percentage degradation efficiency, kinetic rate constant, and correlation coefficients of MnO_2, Cu_2O, ZeoliteX, ZM, ZC, and MC

	MnO_2	**Cu_2O**	**ZeoliteX**	**ZM**	**ZC**	**MC**
PDE(%)	49	52	54	61	65	74.7
K(min^{-1})	9.73×10^{-3}	9.8×10^{-3}	11.8×10^{-3}	13.03×10^{-3}	14.37×10^{-3}	17.45×10^{-3}
R^2	0.94	0.952	0.924	0.926	0.945	0.97

Table 7: The percentage degradation efficiency, kinetic rate constant, and correlation coefficients of MnO_2 and heterojunction MC with varying MnO_2 and Cu_2O concentration

	MnO_2	**1MC**	**3MC**	**5MC**	**7MC**	**9MC**
PDE(%)	49	63	66	70.1	74.7	71
K(min^{-1})	9.73×10^{-3}	13.28×10^{-3}	14.59×10^{-3}	16.67×10^{-3}	17.45×10^{-3}	15.64×10^{-3}
R^2	0.94	0.97	0.98	0.989	0.97	0.99

Table 8: The percentage degradation efficiency, kinetic rate constant, and correlation coefficients of MnO_2 and ternary composite ZMC with varying Zeolite X concentration

	MnO_2	**MC**	**D-ZMC**	**1-ZMC**	**2-ZMC**	**3-ZMC**	**4-ZMC**	**5-ZMC**
PDE(%)	49	74.7	75	87	91	99.01	97	89.1
K(min^{-1})	9.73×10^{-3}	17.45×10^{-3}	22.3×10^{-3}	20.4×10^{-3}	24.17×10^{-3}	44.2×10^{-3}	34.96×10^{-3}	28.6×10^{-3}
R^2	0.94	0.97	0.96	0.952	0.963	0.97	0.95	0.95

4.9.2 Effect of Catalyst Dosage on Degradation of MB

To prevent applying excessive amounts of catalyst for efficient degradation, a series of experiments were carried out by varying the amount of the photocatalyst in the range of 0.1–0.5 g/L with an initial dye concentration of 0.1 g/L and pH 7. It was discovered that, up to a certain point, the rate of degradation increased initially with the rise in catalyst concentration since the number of photons absorbed and the quantity of dye molecules adsorbed both increases as catalyst concentration rises whereas 0.4 g/L was discovered to be the ideal catalyst concentration in the current study.

However, as the load further increased to 0.5 g/L, a reduction in photodegradation efficiency was observed which could relate to particle aggregation and decreased the number of active sites. Additionally, when the load is higher than what is optimal, the solution becomes darker and a light screening effect takes place, which lowers the surface area of the nano-composite exposed to light illumination, consequently, the photocatalytic efficiency (Kumar, Rashid, & Barakat, 2015).

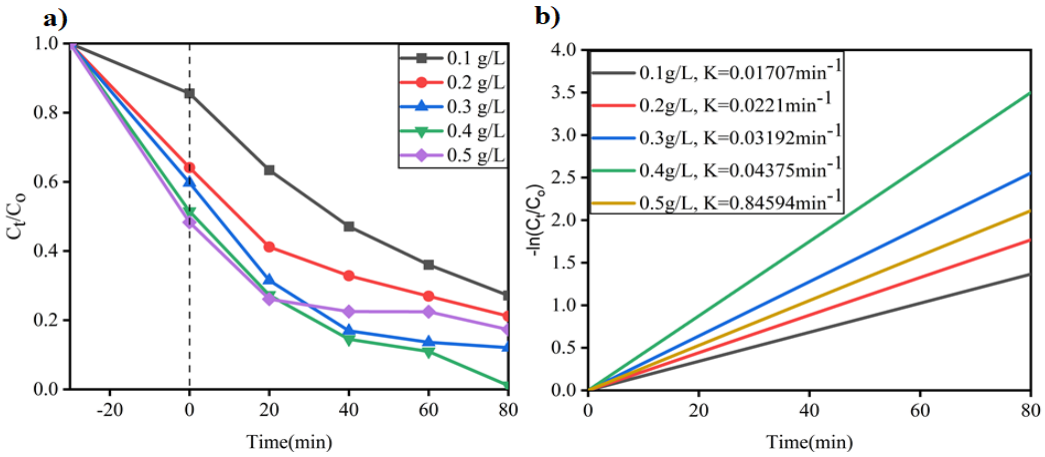

Figure 22: Effect of 3-ZMC Catalytic dosage on the degradation of Methylene blue at pH 7

4.9.3. Effect of pH

One of the most critical elements influencing the net charge on the surface of photocatalysts and organic contaminants is pH. The 3ZMC catalyst test on the MB degradation experiment was run in a basic medium with pH of 9 and 11, neutral media with pH of 7, and acidic media with pH of 3 and 5. The photocatalytic degrading effectiveness of the catalyst gradually shifts from acidic to basic when the pH of the MB dye solution rises, as seen in Figure 23. Since MB is a positively charged molecule thus at basic solution interatomic attraction force between the catalyst surface and dye favors the adsorption (Karimi-Shamsabadi et al., 2017). In the acidic pH, the surface of the 3ZMC catalyst acquires a positive charge thereby little columbic repulsive force between the catalyst and the dye molecules, which decreased the catalyst's capacity for adsorption (Tedla et al., 2015).

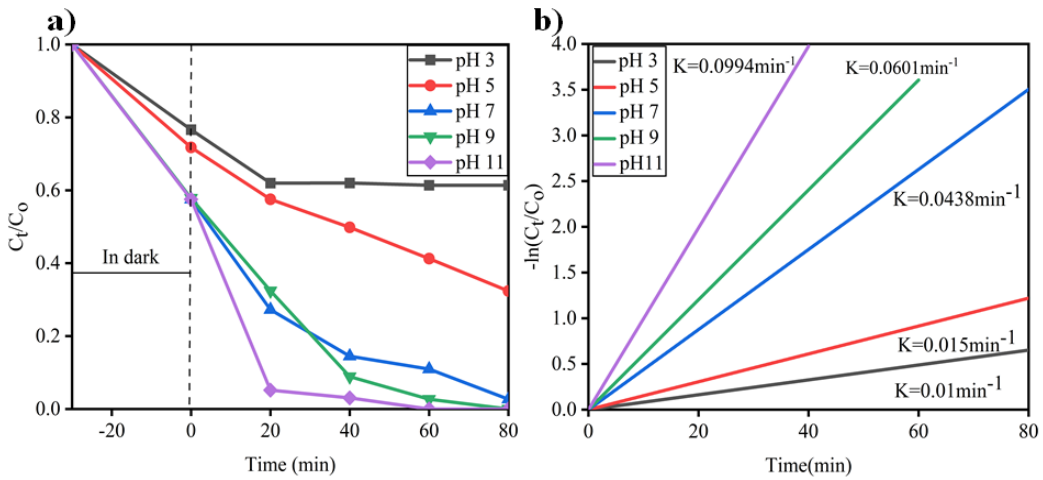

Figure 23: Effect of pH on degradation of Methylene blue at fixed 0.04 mg of 3-ZMC catalyst and 10 ppm of MB solution.

4.9.4. Effect of the initial MB concentration

By varying the initial dye concentration (0.1-0.5 g/L) in the presence of the ideal amount of 3ZMC catalyst at pH 7, the impact of dye concentration on the degradation rate of MB dye was examined. The findings demonstrated that when initial dye concentrations increased, the degradation rate reduced and the concentration of unabsorbed dye in the solution increased.

This is due to less light penetrating the solution and reaching the surface of the catalyst, which in turn reduced the concentration of OH radicals and slowed the rate of degradation. Also, the number of dye molecules competing for a fixed number of active sites on the catalyst surface increases, which results in a steric hindrance effect, thereby reducing the adsorption of dyes on the catalyst surface (Nuengmatcha, Chanthai, Mahachai, & Oh, 2016). As shown in Figure 24 the 0.1 g/L dye concentration was found to be ideal.

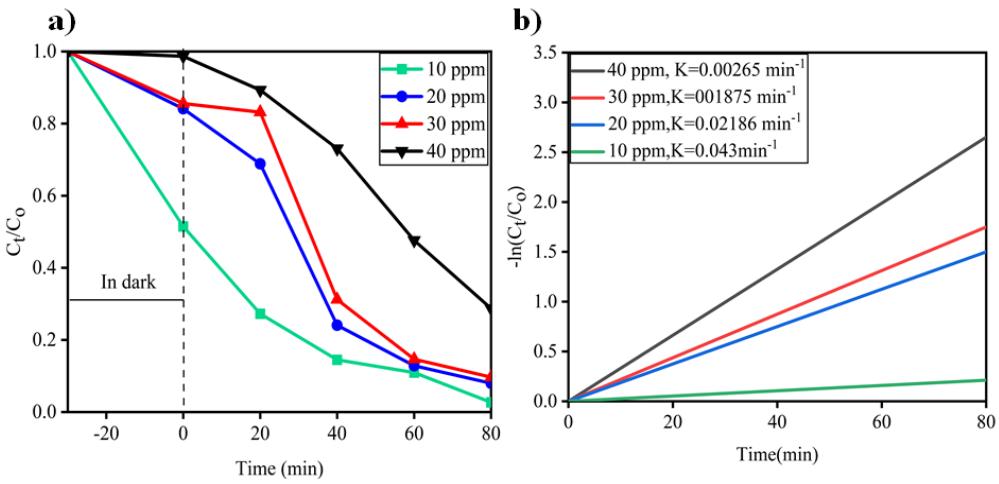

Figure 24: Effect of initial Methylene blue concentration as a function of time, using 3-ZMC catalyst at a load of 0.04 mg and pH 7 solution

4.9.5. Reusability of Catalyst

From both an economic and environmental point of view for large-scale industrial application testing the photocatalysts' durability and recyclability are essential (Xing et al., 2018). To study the stability of the degradations of methylene blue, the 3-ZMC composite catalyst was chosen. The reusability results revealed a little decrease in photocatalytic degradation efficiency in each cycle. As shown in Figure 25(a), the photocatalytic degradation efficiency of the 3-ZMC composite decreased from 99.01 % to 93.4 % after five cycles. These results suggest that the manufactured 3-ZMC catalyst for photodegradation is highly stable and reusable.

Additionally, the XRD pattern for the recycled photocatalyst demonstrated stability which does not change in phase or crystallinity until utilized for five cycles, and only a small reduction in intensity was observed after reuse (Figure 25(b)).

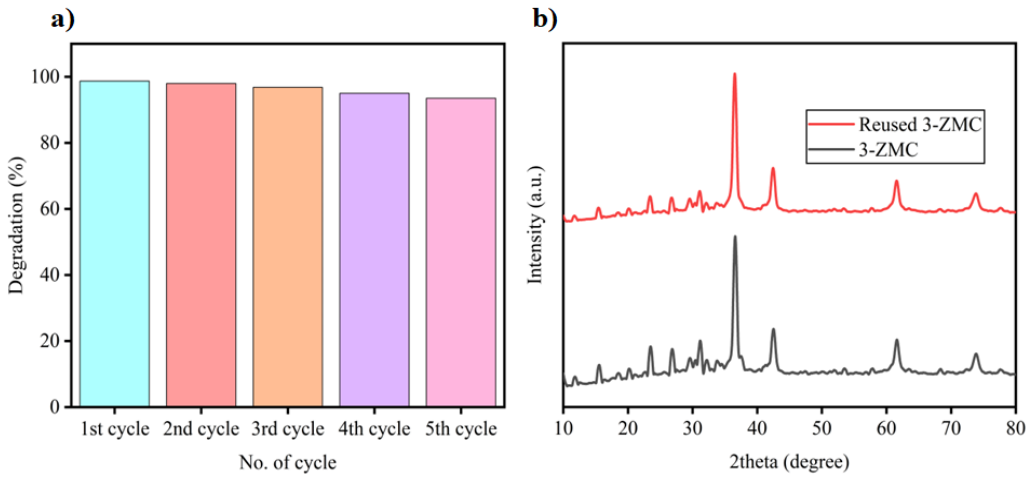

Figure 25: (a) Reusability test 3-ZMC catalyst for photocatalytic degradation of Methylene blue under Visible light irradiation (b), XRD pattern obtained for the recycled 3-ZMC catalyst

4.9.7 Mechanism of Photodegradation

To distinguish between p and n-type metal oxides, Mott-Schottky analysis, which measures the capacitance of a semiconductor-electrolyte interface as a function of the applied voltage, was used (Figure 26 a and b). MnO_2 behaves as an n-type semiconductor due to the positive slope of its Mott–Schottky plots and Cu_2O behaves as a p-type semiconductor due to the negative slope of its Mott–Schottky plot. The flat-band potential (V_{FB}) was analyzed by extending the plot's linear part to the x-axis and resulted in -0.945 V and 1.12 V vs. Ag/AgCl electrodes for MnO_2 and Cu_2O respectively. Regarding a normal hydrogen electrode (NHE), the flat band potential of the two semiconductors is correspondingly obtained as, -0.384 V and 1.681 V vs. NHE (Nakabayashi, Nishikawa, & Nosaka, 2014). The effective SCs VB and CB edge potential for MnO_2 to be 0.825 and 2.555 eV, and for Cu_2O to be -0.395 and 2.035 eV, respectively (Pradhan, Rath, Sethi, Nanda, & Nanda, 2021; Rajendran et al., 2021).

Based on this result, Figure 26 (c) was proposed to illustrate a possible charge separation in the heterojunction and working mechanism with the support of ZeoliteX for the degradation of MB. When the composite is irradiated by simulated sunlight the electrons on MnO_2 and Cu_2O are transferred from VB to CB.

When p-type Cu_2O and n-type MnO_2 are combined, many p-n junctions are created so the holes in the valence band (VB) of the p-type Cu_2O will mix with the electrons in the conduction band (CB) of the n-type MnO_2. As a result of this p-n junction structure, photoexcited electron-hole pairs are efficiently segregated, whereas the direct Z-scheme electron transfer process could occur between the semiconductors (Ye et al., 2015). The n-type and P-type collaboration is supportive of this transfer process since charge flow from high to low concentration (Ye et al., 2015). This reaction process is thermodynamically feasible due to the sufficiently negative CB potential of Cu_2O (-0.395eV vs NHE) compared to E_O ($O^{\bullet}/O_2$) = -0.33 eV vs NHE. Furthermore, the VB potential of MnO_2 (2.555 eV) is higher than that of $H_2O/OH\bullet$ (2.32 eV). As a result, they can convert oxygen to oxide radicals and water molecules into hydroxyl radicals respectively (Jin, Kang, et al., 2020). Even though those generated radicals have a short lifetime of about a few nanoseconds the ZeoliteX brings MB molecules near the catalyst surface due to its high adsorption capacity and hence they immediately react with those radicals (Derikvandi & Nezamzadeh-Ejhieh, 2017b). So, the synergetic mechanism from heterojunction photocatalyst and adsorption from ZeoliteX support could result in efficient degradation performance.

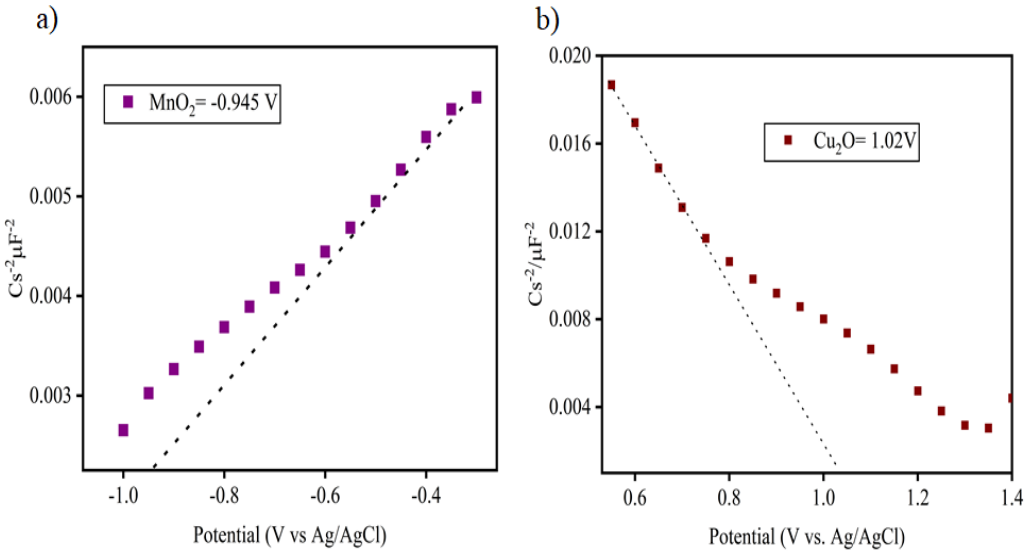

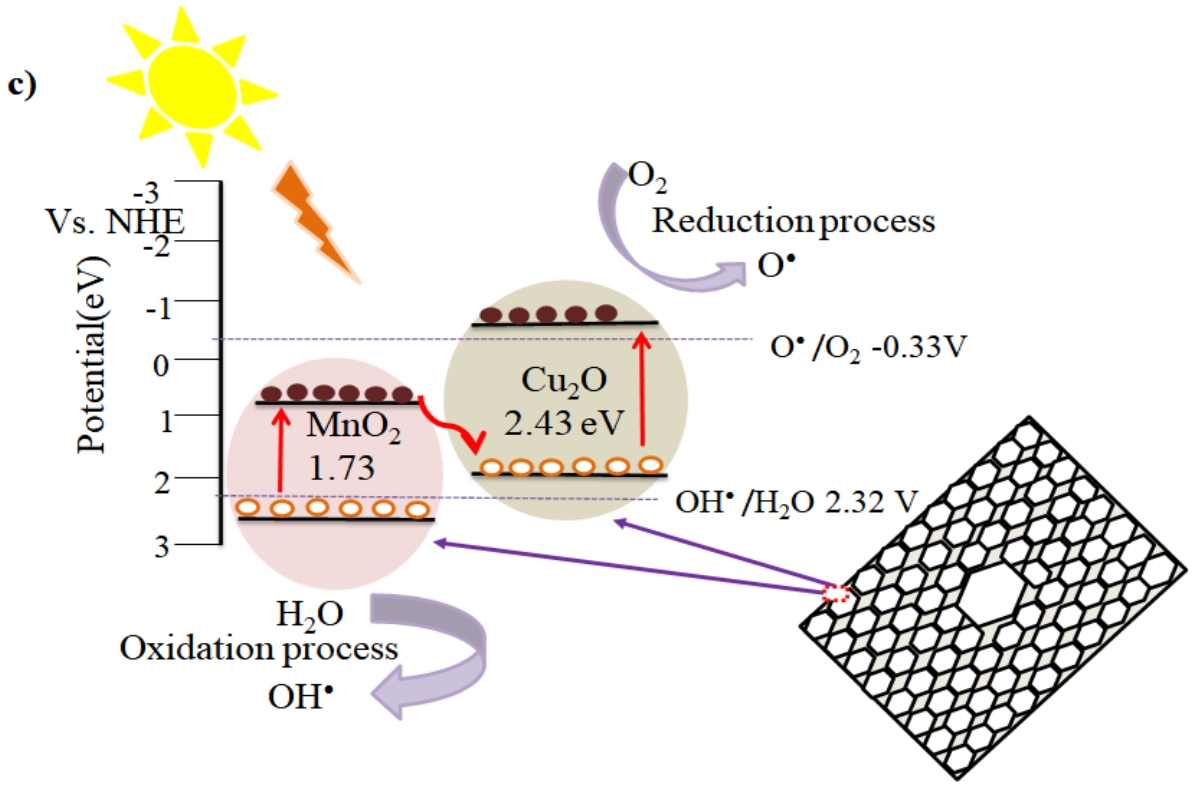

Figure 26: Mott–Schottky plots of (a) MnO_2 and (b) Cu_2O and (C) Zeolite X supported MnO_2 with Cu_2O heterojunction composite against MB

5. CONCLUSION AND RECOMMENDATIONS

5.1 Conclusion

The MnO_2 with Cu_2O heterojunction supported on ZeoliteX was synthesized by the wet impregnation method. The direct Z-scheme p-n heterojunction was prepared to reduce the recombination rate and enhance the redox reaction. By varying their concentration which was assigned as 1MC,2MC,5MC,7MC, and 9MC performance had been compared and 7MC (70%MnO_2 with 30% Cu_2O) get a better degradation performance of MB compared to other heterojunctions. The ZeoliteX was synthesized by an easy alkali fusion method from raw kaolin clay. Then the synthesized ZeoliteX supported the heterojunction 7MC by different amounts starting from 10 to 50% which were labeled as 1-ZMC, 2-ZMC, 3-ZMC, 4-ZMC, and 5-ZMC to study the effect on reduction of agglomeration, stability and the impact of provided active site on the degradation of MB. The phase, morphology, and optical behavior of the synthesized samples are confirmed through various characterization techniques. All catalysts had a small band gap which is in the visible range of the solar spectrum. It was found that the recombination rate reduces due to heterojunction formation and the support ZeoliteX enhances thermal stability, provides an active site for catalytic activity, and reduces agglomeration rate. Also, it has an impact on reducing the recombination rate. Among all catalysts, 3-ZMC exhibits the highest degradation activity (99.01%) due to a sufficient amount of ZeoliteX supported by the heterojunction 7MC which results in low recombination, lower electron transfer resistance, small agglomeration, and high surface area. The highest photocatalytic activity at pH11 indicates the interatomic attraction force between the negatively charged 3-ZMC catalyst and the positively charged MB which is to be adsorbed to the surface of the catalyst. The increase in photodegradation efficiency at 0.4 g/L could be attributed to the availability of more active sites and the easiness of penetration of light. The reusability of the prepared catalyst up to 5 cycles indicates the catalyst was stable and efficient.

5.2 Recommendations

1. The impact of additional factors like reaction temperature and speed should be investigated while studying the degradation of various organic and inorganic contaminants.

2. Investigating the Catalyst's stability under various circumstances, such as high temperatures or exposure to various gases, can assist in determining its suitability for practical application.

3. Synthesizing method for a ternary composite of the support and heterojunction need further studies which could affect performance and stability.

4. It can be used for a variety of purposes, including water splitting, antibacterial and antifungal coatings, drug delivery, and solar cells.

5. Finally, it will be crucial to scale up production and market this material to realize its full potential so analysis of the economic viability of large-scale production could be the main areas of future study.

Reference

Achar, T. K., Bose, A., & Mal, P. (2017). Mechanochemical synthesis of small organic molecules. *Beilstein journal of organic chemistry, 13*(1), 1907-1931.

Acharya, L., Nayak, S., Pattnaik, S. P., Acharya, R., & Parida, K. (2020). Resurrection of boron nitride in pn type-II boron nitride/B-doped-g-C3N4 nanocomposite during solid-state Z-scheme charge transfer path for the degradation of tetracycline hydrochloride. *Journal of colloid and interface science, 566*, 211-223.

Aguirre, M. E., Zhou, R., Eugene, A. J., Guzman, M. I., & Grela, M. A. (2017). Cu2O/TiO2 heterostructures for CO2 reduction through a direct Z-scheme: Protecting Cu2O from photocorrosion. *Applied Catalysis B: Environmental, 217*, 485-493.

Ahuja, P., Ujjain, S. K., Kanojia, R., & Attri, P. (2021). Transition metal oxides and their composites for photocatalytic dye degradation. *Journal of Composites Science, 5*(3), 82.

Ajmal, A., Majeed, I., Malik, R., Iqbal, M., Nadeem, M. A., Hussain, I., . . . Nadeem, M. A. (2016). Photocatalytic degradation of textile dyes on Cu2O-CuO/TiO2 anatase powders. *Journal of environmental chemical engineering, 4*(2), 2138-2146.

Al-Khalid, T., & El-Naas, M. H. (2012). Aerobic biodegradation of phenols: a comprehensive review. *Critical reviews in environmental science and technology, 42*(16), 1631-1690.

Ali, G. A., Yusoff, M. M., Algarni, H., & Chong, K. F. (2018). One-step electrosynthesis of MnO2/rGO nanocomposite and its enhanced electrochemical performance. *Ceramics International, 44*(7), 7799-7807.

Ali, M. M., & Williams, D. J. (2023). Synergistic effect of PCz/SnO2/MnO2 heterojunction nanocomposites for boosted photocatalytic performance induced by interfacial charge transfer. *Materials Chemistry and Physics, 293*, 126973.

Alzahrani, S. A., Al-Thabaiti, S. A., Al-Arjan, W. S., Malik, M. A., & Khan, Z. (2017). Preparation of ultra long α-MnO2 and Ag@ MnO2 nanoparticles by seedless approach and their photocatalytic performance. *Journal of Molecular Structure, 1137*, 495-505.

Ameta, S., & Ameta, R. (2018). *Advanced oxidation processes for wastewater treatment: emerging green chemical technology*: Academic press.

Antonopoulou, M., Kosma, C., Albanis, T., & Konstantinou, I. (2021). An overview of homogeneous and heterogeneous photocatalysis applications for the removal of pharmaceutical compounds from real or synthetic hospital wastewaters under lab or pilot scale. *Science of The Total Environment, 765*, 144163.

Ashraf, A., Liu, G., Yousaf, B., Arif, M., Ahmed, R., Irshad, S., . . . Gulzaman, H. (2021). Recent trends in advanced oxidation process-based degradation of erythromycin: Pollution status, eco-toxicity and degradation mechanism in aquatic ecosystems. *Science of The Total Environment, 772*, 145389.

Atalay, S., & Ersöz, G. (2015). Advanced oxidation processes for removal of dyes from aqueous media. *Green Chemistry for Dyes Removal from Wastewater: Research Trends and Applications*, 83-117.

Atalay, S., & Ersöz, G. (2021). Hybrid application of advanced oxidation processes to dyes′ removal. In *Green Chemistry and Water Remediation: Research and Applications* (pp. 209-238): Elsevier.

Awuchi, C. G., Hannington, T., Awuchi, C. G., Igwe, V. S., & Amagwula, I. O. (2020). Industrial waste management, treatment, and health issues: wastewater, solid, and electronic wastes. *European Academic Research, 8*(2), 1081-1119.

Ayele, L., Pérez-Pariente, J., Chebude, Y., & Díaz, I. (2016). Conventional versus alkali fusion synthesis of zeolite A from low grade kaolin. *Applied Clay Science, 132*, 485-490.

Baral, A., Satish, L., Zhang, G., Ju, S., & Ghosh, M. K. (2021). A review of recent progress on nano MnO 2: synthesis, surface modification and applications. *Journal of Inorganic and Organometallic Polymers and Materials, 31*, 899-922.

Birgisson, S., Saha, D., & Iversen, B. B. (2018). Formation mechanisms of nanocrystalline MnO2 polymorphs under hydrothermal conditions. *Crystal Growth & Design, 18*(2), 827-838.

Bora, T., & Dutta, J. (2014). Applications of nanotechnology in wastewater treatment—a review. *Journal of Nanoscience and Nanotechnology, 14*(1), 613-626.

Cao, M., Zhuang, Z., Liu, Y., Zhang, Z., Xuan, J., Zhang, Q., & Wang, W. (2022). Peptide-mediated green synthesis of the MnO2@ ZIF-8 core–shell nanoparticles for efficient removal of pollutant dyes from wastewater via a synergistic process. *Journal of colloid and interface science, 608*, 2779-2790.

Caponi, N., Collazzo, G. C., Jahn, S. L., Dotto, G. L., Mazutti, M. A., & Foletto, E. L. (2017). Use of Brazilian kaolin as a potential low-cost adsorbent for the removal of malachite green from colored effluents. *Materials Research, 20*, 14-22.

Cavalcante, R. P., Dantas, R. F., Bayarri, B., González, O., Giménez, J., Esplugas, S., & Junior, A. M. (2016). Photocatalytic mechanism of metoprolol oxidation by photocatalysts TiO2 and TiO2 doped with 5% B: Primary active species and intermediates. *Applied Catalysis B: Environmental, 194*, 111-122.

Cech, T. V. (2018). *Principles of water resources: history, development, management, and policy*: John Wiley & Sons.

Chan, S. H. S., Yeong Wu, T., Juan, J. C., & Teh, C. Y. (2011). Recent developments of metal oxide semiconductors as photocatalysts in advanced oxidation processes (AOPs) for treatment of dye waste-water. *Journal of Chemical Technology & Biotechnology, 86*(9), 1130-1158.

Chan, Y.-L., Pung, S.-Y., Sreekantan, S., & Yeoh, F.-Y. (2016). Photocatalytic activity of β-MnO2 nanotubes grown on PET fibre under visible light irradiation. *Journal of Experimental Nanoscience, 11*(8), 603-618.

Chand, P., Joshi, A., Lal, S., & Singh, V. (2021). Effect of hydrothermal temperature on structural, optical and electrochemical properties of α-MnO2 nanostructures for supercapacitor application. *Chemical Physics Letters, 777*, 138742.

Chang, Li, S., Wang, Z., Yu, J., Huang, H., & Qiu, J. (2019). Strategies and insights towards the intrinsic capacitive properties of MnO2 for supercapacitors: challenges and perspectives. *Nano Energy, 57*, 459-472.

Chen, C., Xu, H., Xu, L., Zhang, F., Dong, J., & Wang, H. (2013). One-pot synthesis of homogeneous core–shell Cu 2 O films with nanoparticle-composed multishells and their photocatalytic properties. *RSC advances, 3*(47), 25010-25018.

Chen, J., Huang, Z., Meng, H., Zhang, L., Ji, D., Liu, J., . . . Li, Z. (2018). A facile fluorescence lateral flow biosensor for glutathione detection based on quantum dots-MnO2 nanocomposites. *Sensors and Actuators B: Chemical, 260*, 770-777.

Chen, S., Zhu, J., Han, Q., Zheng, Z., Yang, Y., & Wang, X. (2009). Shape-controlled synthesis of one-dimensional MnO2 via a facile quick-precipitation procedure and its electrochemical properties. *Crystal Growth & Design, 9*(10), 4356-4361.

Chen, X., Sun, H., Zhang, J., Zelekew, O. A., Lu, D., Kuo, D.-H., & Lin, J. (2019). Synthesis of visible light responsive iodine-doped mesoporous TiO2 by using biological renewable lignin as template for degradation of toxic organic pollutants. *Applied Catalysis B: Environmental, 252*, 152-163.

Chen, X., Wu, Z., Liu, D., & Gao, Z. (2017). Preparation of ZnO photocatalyst for the efficient and rapid photocatalytic degradation of azo dyes. *Nanoscale research letters, 12*, 1-10.

Chen, X., Zhao, C., Wu, H., Shi, Y., Chen, C., & Zhou, X. (2022). Two-Dimensional ZnS/SnS2 Heterojunction as a Direct Z-Scheme Photocatalyst for Overall Water Splitting: A DFT Study. *Materials, 15*(11), 3786.

Chen, Y. C., Chen, Y. J., Popescu, R., Dong, P. H., Gerthsen, D., & Hsu, Y. K. (2019). Defect-Cluster-Boosted Solar Photoelectrochemical Water Splitting by n-Cu2O Thin Films Prepared Through Anisotropic Crystal Growth. *ChemSusChem, 12*(21), 4859-4865.

Chiam, S.-L., Pung, S.-Y., & Yeoh, F.-Y. (2020). Recent developments in MnO2-based photocatalysts for organic dye removal: a review. *Environmental Science and Pollution Research, 27*(6), 5759-5778.

Crini, G., & Lichtfouse, E. (2019). Advantages and disadvantages of techniques used for wastewater treatment. *Environmental Chemistry Letters, 17*(1), 145-155.

Danish, M. S. S., Estrella, L. L., Alemaida, I. M. A., Lisin, A., Moiseev, N., Ahmadi, M., . . . Senjyu, T. (2021). Photocatalytic applications of metal oxides for sustainable environmental remediation. *Metals, 11*(1), 80.

David, A., & Vedhi, C. (2022). Synthesis, Characterization and Photocatalytic Activities of Co3O4-MnO2-ZnO Ternary Nanoparticles. *ECS Transactions, 107*(1), 2003.

David, S. A., & Vedhi, C. (2017). Synthesis of nano Co3O4-MnO2-ZrO2 mixed oxides for visible-light photocatalytic activity. *International journal of advance research in science and engineering, 6*(01), 613-623.

Dawadi, S., Gupta, A., Khatri, M., Budhathoki, B., Lamichhane, G., & Parajuli, N. (2020). Manganese dioxide nanoparticles: synthesis, application and challenges. *Bulletin of Materials Science, 43*, 1-10.

De Gisi, S., Lofrano, G., Grassi, M., & Notarnicola, M. (2016). Characteristics and adsorption capacities of low-cost sorbents for wastewater treatment: a review. *Sustainable Materials and Technologies, 9*, 10-40.

Deng, Y., & Zhao, R. (2015). Advanced oxidation processes (AOPs) in wastewater treatment. *Current Pollution Reports, 1*(3), 167-176.

Derikvandi, H., & Nezamzadeh-Ejhieh, A. (2017a). Increased photocatalytic activity of NiO and ZnO in photodegradation of a model drug aqueous solution: effect of coupling, supporting, particles size and calcination temperature. *Journal of hazardous materials, 321*, 629-638.

Derikvandi, H., & Nezamzadeh-Ejhieh, A. (2017b). Synergistic effect of pn heterojunction, supporting and zeolite nanoparticles in enhanced photocatalytic activity of NiO and SnO2. *Journal of colloid and interface science, 490*, 314-327.

Diallo, A., Kaviyarasu, K., Ndiaye, S., Mothudi, B., Ishaq, A., Rajendran, V., & Maaza, M. (2018). Structural, optical and photocatalytic applications of biosynthesized NiO nanocrystals. *Green Chemistry Letters and Reviews, 11*(2), 166-175.

Dinh, V.-P., Luu, A. T., Krzysztof, S., Kozlenko, D., Khiem, L., Dang, N. T., . . . Lo, T. S. (2020). Crystallization pathways, morphologies and structural defects of α-MnO2 nanomaterial synthesized under annealed temperatures.

Dong, L., Li, Y., Chen, D., Chen, X., & Zhang, D. (2020). Facilitated activation of peroxymonosulfate by loading ZIF-8 on Fe3O4-MnO2 for deep mineralization of bisphenol A. *ACS ES&T Water, 1*(2), 417-429.

Du, C., Zhang, Z., Tan, S., Yu, G., Chen, H., Zhou, L., . . . Deng, F. (2021). Construction of Z-scheme g-C3N4/MnO2/GO ternary photocatalyst with enhanced photodegradation ability of tetracycline hydrochloride under visible light radiation. *Environmental research, 200*, 111427.

Dubey, M., Challagulla, N. V., Wadhwa, S., & Kumar, R. (2021). Ultrasound assisted synthesis of magnetic Fe3O4/α-MnO2 nanocomposite for photodegradation of organic dye. *Colloids and Surfaces A: Physicochemical and Engineering Aspects, 609*, 125720.

Durai, S. V., Prasad, L. G., Kumar, E., Muthuraj, D., & Jothy, V. B. (2018). Investigation on Structural and Optical Properties of Manganese dioxide nanoparticles by Microwave Assisted Solution Method. *International Journal of Rearch in Advent Technology, 6*, 1531-1535.

Dutta, S., Gupta, B., Srivastava, S. K., & Gupta, A. K. (2021). Recent advances on the removal of dyes from wastewater using various adsorbents: A critical review. *Materials Advances*.

Erwin, S. C., Zu, L., Haftel, M. I., Efros, A. L., Kennedy, T. A., & Norris, D. J. (2005). Doping semiconductor nanocrystals. *Nature, 436*(7047), 91-94.

Foroutan, R., Peighambardoust, S. J., Boffito, D. C., & Ramavandi, B. (2022). Sono-Photocatalytic activity of cloisite 30B/ZnO/Ag2O nanocomposite for the simultaneous degradation of crystal violet and methylene blue dyes in aqueous media. *Nanomaterials, 12*(18), 3103.

Franger, S., Bach, S., Farcy, J., Pereira-Ramos, J.-P., & Baffier, N. (2002). Synthesis, structural and electrochemical characterizations of the sol–gel birnessite MnO1. 84· 0.6 H2O. *Journal of power sources, 109*(2), 262-275.

Fu, F., Cheng, Z., & Lu, J. (2015). Synthesis and use of bimetals and bimetal oxides in contaminants removal from water: a review. *RSC advances, 5*(104), 85395-85409.

Ghosh, S. K. (2020). Diversity in the family of manganese oxides at the nanoscale: from fundamentals to applications. *ACS omega, 5*(40), 25493-25504.

Guo, Y., Li, L., Song, L., Wu, M., Gao, Y., Chen, J., . . . Niu, H. (2019). Co 2+ induced phase transformation from δ-to α-MnO 2 and their hierarchical α-MnO 2@ δ-MnO 2 nanostructures for efficient asymmetric supercapacitors. *Journal of Materials Chemistry A, 7*(20), 12661-12668.

Gürses, A., Açıkyıldız, M., Güneş, K., Gürses, M. S., Gürses, A., Açıkyıldız, M., . . . Gürses, M. S. (2016). Dyes and pigments: their structure and properties. *Dyes and pigments*, 13-29.

Han, R., Wang, Y., Sun, Q., Wang, L., Song, J., He, X., & Dou, C. (2010). Malachite green adsorption onto natural zeolite and reuse by microwave irradiation. *Journal of hazardous materials, 175*(1-3), 1056-1061.

Hariganesh, S., Vadivel, S., Maruthamani, D., & Rangabhashiyam, S. (2020). Disinfection by-products in drinking water: Detection and treatment methods. In *Disinfection By-products in Drinking Water* (pp. 279-304): Elsevier.

Hasan, M. K., Shahriar, A., & Jim, K. U. (2019). Water pollution in Bangladesh and its impact on public health. *Heliyon, 5*(8), e02145.

Hatakeyama, T., Okamoto, N. L., & Ichitsubo, T. (2022). Thermal stability of MnO2 polymorphs. *Journal of Solid State Chemistry, 305*, 122683.

He, Y., Jiang, D. B., Chen, J., & Zhang, Y. X. (2018). Synthesis of MnO2 nanosheets on montmorillonite for oxidative degradation and adsorption of methylene blue. *Journal of colloid and interface science, 510*, 207-220.

He, Y., Kang, Z., Li, J., Li, Y., & Tian, X. (2023). Recent progress of manganese dioxide based electrocatalysts for oxygen evolution reaction. *Industrial Chemistry & Materials*.

Hong, D., Cao, G., Qu, J., Deng, Y., & Tang, J. (2018). Antibacterial activity of Cu2O and Ag co-modified rice grains-like ZnO nanocomposites. *Journal of Materials Science & Technology, 34*(12), 2359-2367.

Hong, X., Li, Y., Wang, X., Long, J., & Liang, B. (2022). Carbon nanosheet/MnO2/BiOCl ternary composite for degradation of organic pollutants. *Journal of alloys and compounds, 891*, 162090.

Hoseinpour, V., & Ghaemi, N. (2018). Novel ZnO–MnO2–Cu2O triple nanocomposite: Facial synthesis, characterization, antibacterial activity and visible light photocatalytic performance for dyes degradation-A comparative study. *Materials Research Express, 5*(8), 085012.

Hoseinpour, V., Souri, M., & Ghaemi, N. (2018). Green synthesis, characterisation, and photocatalytic activity of manganese dioxide nanoparticles. *Micro & Nano Letters, 13*(11), 1560-1563.

Hu, G., Yang, J., Duan, X., Farnood, R., Yang, C., Yang, J., . . . Liu, Q. (2021). Recent developments and challenges in zeolite-based composite photocatalysts for environmental applications. *Chemical Engineering Journal, 417*, 129209.

Hu, T., Gao, W., Liu, X., Zhang, Y., & Meng, C. (2017). Synthesis of zeolites Na-A and Na-X from tablet compressed and calcinated coal fly ash. *Royal Society Open Science, 4*(10), 170921.

Hu, X., Kitchaev, D. A., Wu, L., Zhang, B., Meng, Q., Poyraz, A. S., . . . Ceder, G. (2018). Revealing and rationalizing the rich polytypism of todorokite MnO2. *Journal of the American Chemical Society, 140*(22), 6961-6968.

Hube, S., Eskafi, M., Hrafnkelsdóttir, K. F., Bjarnadóttir, B., Bjarnadóttir, M. Á., Axelsdóttir, S., & Wu, B. (2020). Direct membrane filtration for wastewater treatment and resource recovery: A review. *Science of The Total Environment, 710*, 136375.

Hullavarad, N., Hullavarad, S., & Karulkar, P. (2008). Cadmium sulphide (CdS) nanotechnology: synthesis and applications. *Journal of Nanoscience and Nanotechnology, 8*(7), 3272-3299.

Ikram, M., Rashid, M., Haider, A., Naz, S., Haider, J., Raza, A., . . . Ahmed, S. S. (2021). A review of photocatalytic characterization, and environmental cleaning, of metal oxide nanostructured materials. *Sustainable Materials and Technologies, 30*, e00343.

Ismail, A. A., Faisal, M., & Al-Haddad, A. (2018). Mesoporous WO3-graphene photocatalyst for photocatalytic degradation of Methylene Blue dye under visible light illumination. *Journal of Environmental Sciences, 66*, 328-337.

Iyengar, P., Das, C., & Balasubramaniam, K. (2017). Photoelectrochemical performance of NiO-coated ZnO–CdS core-shell photoanode. *Journal of Physics D: Applied Physics, 50*(10), 10LT01.

Jabbar, K. Q., Barzinjy, A. A., & Hamad, S. M. (2022). Iron oxide nanoparticles: Preparation methods, functions, adsorption and coagulation/flocculation in wastewater treatment. *Environmental Nanotechnology, Monitoring & Management, 17*, 100661.

Jackson, R. B., Carpenter, S. R., Dahm, C. N., McKnight, D. M., Naiman, R. J., Postel, S. L., & Running, S. W. (2001). Water in a changing world. *Ecological applications, 11*(4), 1027-1045.

Jamil, T. S., Ghafar, H. H. A., Ibrahim, H. S., & Abd El-Maksoud, I. H. (2011). Removal of methylene blue by two zeolites prepared from naturally occurring Egyptian kaolin as cost effective technique. *Solid State Sciences, 13*(10), 1844-1851.

Jin, C., Kang, J., Li, Z., Wang, M., Wu, Z., & Xie, Y. (2020). Enhanced visible light photocatalytic degradation of tetracycline by MoS2/Ag/g-C3N4 Z-scheme composites with peroxymonosulfate. *Applied Surface Science, 514*, 146076.

Jin, C., Wang, M., Li, Z., Kang, J., Zhao, Y., Han, J., & Wu, Z. (2020). Two dimensional Co3O4/g-C3N4 Z-scheme heterojunction: Mechanism insight into enhanced peroxymonosulfate-mediated visible light photocatalytic performance. *Chemical Engineering Journal, 398*, 125569.

Jing, Y., Fan, A., Guo, J., Shen, T., Yuan, S., & Chu, Y. (2022). Synthesis of an ultrathin MnO2 nanosheet-coated Bi2WO6 nanosheet as a heterojunction photocatalyst with enhanced photocatalytic activity. *Chemical Engineering Journal, 429*, 132193.

Johnson, E., & Arshad, S. E. (2014). Hydrothermally synthesized zeolites based on kaolinite: A review. *Applied Clay Science, 97*, 215-221.

Joshi, S., Ippolito, S. J., & Sunkara, M. V. (2016). Convenient architectures of Cu 2 O/SnO 2 type II p–n heterojunctions and their application in visible light catalytic degradation of rhodamine B. *RSC advances, 6*(49), 43672-43684.

Julien, C. M., & Mauger, A. (2017). Nanostructured MnO2 as electrode materials for energy storage. *Nanomaterials, 7*(11), 396.

Karimi-Shamsabadi, M., Behpour, M., Babaheidari, A. K., & Saberi, Z. (2017). Efficiently enhancing photocatalytic activity of NiO-ZnO doped onto nanozeoliteX by synergistic effects of pn heterojunction, supporting and zeolite nanoparticles in photo-degradation of Eriochrome Black T and Methyl Orange. *Journal of photochemistry and Photobiology A: Chemistry, 346*, 133-143.

Ke, G., Shen, H., & Yang, P. (2019). Synthesis of X-Zeolite from waste basalt powder and its influencing factors and synthesis mechanism. *Materials, 12*(23), 3895.

Keerthana, S., Yuvakkumar, R., Ravi, G., Kumar, P., Elshikh, M. S., Alkhamis, H. H., . . . Velauthapillai, D. (2021). A strategy to enhance the photocatalytic efficiency of α-Fe2O3. *Chemosphere, 270*, 129498.

Kemacheevakul, P., & Chuangchote, S. (2020). Photocatalytic Remediation of Organic Pollutants in Water. In *Water Pollution and Remediation: Photocatalysis* (pp. 1-51): Springer.

Khor, C. M., Khan, M. M., Khan, A., Khan, M. Y., & Harunsani, M. H. (2022). Zr-doped silver niobates for photocatalytic degradation of methylene blue and rhodamine B dyes. *Optik, 267*, 169732.

Kim, E.-J., Lee, C.-S., Chang, Y.-Y., & Chang, Y.-S. (2013). Hierarchically structured manganese oxide-coated magnetic nanocomposites for the efficient removal of heavy metal ions from aqueous systems. *ACS Applied Materials & Interfaces, 5*(19), 9628-9634.

Klein, A. (2012). Energy band alignment at interfaces of semiconducting oxides: A review of experimental determination using photoelectron spectroscopy and comparison with theoretical predictions by the electron affinity rule, charge neutrality levels, and the common anion rule. *Thin Solid Films, 520*(10), 3721-3728.

Kumar, R., Rashid, J., & Barakat, M. (2015). Zero valent Ag deposited TiO2 for the efficient photocatalysis of methylene blue under UV-C light irradiation. *Colloids and Interface Science Communications, 5*, 1-4.

Le, H. S., Tran, V. A., Sang-Wha, L., Doan, V.-D., Joo, S.-W., & Vasseghian, Y. (2022). Enhanced photocatalytic degradation of reactive blue 19 using zeolitic imidazolate framework-8 composited with Fe3O4/MnO2 heterojunction. *Journal of industrial and engineering chemistry*.

Lee, S.-Y., & Park, S.-J. (2013). TiO2 photocatalyst for water treatment applications. *Journal of industrial and engineering chemistry, 19*(6), 1761-1769.

Li, B., Nengzi, L.-C., Guo, R., Cui, Y., Zhang, Y., & Cheng, X. (2020). Novel synthesis of Z-scheme α-Bi2O3/g-C3N4 composite photocatalyst and its enhanced visible light photocatalytic performance: Influence of calcination temperature. *Chinese Chemical Letters, 31*(10), 2705-2711.

Li, L., Nan, C., Lu, J., Peng, Q., & Li, Y. (2012). α-MnO 2 nanotubes: high surface area and enhanced lithium battery properties. *Chemical communications, 48*(55), 6945-6947.

Li, Q., Zhao, Y., Qu, D., Wang, H., Chen, J., & Zhou, R. (2018). Preparation of Ag-MnFe2O4-bentonite magnetic composite for Pb (II)/Cd (II) adsorption removal and bacterial inactivation in wastewater. *Chemical Research in Chinese Universities, 34*(5), 808-816.

Li, X., Fang, G., Qian, X., & Tian, Q. (2022). Z-scheme heterojunction of low conduction band potential MnO2 and biochar-based g-C3N4 for efficient formaldehyde degradation. *Chemical Engineering Journal, 428*, 131052.

Li, X., Raza, S., & Liu, C. (2021). Enhanced photo-catalytic efficiency through dual-functional ZIF based materials: Fabrication and application as a degradation of organic dyes. *Journal of the Taiwan Institute of Chemical Engineers, 120*, 368-380.

Li, Y.-F., Zhu, S.-C., & Liu, Z.-P. (2016). Reaction network of layer-to-tunnel transition of MnO2. *Journal of the American Chemical Society, 138*(16), 5371-5379.

Li, Z., Kang, W., Han, Z., Yan, J., Cheng, B., & Liu, Y. (2019). Hierarchical MnOx@ PVDF/MWCNTs tree-like nanofiber membrane with high catalytic oxidation activity. *Journal of alloys and compounds, 780*, 805-815.

Liu, F., Xiao, Y., Liu, Y., Han, P., & Qin, G. (2020). Mesoporous MnO2 based composite electrode for efficient alkali-metal-ion storage. *Chemical Engineering Journal, 380*, 122487.

Liu, H., Wang, C., & Wang, G. (2020). Photocatalytic advanced oxidation processes for water treatment: recent advances and perspective. *Chemistry–An Asian Journal, 15*(20), 3239-3253.

Liu, S., Liu, H., Jin, G., & Yuan, H. (2015). Preparation of a novel flower-like MnO 2/BiOI composite with highly enhanced adsorption and photocatalytic activity. *RSC advances, 5*(57), 45646-45653.

Lou, T., Yan, X., & Wang, X. (2019). Chitosan coated polyacrylonitrile nanofibrous mat for dye adsorption. *International journal of biological macromolecules, 135*, 919-925.

Luévano-Hipólito, E., Torres-Martínez, L. M., & Fernández-Trujillo, A. (2021). Ternary ZnO/CuO/Zeolite composite obtained from volcanic ash for photocatalytic CO2 reduction and H2O decomposition. *Journal of Physics and Chemistry of Solids, 151*, 109917.

Luo, Y., Wei, X., Gao, B., Zou, W., Zheng, Y., Yang, Y., . . . Dong, L. (2019). Synergistic adsorption-photocatalysis processes of graphitic carbon nitrate (g-C3N4) for contaminant removal: Kinetics, models, and mechanisms. *Chemical Engineering Journal, 375*, 122019.

Lyu, Y., Li, C., Du, X., Zhu, Y., Zhang, Y., & Li, S. (2020). Catalytic oxidation of toluene over MnO2 catalysts with different Mn (II) precursors and the study of reaction pathway. *Fuel, 262*, 116610.

Ma, Z., Shao, G., Fan, Y., Wang, G., Song, J., & Shen, D. (2016). Construction of hierarchical α-MnO2 nanowires@ ultrathin δ-MnO2 nanosheets core–shell nanostructure with excellent cycling stability for high-power asymmetric supercapacitor electrodes. *ACS Applied Materials & Interfaces, 8*(14), 9050-9058.

Machineni, L. (2019). Review on biological wastewater treatment and resources recovery: attached and suspended growth systems. *Water Science and Technology, 80*(11), 2013-2026.

Manikandan, S., & Sasikumar, D. (2022). Improving sunlight-photocatalytic activity of undoped and phosphorus doped MnO2 with activated carbon from bio-waste with nanorods morphology. *Inorganic Chemistry Communications, 144*, 109942.

McFarland, E. W., & Metiu, H. (2013). Catalysis by doped oxides. *Chemical reviews, 113*(6), 4391-4427.

Milenković, D. A., Dimić, D. S., Avdović, E. H., Amić, A. D., Marković, J. M. D., & Marković, Z. S. (2020). Advanced oxidation process of coumarins by hydroxyl radical: Towards the new mechanism leading to less toxic products. *Chemical Engineering Journal, 395*, 124971.

Mingshan, D., Xiaoming, T., Guan, W., Huaijie, Y., Zengqiang, L., Junzhang, L., & Gongze, C. (2021). Remediation of high oil content of oil sludge-contaminated soil by hot water washing and biodegradation. *Chinese Journal of Environmental Engineering, 15*(6), 2063-2071.

Mohammadi, T., Moheb, A., Sadrzadeh, M., & Razmi, A. (2005). Modeling of metal ion removal from wastewater by electrodialysis. *Separation and Purification Technology, 41*(1), 73-82.

Motahari, F., Mozdianfard, M. R., Soofivand, F., & Salavati-Niasari, M. (2014). NiO nanostructures: synthesis, characterization and photocatalyst application in dye wastewater treatment. *RSC advances, 4*(53), 27654-27660.

Mouni, L., Belkhiri, L., Bollinger, J.-C., Bouzaza, A., Assadi, A., Tirri, A., . . . Remini, H. (2018). Removal of Methylene Blue from aqueous solutions by adsorption on Kaolin: Kinetic and equilibrium studies. *Applied Clay Science, 153*, 38-45.

Muga, H. E., & Mihelcic, J. R. (2008). Sustainability of wastewater treatment technologies. *Journal of environmental management, 88*(3), 437-447.

Musyoka, N. M. (2012). Zeolite A, X and Cancrinite from South African coal fly ash: mechanism of crystallization, routes to rapid synthesis and new morphology.

Musyoka, N. M., Petrik, L. F., Hums, E., Kuhnt, A., & Schwieger, W. (2015). Thermal stability studies of zeolites A and X synthesized from South African coal fly ash. *Research on Chemical Intermediates, 41*, 575-582.

Najafpour, M. M., & Allakhverdiev, S. I. (2012). Manganese compounds as water oxidizing catalysts for hydrogen production via water splitting: from manganese complexes to nano-sized manganese oxides. *International journal of hydrogen energy, 37*(10), 8753-8764.

Nakabayashi, Y., Nishikawa, M., & Nosaka, Y. (2014). Fabrication of CuBi2O4 photocathode through novel anodic electrodeposition for solar hydrogen production. *Electrochimica Acta, 125*, 191-198.

Nakhaei, M., Barzgari, Z., Mohammadi, S. S., & Ghazizadeh, A. (2019). Preparation of MnO 2/bentonite nanocomposite with enhanced photocatalytic activity under sunlight irradiation. *Research on Chemical Intermediates, 45*, 4995-5005.

Natarajan, S., Bajaj, H. C., & Tayade, R. J. (2018). Recent advances based on the synergetic effect of adsorption for removal of dyes from waste water using photocatalytic process. *Journal of Environmental Sciences, 65*, 201-222.

Nathanson, J. A., & Ambulkar, A. (2018). Wastewater treatment. *Encyclopedia Britannica, available at: www. britannica. com/technology/wastewater-treatment (accessed June 3, 2018)*.

Nevárez-Martínez, M. C., Kobylański, M. P., Mazierski, P., Wółkiewicz, J., Trykowski, G., Malankowska, A., . . . Zaleska-Medynska, A. (2017). Self-organized TiO2–MnO2 nanotube arrays for efficient photocatalytic degradation of toluene. *Molecules, 22*(4), 564.

Nuengmatcha, P., Chanthai, S., Mahachai, R., & Oh, W.-C. (2016). Sonocatalytic performance of ZnO/graphene/TiO2 nanocomposite for degradation of dye pollutants (methylene blue, texbrite BAC-L, texbrite BBU-L and texbrite NFW-L) under ultrasonic irradiation. *Dyes and pigments, 134*, 487-497.

Pang, W., Yu, J., Xu, R., Huo, Q., & Chen, J. (2009). *Chemistry of zeolites and related porous materials: synthesis and structure*: John Wiley & Sons.

Panimalar, S., Uthrakumar, R., Selvi, E. T., Gomathy, P., Inmozhi, C., Kaviyarasu, K., & Kennedy, J. (2020). Studies of MnO2/g-C3N4 hetrostructure efficient of visible light photocatalyst for pollutants degradation by sol-gel technique. *Surfaces and Interfaces, 20*, 100512.

Pargoletti, E., Pifferi, V., Falciola, L., Facchinetti, G., Depaolini, A. R., Davoli, E., . . . Cappelletti, G. (2019). A detailed investigation of MnO2 nanorods to be grown onto

activated carbon. High efficiency towards aqueous methyl orange adsorption/degradation. *Applied Surface Science, 472*, 118-126.

Parsapur, R. K., & Selvam, P. (2018). Rational design, synthesis, characterization and catalytic properties of high-quality low-silica hierarchical FAU-and LTA-type zeolites. *Scientific reports, 8*(1), 16291.

Paul, A. M., Sajeev, A., Nivetha, R., Gothandapani, K., Bhardwaj, P., Govardhan, K., . . . Jeong, S. K. (2020). Cuprous oxide (Cu2O)/graphitic carbon nitride (g-C3N4) nanocomposites for electrocatalytic hydrogen evolution reaction. *Diamond and Related Materials, 107*, 107899.

Pera-Titus, M., García-Molina, V., Baños, M. A., Giménez, J., & Esplugas, S. (2004). Degradation of chlorophenols by means of advanced oxidation processes: a general review. *Applied Catalysis B: Environmental, 47*(4), 219-256.

Plascencia-Hernández, F., Luna, A. L., Colbeau-Justin, C., Santiago, P., Garcia-Rocha, M., Valverde-Aguilar, G., & Valenzuela, M. A. (2019). Cu2O cubic and polyhedral structures versus commercial powder: shape effect on photocatalytic activity under visible light. *Journal of Saudi Chemical Society, 23*(8), 1016-1023.

Pradhan, M. R., Rath, D., Sethi, R., Nanda, B. B., & Nanda, B. (2021). α-MnO2 modified exfoliated porous g-C3N4 nanosheet (2D) for enhanced photocatalytic oxidation efficiency of aromatic alcohols. *Inorganic Chemistry Communications, 130*, 108717.

Prakash, K., Senthil Kumar, P., Pandiaraj, S., Saravanakumar, K., & Karuthapandian, S. (2016). Controllable synthesis of SnO2 photocatalyst with superior photocatalytic activity for the degradation of methylene blue dye solution. *Journal of Experimental Nanoscience, 11*(14), 1138-1155.

Quiton, K. G. N., Lu, M.-C., & Huang, Y.-H. (2021). Synthesis and catalytic utilization of bimetallic systems for wastewater remediation: A review. *Chemosphere, 262*, 128371.

Rahimi, B., Jafari, N., Abdolahnejad, A., Farrokhzadeh, H., & Ebrahimi, A. (2019). Application of efficient photocatalytic process using a novel BiVO/TiO2-NaY zeolite composite for removal of acid orange 10 dye in aqueous solutions: Modeling by response surface methodology (RSM). *Journal of environmental chemical engineering, 7*(4), 103253.

Rajendran, R., Sasireka, A., Priya, P., Vignesh, S., Suganthi, S., Vairamuthu, R., . . . Ramasamy, P. (2021). Investigation on Cu2O Combined g-C3N4/ZnO Heterostructures For High-Performance Photocatalytic Dye Degradation Under Visible-Light Exposure.

Rao, U., Su, Y., Khor, C. M., Jung, B., Ma, S., Cwiertny, D. M., . . . Jassby, D. (2020). Structural dependence of reductive defluorination of linear PFAS compounds in a UV/electrochemical system. *Environmental science & technology, 54*(17), 10668-10677.

Raza, W., Faisal, S. M., Owais, M., Bahnemann, D., & Muneer, M. (2016). Facile fabrication of highly efficient modified ZnO photocatalyst with enhanced photocatalytic, antibacterial and anticancer activity. *RSC advances, 6*(82), 78335-78350.

Rodriguez, J., Puzenat, E., & Thivel, P.-X. (2016). From solar photocatalysis to fuel-cell: A hydrogen supply chain. *Journal of environmental chemical engineering, 4*(3), 3001-3005.

Salari, H. (2019). Kinetics and mechanism of enhanced photocatalytic activity under visible light irradiation using Cr2O3/Fe2O3 nanostructure derived from bimetallic metal organic framework. *Journal of environmental chemical engineering, 7*(3), 103092.

Salari, H. (2020). Efficient photocatalytic degradation of environmental pollutant with enhanced photocarrier separation in novel Z-scheme a-MnO2 nanorod/a-MoO3 nanocomposites. *Journal of photochemistry and Photobiology A: Chemistry, 401*, 112787.

Salari, H., & Hosseini, H. H. (2021). In situ synthesis of visible-light-driven a-MnO2 nanorod/AgBr nanocomposites for increased photoinduced charge separation and enhanced photocatalytic activity. *Materials Research Bulletin, 133*, 111046.

Salari, H., & Yaghmaei, H. (2020). Z-scheme 3D Bi2WO6/MnO2 heterojunction for increased photoinduced charge separation and enhanced photocatalytic activity. *Applied Surface Science, 532*, 147413.

Santhoshkumar, S., & Murugan, E. (2021). Rationally designed SERS AgNPs/GO/g-CN nanohybrids to detect methylene blue and Hg2+ ions in aqueous solution. *Applied Surface Science, 553*, 149544.

Saputra, E., Muhammad, S., Sun, H., Patel, A., Shukla, P., Zhu, Z., & Wang, S. (2012). α-MnO2 activation of peroxymonosulfate for catalytic phenol degradation in aqueous solutions. *Catalysis Communications, 26*, 144-148.

Schneider, J., Matsuoka, M., Takeuchi, M., Zhang, J., Horiuchi, Y., Anpo, M., & Bahnemann, D. W. (2014). Understanding TiO2 photocatalysis: mechanisms and materials. *Chemical reviews, 114*(19), 9919-9986.

Sethia, G., Somani, R. S., & Bajaj, H. C. (2015). Adsorption of carbon monoxide, methane and nitrogen on alkaline earth metal ion exchanged zeolite-X: structure, cation position and adsorption relationship. *RSC advances, 5*(17), 12773-12781.

Shaker-Agjekandy, S., & Habibi-Yangjeh, A. (2016). Ultrasonic-assisted preparation of novel ternary ZnO/AgI/Ag2CrO4 nanocomposites as visible-light-driven photocatalysts with excellent activity. *Materials Science in Semiconductor Processing, 44*, 48-56.

Shim, H. Y., Lee, K. S., Lee, D. S., Jeon, D. S., Park, M. S., Shin, J. S., . . . Chung, D. Y. (2014). Application of electrocoagulation and electrolysis on the precipitation of heavy metals and particulate solids in washwater from the soil washing. *Journal of Agricultural Chemistry and Environment, 3*(04), 130.

Shirzadi, A., & Nezamzadeh-Ejhieh, A. (2016). Enhanced photocatalytic activity of supported CuO–ZnO semiconductors towards the photodegradation of mefenamic acid aqueous solution as a semi real sample. *Journal of Molecular Catalysis A: Chemical, 411*, 222-229.

Siddiqui, S. I., Manzoor, O., Mohsin, M., & Chaudhry, S. A. (2019). Nigella sativa seed based nanocomposite-MnO2/BC: An antibacterial material for photocatalytic degradation, and adsorptive removal of Methylene blue from water. *Environmental research, 171*, 328-340.

Singh, M., Goyal, M., & Devlal, K. (2018). Size and shape effects on the band gap of semiconductor compound nanomaterials. *Journal of Taibah University for Science, 12*(4), 470-475.

Song, H., Zhao, H., Zhang, X., Xu, Y., Cheng, X., Gao, S., & Huo, L. (2019). A hollow urchin-like α-MnO 2 as an electrochemical sensor for hydrogen peroxide and dopamine with high selectivity and sensitivity. *Microchimica Acta, 186*, 1-12.

Sturm, M., Goldstein, M. A., & Parr, C. (2017). Water and life from snow: A trillion dollar science question. *Water Resources Research, 53*(5), 3534-3544.

Su, T., Zhao, B., Fan, B., Li, H., & Zhang, R. (2019). Enhanced microwave absorption properties of novel hierarchical core-shell δ/α MnO2 composites. *Journal of Solid State Chemistry, 273*, 192-198.

Sun, L.-J., & Liu, X.-X. (2008). Electrodepositions and capacitive properties of hybrid films of polyaniline and manganese dioxide with fibrous morphologies. *European Polymer Journal, 44*(1), 219-224.

Tang, Y., Zheng, S., Xu, Y., Xiao, X., Xue, H., & Pang, H. (2018). Advanced batteries based on manganese dioxide and its composites. *Energy Storage Materials, 12*, 284-309.

Tara, N., Siddiqui, S. I., Bach, Q.-V., & Chaudhry, S. A. (2020). Reduce graphene oxide-manganese oxide-black cumin based hybrid composite (rGO-MnO2/BC): a novel material for water remediation. *Materials Today Communications, 25*, 101560.

Tedla, H., Díaz, I., Kebede, T., & Taddesse, A. M. (2015). Synthesis, characterization and photocatalytic activity of zeolite supported ZnO/Fe2O3/MnO2 nanocomposites. *Journal of environmental chemical engineering, 3*(3), 1586-1591.

Thenmozhi, E., Harshavardhan, M., Kamala-Kannan, S., & Janaki, V. (2022). Synthesis and characterization of mesoporous silica-MnO2 nanocomposite–An efficient nanocatalyst for Methylene blue degradation. *Materials Letters, 309*, 131367.

Tian, C., Zhang, Q., Wu, A., Jiang, M., Liang, Z., Jiang, B., & Fu, H. (2012). Cost-effective large-scale synthesis of ZnO photocatalyst with excellent performance for dye photodegradation. *Chemical communications, 48*(23), 2858-2860.

Toupin, M., Brousse, T., & Bélanger, D. (2002). Influence of microstucture on the charge storage properties of chemically synthesized manganese dioxide. *Chemistry of materials, 14*(9), 3946-3952.

Toupin, M., Brousse, T., & Bélanger, D. (2004). Charge storage mechanism of MnO2 electrode used in aqueous electrochemical capacitor. *Chemistry of materials, 16*(16), 3184-3190.

Tsitsishvili, V., Dolaberidze, N., Mirdzveli, N., Nijaradze, M., Amiridze, Z., Gabunia, V., & Tsintskaladze, G. (2019). Hydrothermal transformation of natural analcime and phillipsite. *Bull. Georg. Natl. Acad. Sci, 13*(1).

Tufail, A., Price, W. E., Mohseni, M., Pramanik, B. K., & Hai, F. I. (2021). A critical review of advanced oxidation processes for emerging trace organic contaminant degradation: Mechanisms, factors, degradation products, and effluent toxicity. *Journal of Water Process Engineering, 40*, 101778.

Uddin, M. T., Nicolas, Y., Olivier, C., Jaegermann, W., Rockstroh, N., Junge, H., & Toupance, T. (2017). Band alignment investigations of heterostructure NiO/TiO 2 nanomaterials used as efficient heterojunction earth-abundant metal oxide photocatalysts for hydrogen production. *Physical Chemistry Chemical Physics, 19*(29), 19279-19288.

Upadhyay, R. K., Soin, N., & Roy, S. S. (2014). Role of graphene/metal oxide composites as photocatalysts, adsorbents and disinfectants in water treatment: a review. *RSC advances, 4*(8), 3823-3851.

Vickers, N. J. (2017). Animal communication: when i'm calling you, will you answer too? *Current biology, 27*(14), R713-R715.

Wan, X., Yang, S., Cai, Z., He, Q., Ye, Y., Xia, Y., . . . Liu, J. (2019). Facile synthesis of MnO2 nanoflowers/N-doped reduced graphene oxide composite and its application for simultaneous determination of dopamine and uric acid. *Nanomaterials, 9*(6), 847.

Wang, J., & Wang, S. (2020). Reactive species in advanced oxidation processes: Formation, identification and reaction mechanism. *Chemical Engineering Journal, 401*, 126158.

Wang, Q., & Yang, Z. (2016). Industrial water pollution, water environment treatment, and health risks in China. *Environmental pollution, 218*, 358-365.

Wang, S., Tang, S., Yang, H., Wang, F., Yu, C., Gao, H., . . . Li, D. (2022). A novel heterojunction ZnO/CuO piezoelectric catalysts: fabrication, optical properties and piezoelectric catalytic activity for efficient degradation of methylene blue. *Journal of Materials Science: Materials in Electronics, 33*(9), 7172-7190.

Warang, T., Patel, N., Fernandes, R., Bazzanella, N., & Miotello, A. (2013). Co3O4 nanoparticles assembled coatings synthesized by different techniques for photo-degradation of methylene blue dye. *Applied Catalysis B: Environmental, 132*, 204-211.

Wei, B., Yang, N., Pang, F., & Ge, J. (2018). Cu2O–CuO hollow nanospheres as a heterogeneous catalyst for synergetic oxidation of CO. *The Journal of Physical Chemistry C, 122*(34), 19524-19531.

Worku, A. K., Ayele, D. W., & Habtu, N. G. (2021). Influence of nickel doping on MnO 2 nanoflowers as electrocatalyst for oxygen reduction reaction. *SN Applied Sciences, 3*, 1-16.

Wu, W., Jiang, C., & Roy, V. A. (2015). Recent progress in magnetic iron oxide–semiconductor composite nanomaterials as promising photocatalysts. *Nanoscale, 7*(1), 38-58.

Xia, P., Zhu, B., Cheng, B., Yu, J., & Xu, J. (2018). 2D/2D g-C3N4/MnO2 nanocomposite as a direct Z-scheme photocatalyst for enhanced photocatalytic activity. *ACS Sustainable Chemistry & Engineering, 6*(1), 965-973.

Xiao, L., Sun, W., Zhou, X., Cai, Z., & Hu, F. (2018). Facile synthesis of mesoporous MnO2 nanosheet and microflower with efficient photocatalytic activities for organic dyes. *Vacuum, 156*, 291-297.

Xing, Z., Zhang, J., Cui, J., Yin, J., Zhao, T., Kuang, J., . . . Zhou, W. (2018). Recent advances in floating TiO2-based photocatalysts for environmental application. *Applied Catalysis B: Environmental, 225*, 452-467.

Xu, R., Pang, W., Yu, J., Huo, Q., & Chen, J. (2009). *Chemistry of zeolites and related porous materials: synthesis and structure*: John Wiley & Sons.

Xue, C., Zhang, P., Shao, G., & Yang, G. (2020). Effective promotion of spacial charge separation in direct Z-scheme WO3/CdS/WS2 tandem heterojunction with enhanced visible-light-driven photocatalytic H2 evolution. *Chemical Engineering Journal, 398*, 125602.

Yang, H., Zhang, K., Shi, R., Li, X., Dong, X., & Yu, Y. (2006). Sol–gel synthesis of TiO2 nanoparticles and photocatalytic degradation of methyl orange in aqueous TiO2 suspensions. *Journal of alloys and compounds, 413*(1-2), 302-306.

Yang, N., Lv, X., Zhong, S., Qian, D., Han, S., Li, D., . . . Jiang, W. (2018). Preparation of Z-scheme AgI/Bi 5 O 7 I plate with high visible light photocatalytic performance by phase transition and morphological transformation of BiOI microspheres at room temperature. *Dalton Transactions, 47*(33), 11420-11428.

Yang, R., Fan, Y., Ye, R., Tang, Y., Cao, X., Yin, Z., & Zeng, Z. (2021). MnO2-based materials for environmental applications. *Advanced Materials, 33*(9), 2004862.

Yaseen, D., & Scholz, M. (2019). Textile dye wastewater characteristics and constituents of synthetic effluents: a critical review. *International Journal of Environmental Science and Technology, 16*(2), 1193-1226.

Ye, K.-H., Yu, X., Qiu, Z., Zhu, Y., Lu, X., & Zhang, Y. (2015). Facile synthesis of bismuth oxide/bismuth vanadate heterostructures for efficient photoelectrochemical cells. *RSC advances, 5*(43), 34152-34156.

Yi, X.-H., Ma, S.-Q., Du, X.-D., Zhao, C., Fu, H., Wang, P., & Wang, C.-C. (2019). The facile fabrication of 2D/3D Z-scheme g-C3N4/UiO-66 heterojunction with enhanced photocatalytic Cr (VI) reduction performance under white light. *Chemical Engineering Journal, 375*, 121944.

Yu, C., Yang, K., Shu, Q., Yu, J. C., Cao, F., Li, X., & Zhou, X. (2012). Preparation, characterization and photocatalytic performance of Mo-doped ZnO photocatalysts. *Science china chemistry, 55*, 1802-1810.

Yu, T., Sun, Y., Zhe, C., Wang, W., & Rao, P. (2017). Synthesis of CuO x/MnO 2 Heterostructures with Enhanced Visible Light-Driven Photocatalytic Activity. *Journal of Materials Science and Chemical Engineering, 5*(10), 12.

Yuan, J., Yi, X., Tang, Y., Liu, C., & Luo, S. (2020). Efficient photocatalytic hydrogen evolution and CO2 reduction: enhanced light absorption, charge separation, and hydrophilicity by tailoring terminal and linker units in g-C3N4. *ACS Applied Materials & Interfaces, 12*(17), 19607-19615.

Zambrano, H. L. M., Cobeña, J. A. B., Ponce, J. B. R., Cedeño, U. E. A., & Briones, G. A. B. (2021). Propiedades coagulantes de extractos naturales secos de semillas de M. Oleífera y hojas C. Spinosa en jugo de naranja. *Polo del Conocimiento: Revista científico-profesional, 6*(4), 527-539.

Zhang, G., Sun, Z., Hu, X., Song, A., & Zheng, S. (2017). Synthesis of BiOCl/TiO2–zeolite composite with enhanced visible light photoactivity. *Journal of the Taiwan Institute of Chemical Engineers, 81*, 435-444.

Zhang, M., Arif, M., Hua, Y., Qiu, B., Mao, Y., & Liu, X. (2021). Direct Z-scheme α-MnO 2@ MnIn 2 S 4 hierarchical photocatalysts with atomically defined junctions for improved photocatalytic activities. *Nanoscale Advances, 3*(3), 812-822.

Zhang, Q., Peng, Y., Deng, F., Wang, M., & Chen, D. (2020). Porous Z-scheme MnO2/Mn-modified alkalinized g-C3N4 heterojunction with excellent Fenton-like photocatalytic activity for efficient degradation of pharmaceutical pollutants. *Separation and Purification Technology, 246*, 116890.

Zhang, Y., Deng, B., Zhang, T., Gao, D., & Xu, A.-W. (2010). Shape effects of Cu2O polyhedral microcrystals on photocatalytic activity. *The Journal of Physical Chemistry C, 114*(11), 5073-5079.

Zhao, J., Nan, J., Zhao, Z., Li, N., Liu, J., & Cui, F. (2017). Energy-efficient fabrication of a novel multivalence Mn3O4-MnO2 heterojunction for dye degradation under visible light irradiation. *Applied Catalysis B: Environmental, 202*, 509-517.

Zhao, L., Yu, T., Yang, B., Guo, H., Liu, L., Zhang, J., . . . Zhang, Y. (2022). Wastewater Purification and All-Solid Z-Scheme Heterojunction ZnO-C/MnO2 Preparation: Properties and Mechanism. *Catalysts, 12*(10), 1250.

Zhao, Z., Liu, J., Cui, F., Feng, H., & Zhang, L. (2012). One pot synthesis of tunable Fe 3 O 4–MnO 2 core–shell nanoplates and their applications for water purification. *Journal of Materials Chemistry, 22*(18), 9052-9057.

Zheng, X., Han, Z., Yang, W., Qu, F., Liu, B., & Wu, X. (2016). 3D Co3O4@ MnO2 heterostructures grown on a flexible substrate and their applications in supercapacitor electrodes and photocatalysts. *Dalton Transactions, 45*(42), 16850-16858.

Zhou, P., Yu, J., & Jaroniec, M. (2014). All-solid-state Z-scheme photocatalytic systems. *Advanced Materials, 26*(29), 4920-4935.